SOLUTION-PROCESSED NANOSTRUCTURES AND DEVICES FOR HIGHLY POLARIZED LIGHT GENERATION, SCATTERING AND SENSING

A DISSERTATION SUBMITTED TO

THE GRADUATE SCHOOL OF ENGINEERING AND SCIENCE

OF BILKENT UNIVERSITY

IN PARTIAL FULFILLMENT OF THE REQUIREMENTS FOR

THE DEGREE OF

DOCTOR OF PHILOSOPHY

IN

ELECTRICAL AND ELECTRONICS ENGINEERING

By

Can Uran

December, 2014

SOLUTION-PROCESSED NANOSTRUCTURES AND DEVICES FOR HIGHLY POLARIZED LIGHT GENERATION, SCATTERING AND SENSING

By Can Uran

December, 2014

We certify that we have read this thesis and that in our opinion it is fully adequate, in scope and in quality, as a dissertation for the degree of Doctor of Philosophy.

Assoc. Prof. Dr. Hilmi Volkan Demir (Advisor)

Prof. Dr. Ayhan Altıntaş

Assist. Prof. Dr. Ali Kemal Okyay

Assoc. Prof. Dr. Dönüş Tuncel

Assist. Prof. Dr. Evren Mutlugün

Approved for the Graduate School of Engineering and Science:

Prof. Dr. Levent Onural
Director of the Graduate School

ABSTRACT

SOLUTION-PROCESSED NANOSTRUCTURES AND DEVICES FOR HIGHLY POLARIZED LIGHT GENERATION, SCATTERING AND SENSING

Can Uran
Ph.D. in Electrical and Electronics Engineering
Advisor: Assoc. Prof. Dr. Hilmi Volkan Demir
December, 2014

Recent advancements in photonics have facilitated robust and reliable light sources, displays and photosensors with relatively long lifetimes and high energy efficiency in their classes. However, developing intrinsically polarization selective photonic devices still remains a challenge, although polarization sensitivity is essential to various advanced functions and/or improved performance. One of the main difficulties in making such devices emerges from the compromise on the efficiency while striving to reach high polarization contrast levels. For instance, commercially available birefringent structures including those integrating liquid crystals suffer from major transmission losses. On the other hand, solution-processed, high aspect-ratio nanostructures may offer power efficient platforms with high polarization contrasts via selection of the polarization in a preferred direction during emission, absorption and/or scattering process(es) while suppressing efficiency of the relevant ones in the other polarization. In this thesis, we present solution-processed metal and semiconductor nanostructures and optoelectronic devices made from them for highly polarized light generation and enhanced photosensing. Here we developed and demonstrated in-template fabricated suspended arrays of plasmonic thin nanodiscs with tunable disc-heights and gap-widths tailoring absorption and scattering properties for applications ranging from polarized light scattering to photodetection. Also, we proposed and showed highly polarized light emission in coupled thin films of magnetically aligned multi-segmented nanowires and colloidal nanocrystals for polarized color enrichment in displays. Here well-controlled in-template synthesis of these nanowires together with their alignment under magnetic field allows for highly parallel orientation of the nanowires in massive numbers over large-area thin films. Integrating with color-enriching nanocrystals, this enabled a record high polarization contrast over 15:1 for the isotropic nanocrystals in the visible range. We believe that such

hybrid assemblies of solution-processed nanostructures integrated into optoelectronic devices hold great promise for advanced functions in photonics.

Keywords: Nanowires, nanodiscs, nanocrystals, quantum dots, plasmonic nanostructures, polarization contrast, light generation, scattering, photosensing.

ÖZET

YÜKSEK POLARİZE IŞIMA, SAÇILMA VE ALGILAMA İÇİN SOLÜSYON BAZLI İŞLENMİŞ NANOYAPILAR VE AYGITLAR

Can Uran
Elektrik ve Elektronik Mühendisliği, Doktora
Tez Danışmanı: Assoc. Prof. Dr. Hilmi Volkan Demir
Aralık, 2014

Fotonikteki son gelişmeler, kendi sınıflarında daha uzun ömürlü, yüksek enerji verimli ve güvenilir ışık kaynaklarına, ekranlara ve fotosensörlere imkan sağlamıştır. Ancak, polarizasyon duyarlılığı birçok gelişmiş fonksiyon ve/veya performans için gerekli olmasına rağmen, polarizasyon seçici fotonik aygıtlar geliştirmek hala bir sorun olmaya devam etmektedir. Bu tür cihazların yapımındaki ana zorluklardan biri yüksek polarizasyon kontrast seviyelerine ulaşmaya çalışırken enerji verimliliğindeki verilen ödünden kaynaklanır. Örneğin, mevcut sıvı kristaller ile entegre çift kırılımlı yapılar, ışık iletiminde büyük kayıplar gösterirler. Öte yandan, solüsyon bazlı işlenmiş ve yüksek en boy oranına sahip nanoyapılar, ışıma, soğurma ve saçılım sırasında tercih edilen bir yönde yapılan polarizasyon seçimi ile yüksek polarizasyon oranlı ve aynı zamanda enerji verimli platformlar sunabilir. Bu yapılar, sözü edilen mekanizmalarla bir yöndeki polarizasyonu seçici olarak geçirirken diğer yöndeki polarizasyonu da bastırmaktadır. Bu tezde solüsyon tabanlı işlenmiş metal ve yarı iletken nanoyapıları ve bunlarla yapılan yüksek derece polarize ışık üreten ve artırılımış fotoalgılama yapan optoelektronik aygıtlar sunuyoruz. Burada, şablonda sentezlenen, disk yükseklikleri ve aralık genişlikleri ile soğurma ve saçılım özellikleri ayarlanabilen, havada asılı plazmonik ince nanodisk dizileri üretip gösterdik. Ayrıca, manyetik olarak hizalanmış çok kısımlı nanotellerin kolloidal nanokristaller ile birleştirildiği ince filmler kullanarak polarize renk zenginleştirme uygulamalarında son derece yüksek polarize ışıma önerdik ve gösterdik. Burda şablon içinde yüksek kontrollü sentezlenen nanotellerin manyetik alan altında dizilimi, ince filmli geniş yüzeylerde oldukça paralel ve etkili bir yönlerdirmeyi mümkün kılıyor. Dizilmiş nanotellerin renk zenginleştirici nanokristallerle entegre edilmeleri 15:1in üzerinde, izotropik nanokristaller ile elde edilmiş rekor bir görünür spektrum polarizasyon kontrastı

sağladı. Bu şekilde solüsyon bazlı işlenmiş nanoyapıların optoelektronik cihazlara entegresi ile elde edilen melez oluşumlar fotonikte ileri düzeyde işlevlerin gerçekleştirilmesi için büyük öneme sahiptir.

Anahtar sözcükler: Nanoteller, nanodiskler, nanokristaller, kuvantum noktacıkları, plasmonik nanoyapılar, polarizasyon kontrastı, ışık üretimi, saçılma, fotoalgılama.

Acknowledgement

First of all, I would like to thank my supervisor Prof. Hilmi Volkan Demir, who has provided me with the understanding and motivation in both scientific and daily life. His kind, friendly and motivating personality guided me during my study of research and I am honored with his supervision. I thank him again for his endless effort and support. I would like to thank Prof. Ali Kemal Okyay and Prof. Dönüş Tuncel for serving on my PhD thesis progress committee. They have carefully followed my studies and contributed with their valuable ideas and comments for my thesis progress. I would also like to thank Prof. Ayhan Altıntaş and Prof. Evren Mutlugün for kindly taking part in my PhD thesis defense jury. I would like to thank all of my friends in our Sensors and Devices Research Group for their great support and unforgettable times together: Shahab Akhavan, Akbar Alipour, Talha Erdem, Zeliha Erdem, Burak Güzeltürk, Yusuf Keleştemur, Kıvanç Güngör, Berkay Bozok, Aydan Yeltik, Neslihan Çiçek, Tuncay Özel, İlkem Özge Özel, Zafer Akgül, Onur Erdem, Mustafa Akın Sefünç, Onur Akın, Özgün Akyüz, Emre Ünal, Dr. Emre Sarı, Dr. Murat Soğancı, Prof. Sedat Nizamoğlu, Prof. Nihan Kosku Perkgöz, Prof. Rohat Melik and Prof. Urartu Şeker. I would like to thank all UNAM and ARL researchers and staff for their support and help on my experimental studies and for providing me with a well equipped research environment. I would like to thank all EE faculty, technical and administrative staff, researchers, and to my close friends, Emre Kopanoğlu, Aslı Ünlügedik, Sıtar Kortik, Duygu Şatır, Gülis Zengin, Refik Sina Toru, Elif Aydoğdu, Niyazi Şenlik, Behnam Ghassemiparvin, Volkan Açıkel and Mehmet Can Kerse. I have been really happy to study at my department where I have had very good relations and friendships and at the same time acquire high level of engineering education.

Lastly, I would like to thank a lot my parents, my brother and all my family for their support and love.

Contents

List of Figures

Chapter 1

Introduction

Solution-processed metal and semiconductor nanostructures including nanowires, nanodiscs and nanoparticles are interesting building blocks for nanoscale optoelectronics and electronics, imaging, biosensing and other sensing applications. In-template synthesis of multi-segmented metal nanostructures offers easy and low cost manufacturing capability without time consuming, unlike low throughput nanolithography techniques such as electron beam lithography, focused ion beam and nanoimprint lithography. Moreover, in-solution synthesized colloidal semiconductor nanocrystals are great candidates for light generating and photosensing due to their easy emission tuning and strong absorption properties.

Plasmonic structures enable enhanced light utilization for optoelectronic devices owing to their unique, strong and tunable electric field localization leading to increased scattering and absorption properties [1, 2, 3]. Such nanopatterned plasmonic structures that have been proposed in literature usually use the conventional fabrication techniques of electron beam lithography (EBL) and nanoimprint lithography [4, 5]. Although these methods exhibit high resolution and enable more deterministic structure layouts for plasmonic devices, these technologies are quite costly and limited in throughput. Alternatively, solution-processed nanostructures have been inroduced. For example, metallic nanodiscs can be synthesized using in-template electrodeposition, followed by simple selective etching

of sacrificial metal layers. Previously, a high-throughput procedure for lithographically processing one-dimensional nanowires known as on-wire lithography has been reported [6]. This method uniquely combines in-template electrodepostion of different compositions of nanowires and their selective wet-chemical etching to form disk arrays and gap structures in the range of few nanometers to several hundred nanometers. The fabrication relies on the segmented nanowires consisting of two types of materials, one of which is susceptible and the other of which is resistant to etching after these segments are blanketed by a bridging material. Electrodeposition filling in the porous template is used to prepare segmented nanowires with tailorable dimensions and compositions. In-template electrodeposition of various metals [7], followed by selective etching of sacrificial metal layers, allows for tailoring the light spectrum scattered from these nanodisc structures [8]. The local field enhancement in the close proximity of the plasmonic nanoparticles, which is determined by absorption and scattering mechanisms, is important in sensing [9], surface enhanced Raman spectroscopy (SERS) [10] and fluorescence [11]. The nanodiscs are promising for nanoplasmonics because their optical properties may be fine-tuned either via the disc-gap and/or the disc-width [12]. The spectral line shape of the localized surface plasmon (LSP) resonance of a metallic nanoparticle, as obtained by measuring absorption or scattering cross-section as a function of the photon energy, depends on the material and particle size [13]. These structures enable enhanced light utilization for optoelectronic devices owing to their unique, strong and tunable electric field localization leading to increased scattering and absorption properties.

Sub-wavelength metallic features with promising electrical and optical properties can also be fabricated by using in-template electrodeposition methods for applications from imaging [14] to liquid crystal displays (LCDs) [15]. In literature, ranges of polarizing optical media were integrated with light-emitting materials to achieve polarized light sources. These sources selectively transmit the light with electric field parallel to the transmission axis and block the transmission of the electromagnetic field in the orthogonal polarization. Wire-grid based polarizers [16], plasmonic nanocavities [17], birefringent crystals [18], and liquid crystal integrated fluorescent materials [19] can be utilized to achieve polarized

light emission. Wire-grid polarizers with sub-wavelength structures exhibit very good performance in terms of reshaping the emission polarization. For instance, Zhang et al. reached a vertical (s) to parallel (p) polarization contrast of 7:1 using metallic nanogratings fabricated by electron beam lithography on top of a conventional InGaN/GaN LED [20]. Ma et al. obtained an s/p polarization contrast as high as 50:1, corresponding to a polarization degree of about 0.96 in another recent study [21]. However, such approaches require expensive and time consuming techniques with low throughputs in order to achieve polarized light in the visible spectrum such as focused ion beam lithography, electron beam lithography, and nanoimprint lithography.

Solution-processed colloidal semiconductor nanocrystals (NCs) are crucially important thanks to their color tuning properties, large-area surface coverage abilities and their cost-effective mass fabrication in optoelectronics [22]. These properties allow them to be used as the photoactive absorbing layer in photosensors [23]. The photosensitivity of solution-cast NC photodetectors, either photoconductor [23] or photodiode type [24], is quite impressive with high photoconductive gain and low noise. Conventional NC-based photosensors, with ultrasensitive and fast detection, are reported in literature [25]. In these sensors, external bias must be applied to collect the photogenerated charges. Photodetectors including a Shockley-Schottky barrier can be principally operated without an applied bias in lower sensitivity operation levels. However, they are usually operated under negative bias and show high dark current, which results in high noise levels and limit the detection sensitivity of the device.

In this thesis, we present in-template and in-solution synthesized nanostructures and optoelectronic devices for highly polarized light generation and enhanced photosensing to bring solutions to the aforementioned problems above. We provide straightforwardly fabricated devices with suspended structures or flexible substrates allowing for tailorable absorption, emission and scattering properties for various applications ranging from polarized and/or unpolarized light generation, to imaging and detection.

In Chapter 1, we provide brief information about the importance of solution

processed nanoparticles and nanostructures, which are easily fabricated alternatives to the ones manufactured by conventional methods. Here, we discuss our approaches to address various optical problems and issues in light-emitting devices and light sensors.

In Chapter 2, we provide background information on plasmons and nanocrystal quantum dots. We introduce their optical properties and the underlying physics. We also discuss the role of size, shape and composition of these nanoparticles.

In Chapter 3, we present our in-template electrodeposition methods to fabricate various shaped structures including segmented nanowires with different compositions and suspended nanodisc arrays with tuned disc-/gap- widths, which can be dispersed in solution while discs are securely kept inside insulating wrap.

In Chapter 4, we demonstrate highly polarized light emission in coupled thin films of colloidal nanocrystals and magnetically aligned multi-segmented nanowires. These nanowires consist of ferromagnetic parts, which enable alignment under externally applied magnetic field. In-template synthesis of these nanowires together with their alignment allow for the fabrication of a massive number of highly parallel nanowires incorporated with nanocrystals over large-area thin films with the purpose to generate polarized light with a contrast of polarizations perpendicular to parallel larger than 15:1 in the visible range.

In Chapter 5, we present our results on the light interaction of our fabricated nanodisc arrays. We discuss their disc-/gap-width size dependendent polarization selective light scattering properties and localized electric field enhancements in the medium by performing finite difference time domain (FDTD) simulations, and enhanced voltage buildup measurements in light-sensitive nanocrystal devices, which are remarkable and highly sensitive photosensors with unconventional operation relying on voltage buildup in the absence of an external bias.

In Chapter 6, we show our flexible and fragmantable tandem photosensitive nanocrystal platform, which offers promising advantages in sensors, smart facades and displays. Owing to the monolayer of NCs in the active area of the

device, the noise is remarkably reduced, resulting in high sensitivity levels. The presented tandem photosensitive device is fabricated over large areas on flexible plastics and can be used to build photosensitive multi-junction devices. Such devices offer important enhancements in the sensitivity levels and extensions in the operational wavelength range thanks to different material selections in the subsequent junctions.

In Chapter 7, we conclude with our results on solution-processed and in-template synthesized metal/semiconductor nanostructures, which have advantageous electrical and optical properties to be beneficially used in fabrication of optoelectronic devices for highly polarized light generation and enhanced photosensing for flexible electronics.

Chapter 2

Background

2.1 Semiconductor nanocrystals

Colloidal semiconductor nanocrystals also known as colloidal quantum dots, are nanomaterials composed of II-VI, III-V, and IV-VI elements. They include a few hundred to a thousand atoms. Their small size of a few nanometers, which is less than the Bohr radius, leads to strong quantum confinement effect [26]. This confinement increases the band gap in the discrete and quantized energy levels, meaning that the optical properties of the nanocrystals strongly depend on their sizes. For example, larger nanocrystals emit at longer wavelengths with respect to the smaller ones. In addition to the size dependency, the emission wavelength of the nanocrystals also depends on their composition. Nanocrystals are strong candidates in photonic applications due to their fine bandgap tunability and easy integrability on different substrates (Figure 2.1). CdSe nanocrystals can span an emission range from around 490 nm to 620 nm [27] while PbS and PbSe nanocrystals cover from 850 nm to 2100 nm [28]. Bulk forms of these semiconductor materials exhibit approximately continuous energy bands. Nanocrystals are different from their bulk forms as they exhibit more discrete energy levels due to quantum confinement effects. II-VI group core nanocrystals have been synthesized so far including CdS, CdSe, ZnS, CdTe, PbS, and PbSe. Among them,

Figure 2.1: Semiconductor quantum dots syntesized in our setup.

CdTe nanocrystals are aqueous when they are functiolized via TGA (thioglycolic acid) ligands on their surfaces [29].

2.2 An example of semiconductor nanocrystal synthesis

This part is partially taken from our paper in submission [30]. We synthesize water-soluble thioglycolic acid (TGA)-capped CdTe NCs and 3-mercaptopropionic acid (MPA)-capped CdHgTe NCs [31, 32, 33]. Al_2Te_3 (Cerac Inc) is employed for the generation of H_2Te. During the synthesis, 4.59 g of $Cd(ClO_4)_26H_2O$ and 1.33 g of TGA is dissolved inside 500 mL of deoinized water. The pH of the resulting solution is adjusted to 12 by addition of 1 M NaOH

solution and the solution is blown with argon for 0.5 h. Afterwards, under vigorous stirring, H_2Te gas, generated by the reaction of 0.8 g of Al_2Te_3 with an excess of 0.5 M H_2SO_4 solution, is injected into the deaerated reaction mixture with a slow argon flow. Nucleation and growth of the NCs proceeds upon reflux of the reaction mixture under open-air conditions for 6 h. $Cd_xHg_{1-x}Te$ NCs are synthesized employing a similar procedure [31] according to a previously reported method [33]. Briefly, 0.545 g of $Cd(ClO_4)_26H_2O$, 0.0135 g of $Hg(ClO_4)_26H_2O$ and 0.183 g of MPA are dissolved in 60 mL of water, followed by addition of 1M NaOH solution up to pH = 12. 0.15 g of Al_2Te_3 is used to generate H_2Te gas. Therefore, the molar ratio of $Cd^{2+}/Hg^{2+}/Te^{2-}$/MPA is 0.98/0.02/0.75/1.3. After injection of H_2Te, the color of the solution changes into brown. As in the case of CdTe NCs, nucleation and growth of $Cd_xHg_{1-x}Te$ NCs proceeds upon reflux of the reaction mixture under open-air conditions for 40 min. After cooling the NC solutions to room temperature, they are concentrated on a rotor evaporator by vaporization of 90 % of water. Afterwards, the NCs are precipitated by addition of 2-3 mL of isopropanol to concentrated CdTe and $Cd_xHg_{1-x}Te$ NC colloids, with subsequent centrifugation, and are then redissolved in 5-10 mL of dionized water.

2.3 Layer-by-layer assembly of semiconductor nanocrystals

In order to provide a sufficiently uniform film with high surface coverage for depositing the NC monolayer, we use four bilayers of PDDA-PSS. The concentration of PDDA and PSS is 2 mg/mL in 0.1 M NaCl. We remove the ligands partially by adding isopropanol to the NCs solutions and centrifuging the mixtures for three times. A fully automated dip-coater system is employed for layer-by-layer self-assembly. The PDDA-PSS film is deposited by sequentially dipping the substrate into the prepared solution for 5 min and rinsed with dionized water for 1 min. The thickness of PDDA-PSS bilayer is approximately 1.4 nm as verified by the optical ellipsometry measurement. After coating one extra layer of positively charged PDDA on top of subsequent bilayers, negatively charged water soluble

NCs are coated by immersing the substrate for 20 min in the 4 μM NCs dispersion, with subsequent washing with dionized water for 1 min to remove excess amount of NCs [30].

2.4 Metal nanoparticles

Free electrons confined inside metal nanoparticles can be excited under electromagnetic radiation to have collective oscillations. These collective charge oscillations excited by light are called plasmons [34]. Plasmonics is the study of the interaction of these free electrons with the electromagnetic fields. Surface plasmons are electromagnetic waves at the interface between a dielectric and a conductor. These plasmons can appear as propagating surface waves or localized electron oscillations confined inside metal nanoparticles. The radiation can penetrate into these nanoparticles, which are smaller than the penetration depth into the metal and the conduction electrons are moved away from the nucleus by the field. Due to the Coulomb attraction between the fixed nucleus and these conduction electrons, a restoring force results as the electrons move back and forth. This oscillation frequency is called surface plasmon resonance frequency [35]. This field is highly localized around the close vicinity of the nanoparticle and it decays rapidly away from the nanoparticle into the medium. Moreover, far field scattering from the particle is also enhanced by the plasmon resonance (Figure 2.2).

Drude model is a strong prediction of the plasmon resonance frequency depending on the electron density, the dielectric medium properties and the effective electron mass. This model explains the blue shift in resonance in high electron dense materials compared to the materials with low electron density [36]. Gold (Au) and silver (Ag) nanoparticles have their surface plasmon resonance in frequency ranges corresponding to the visible regions. For Au nanoparticles with the size ranging from 5 to 50 nm, the resonance frequency spans the band from 500 to 600 nm. For Ag particles with the same size range, the resonance covers the spectrum from 380 to 430 nm. On the other hand, aluminum (Al) and mercury (Hg) metals have the plasmon resonance in ultraviolet.

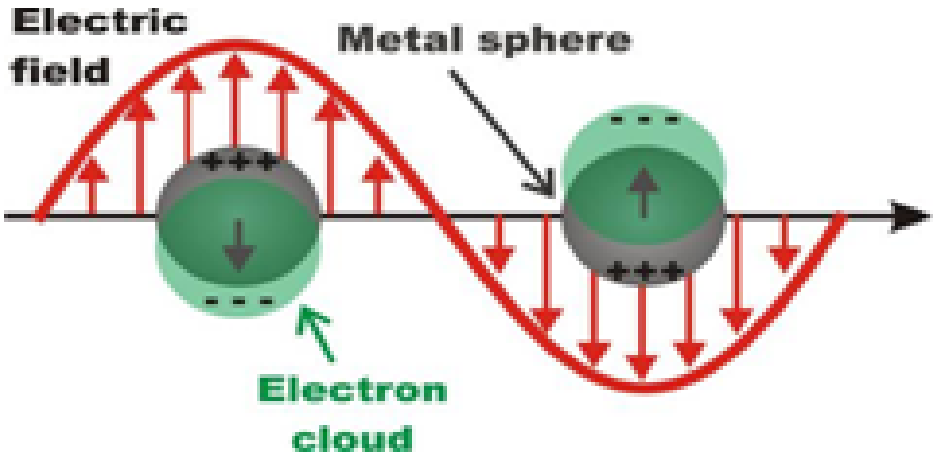

Figure 2.2: Plasmons inside metal nanoparticles.

For rod-shaped nanoparticles, two different resonances appear depending on their orientation with respect to the direction of the electric field of the incident radiation. Different oscillations take place either along the rod, which is the longitudinal axis, or across the rod, which is the transversal axis. For instance, nanowires exhibit a much more directional scattering pattern compared to spherical particles. Due to the particle shape, nanowires are able to focus the scattering into a narrower angular range compared to spherical nanoparticles. Tuning the direction of the scattering from these plasmonic nanoparticles is possible by controlling the aspect ratio of the nanowires [37].

2.5 An example of metal nanoparticle synthesis

This decription is partially taken from our previous work [38]. For gold nanoparticle synthesis, 1 mM hydrogentetrachloroaurate (III) trihydrate ($HAuCl_4.3H_2O$) aqueous solution is prepared (0.08 g $HAuCl_4$ in 200 mL DI water). This solution is heated to 300 °C. 44 mM sodium citrate dehydrate solution (0.26 g in 20 mL DI water) is dropped into $HAuCl_4.3H_2O$ solution while boiling. After becoming dark, the color of the solution starts to turn into red, showing that gold nanoparticles are synthesized after the reaction (Figure 2.3). Absorbance spectrum of

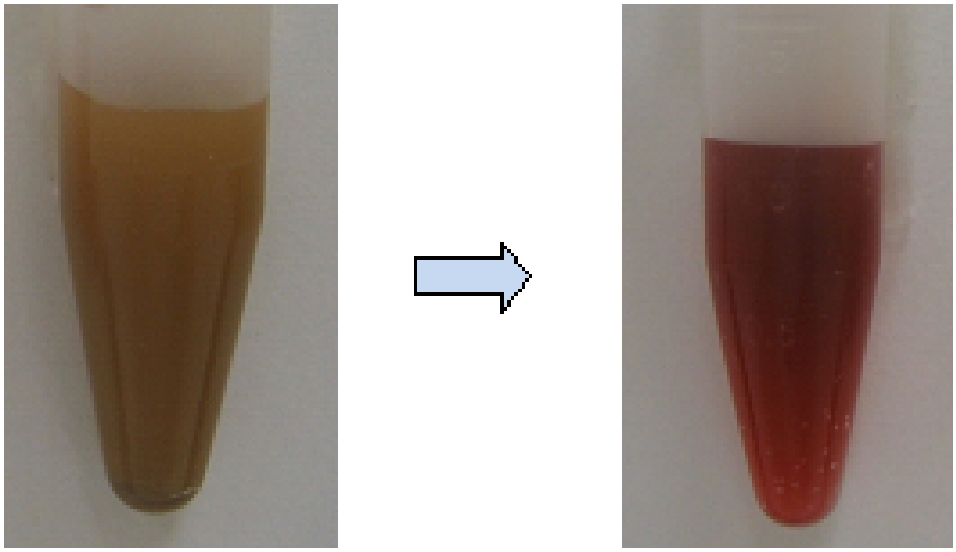

Figure 2.3: Our gold nanowires (on the left) and nanoparticles in water (on the right). As the particle size shrinks smaller than the 50 nm, the color turns reddish due to plasmonic effect.

gold nanoparticles is shown in Figure 2.4.

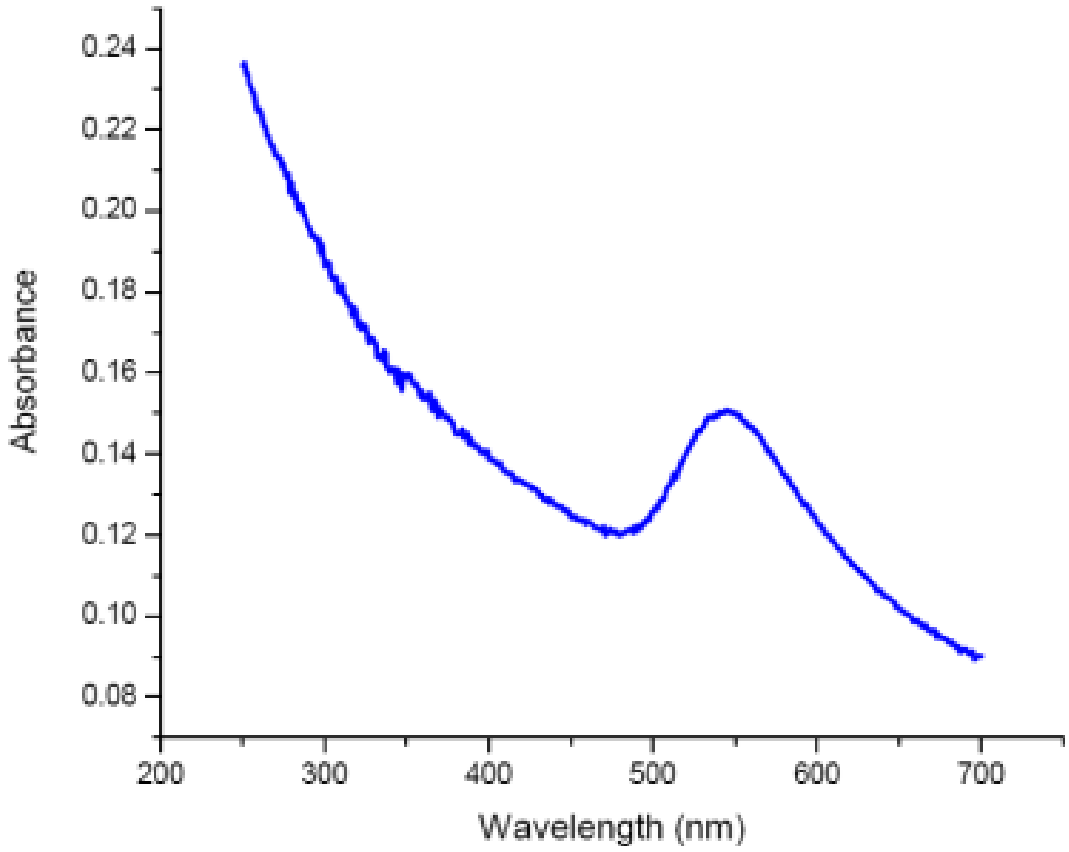

Figure 2.4: Absorbance spectrum of our gold nanoparticles in film.

Chapter 3

In-template electrodeposited nanostructures

3.1 Nanowire synthesis

By subsequent electrodepositions within a porous template, we prepare segmented nanowires with tailorable dimensions and compositions along the length of the wire enabling electrical and optical functionalities [39, 40]. Well-known methods to fabricate such structures with different materials include vapor solid liquid (VLS) growth, which can be used to deposit semiconductor superlattices [41] and templated electrodeposition, which allows for metal deposition by ion reduction inside the pores of a membrane [42, 43]. Keating and Natan groups, again cooperatively synthesized multi-segmented nanowires intrinsically encoded with submicrometer segments to observe different reflectivity patterns from subsequent segments. The optical contrast among reflected lights from different metal segments was the basic principle of this barcoding mechanism. They studied the variety of different metal depositions such as gold (Au), silver (Ag), platinum (Pt), palladium (Pd), nickel (Ni) and cobalt (Co)) in segments from 10 nm to several micrometers, in membranes of different sizes down to 15 nm [44, 45].

Using electrodeposition, we synthesize Au/Ag/Au segmented NWs [46] in porous circular membranes made of aluminum oxide (Whatman Anodisc) employed as the hard template. These membranes are 21 mm in diameter and 60 μm thick with a pore size of 300 nm and a pore density of 10^9 cm^{-2}. The back side of this aluminum oxide (Al_2O_3) membrane coated with 300 nm thick silver by evaporation to be used as the cathode before electrodeposition. A platinum mesh with an area as large as the area of the porous membrane is used as the anode. The silver coated side of the aluminum oxide membrane is placed on the silver plate, which is to be cleaned and rinsed each time before the experiment to make sure the conduction is good during the electrodeposition, just in case it is oxidized.

We prepare our electrodeposition setup for deposition baths by using o-ring and o-ring glass on the top of the disc in order to prevent the leakage of the gold or silver bath (Figure 3.1). The working electrode connects to the silver plate at which the desired deposition occurs by reduction of metal ions. On the other hand, the counter electrode is connected to the platinum mesh. This electrode controls the power output of the potentiostat (Versastat3) electrode (Figure 3.2). By means of sense and reference electrodes, potential difference between the counter and working electrodes is measured to keep control of the deposition rate (Figure 3.3).

We use the method of chronopotentiometry for electrodeposition, where a constant current pulse is driven from the counter electrode to working electrode, while the potential difference between them, is measured against as a function of time. First, we deposit silver with a current level of 1.6 mA for 1200 s from the silver bath containing 42 g/L of silver cyanide and 85 g/L of potassium cyanide (TechniSilver, Italgalvano to make sure that the branching portion of the membrane is totally clogged. The reduction of silver ions occurs for a potential range of 1.40 V and 1.70 V for 1.6 mA of current (Figure 3.4 and Figure 3.5). Second, we start the deposition of the first gold segment using a current level of 1.6 mA for 3600 s in the gold bath (Orotemp 24, Italgalvano). Our rate of gold deposition is 1 nm/s. The reduction of gold ions occurs for a potential range of 1.70 V and 2.65 V for 1.6 mA of current (Figure 3.6). For following Ag segment that

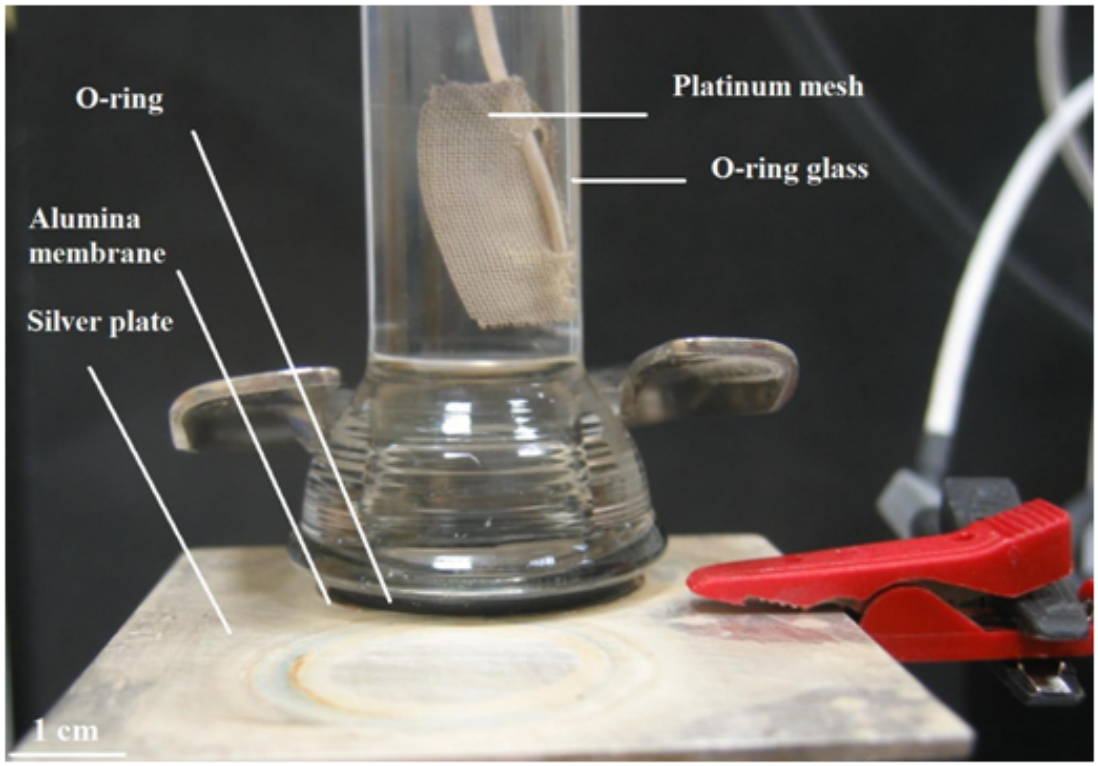

Figure 3.1: Our experimental setup for electrodeposition that includes template membrane disc, o-ring, and plates.

Figure 3.2: Versastat3 potentiostat/galvanostat.

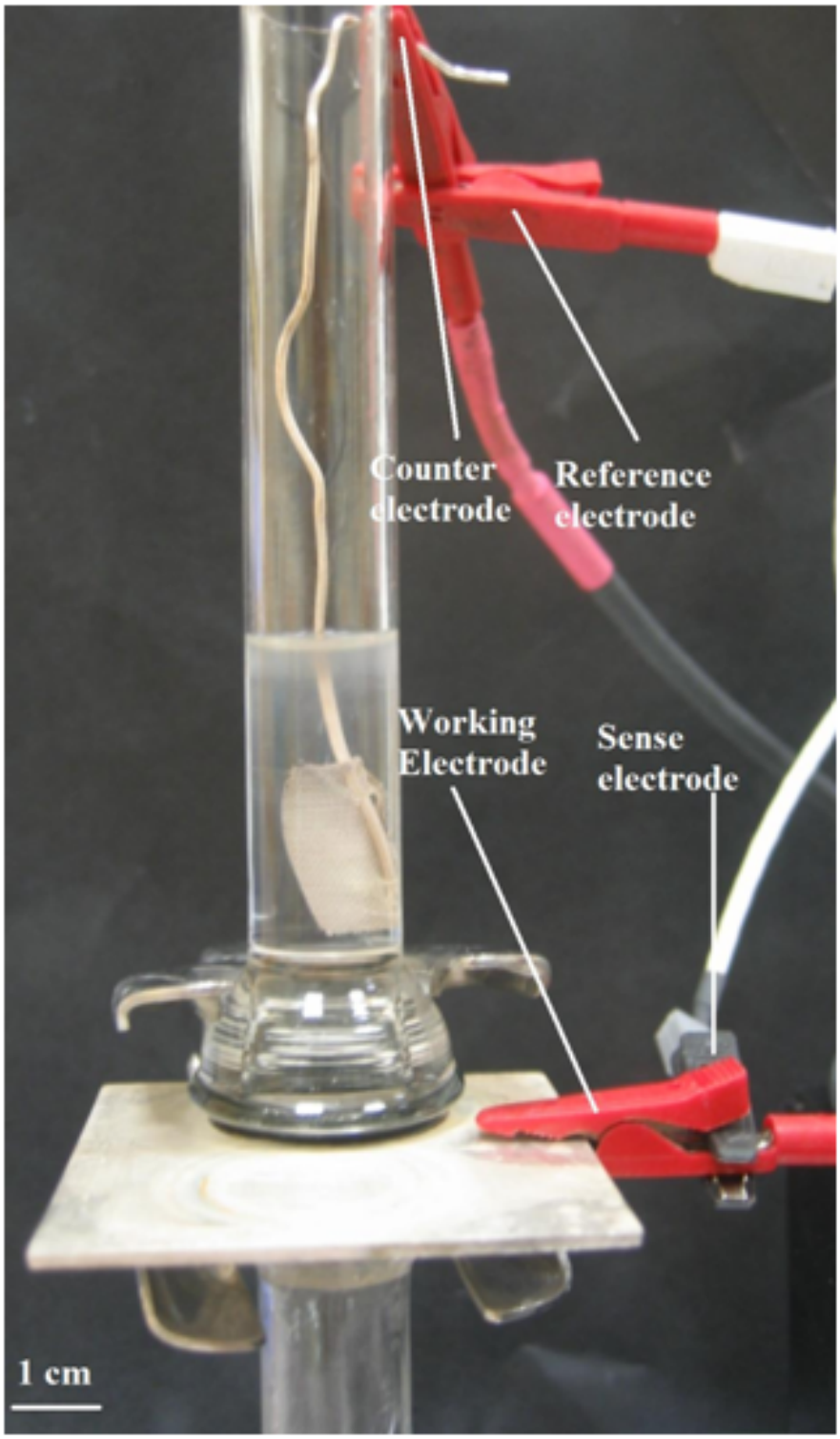

Figure 3.3: Our experimental setup for electrodes.

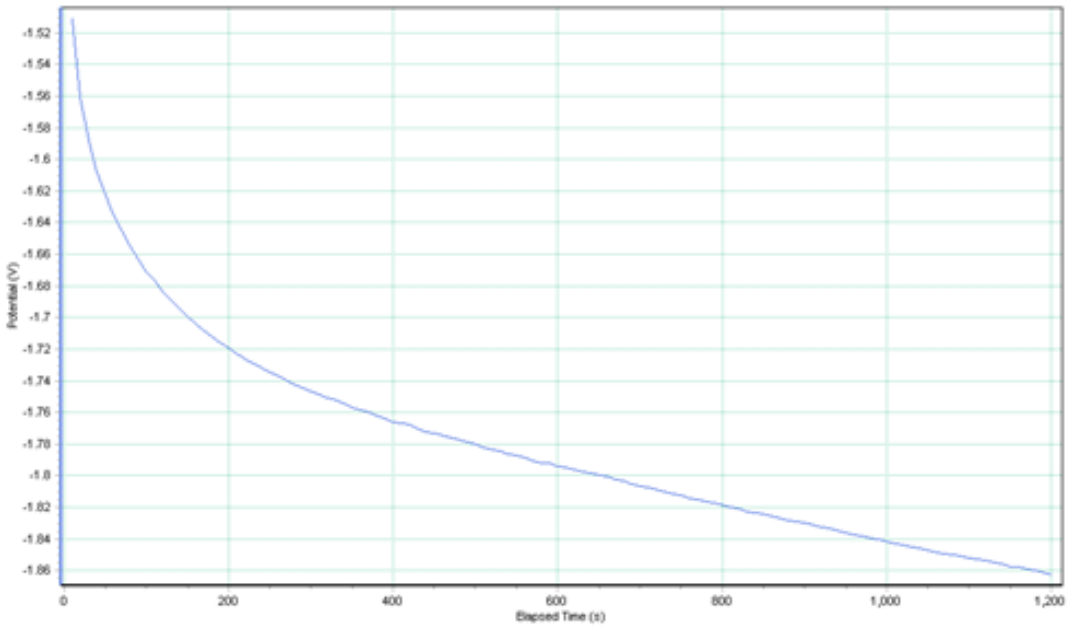

Figure 3.4: Potential trace during silver deposition into the branched part of the alumina disc.

determines the size of our gap, we employ a current level of 1.6 mA while varying deposition times to make Ag segments of varying lengths tuned from 300 nm down to 20 nm. Our rate of silver deposition is 1.5 nm/s. We produced NWs with size controllable nanogaps, depending on the deposition time. Finally, we deposit Au again applying the same current and deposition time with the first Au segment (Figure 3.7). The total lengths of the Au/Ag/Au NWs can be made to extend over 20 μm (e.g., 7.78 μm and 6.65 μm as in our cases in Figure 3.8 and Figure 3.9, respectively) [46].

After finishing the electrodeposition, the backside silver layer is etched with nitric acid solution (HNO_3 of 30 in concentration) and alumina disc is dissolved in sodium hydroxide solution (NaOH of 3 M). The NWs remain in this base solution during dissolution. Subsequently, the NWs are centrifuged three times in water at 3000 r/min for 6 min for rinsing, and three times in desired solution (water or ethanol) at 3000 r/min for 6 min, and finally they get dispersed (Figure 3.10, Figure 3.11 and Figure 3.12).

Using track-etched polycarbonate membranes (Nuclepore) with pore diameters

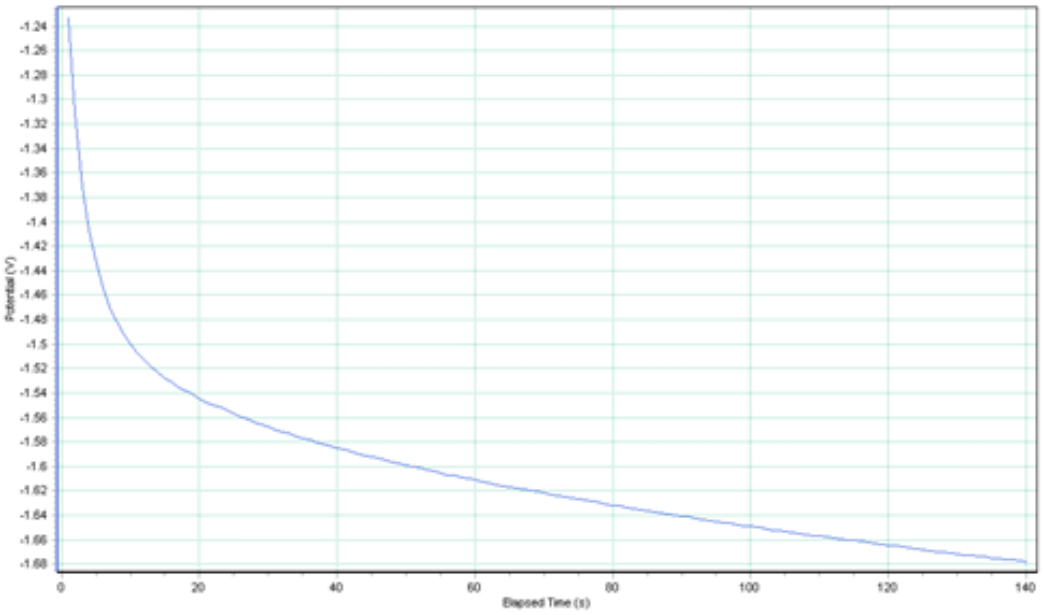

Figure 3.5: Potential trace during silver deposition into the pores of the alumina disc for Ag segments of our nanowires.

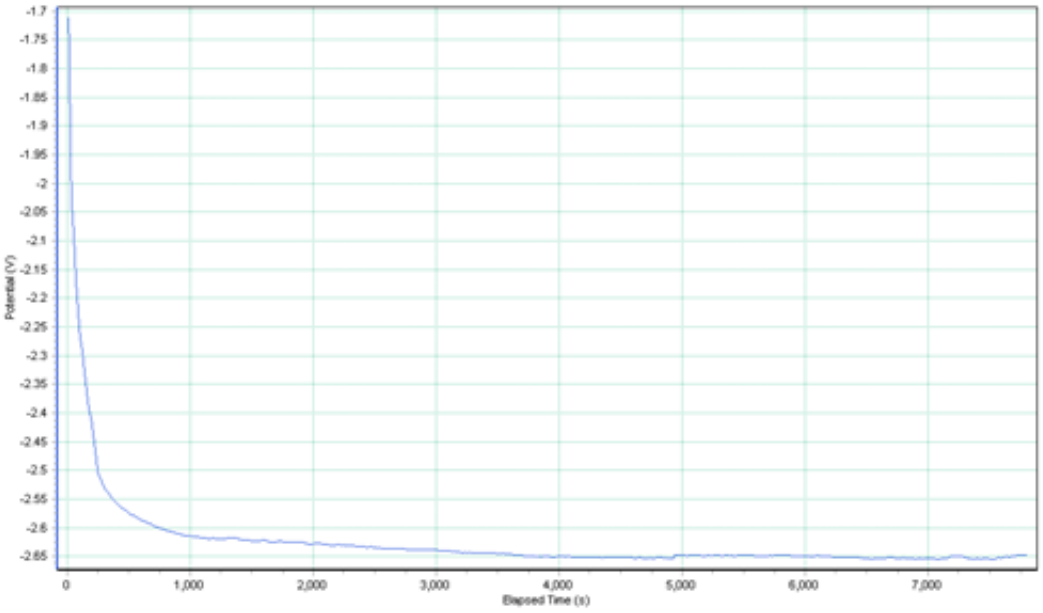

Figure 3.6: Potential trace during gold deposition into the pores of the alumina disc for Au segments of our nanowires.

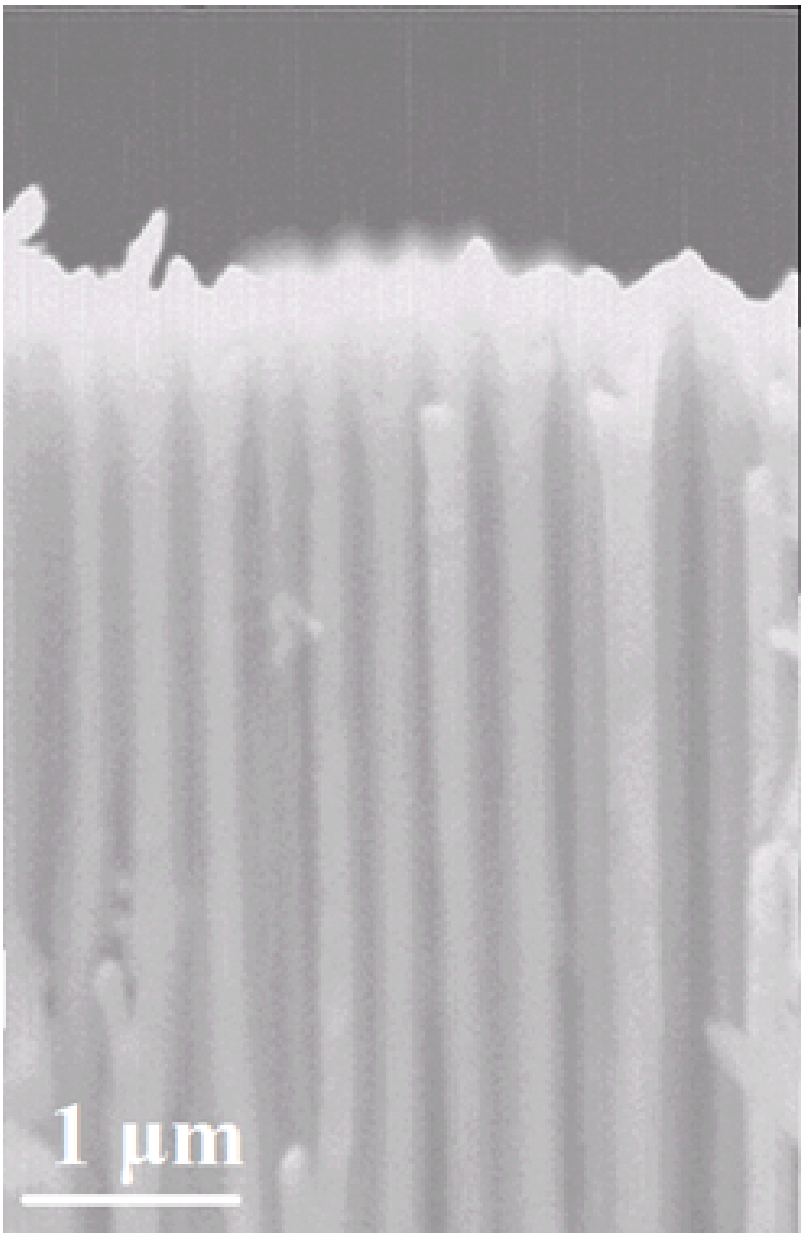

Figure 3.7: SEM image of the nanowires inside the alumina disc.

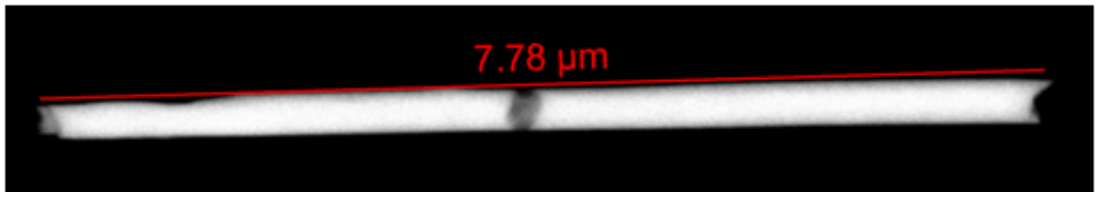

Figure 3.8: SEM image of an exemplary nanowire with a short Ag segment in the middle between long Au segments at the ends (with a total nanowire length of 7.78 μm).

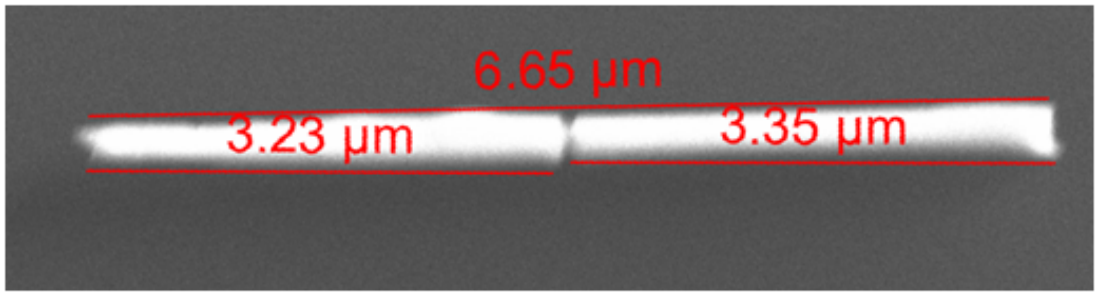

Figure 3.9: SEM image of another nanowire with 3.23 μm and 3.35 μm long Au segments.

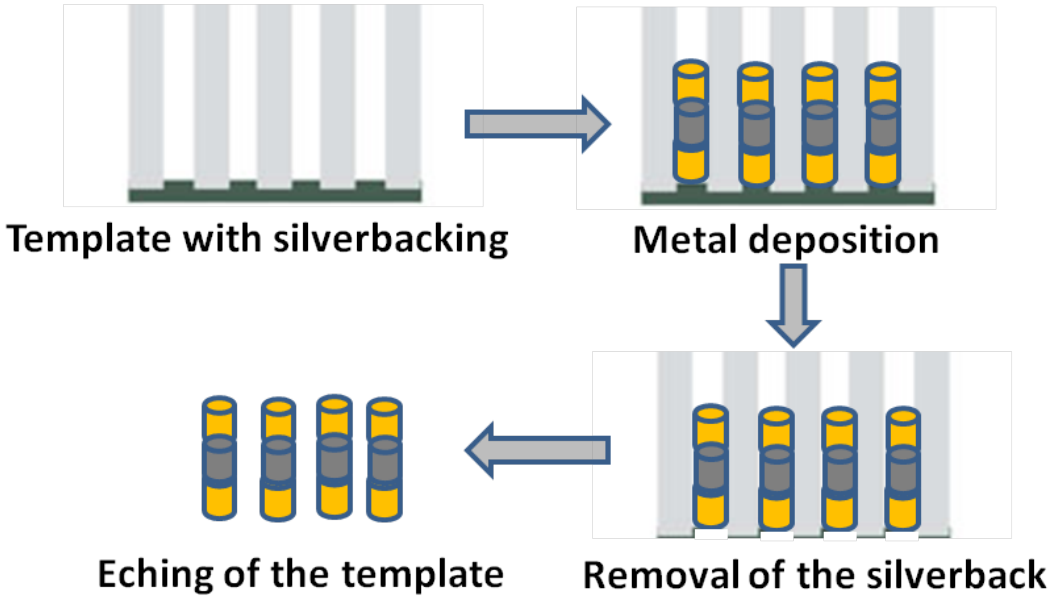

Figure 3.10: In-template electrodeposition process flow

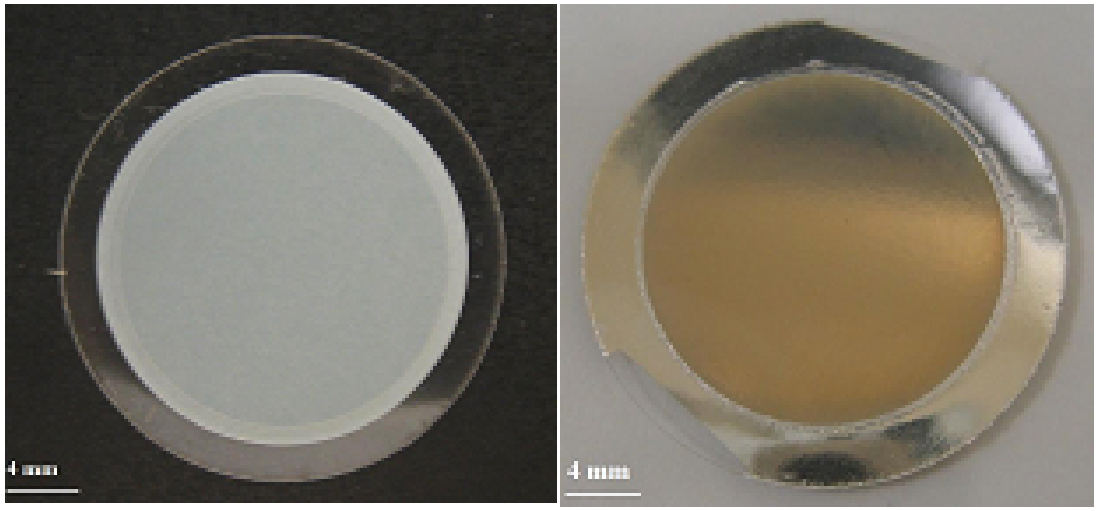

Figure 3.11: Backside of the membrane disc (a) before deposition and (b) after silver backing.

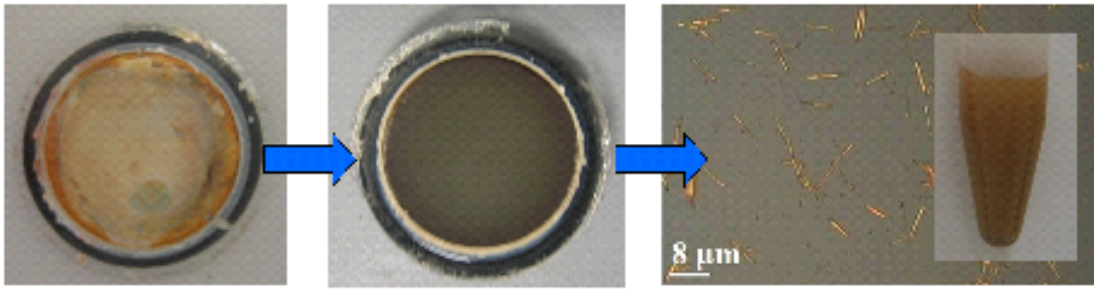

Figure 3.12: Silver backing is etched, membrane is dissolved and nanowires are dispersed inside solution.

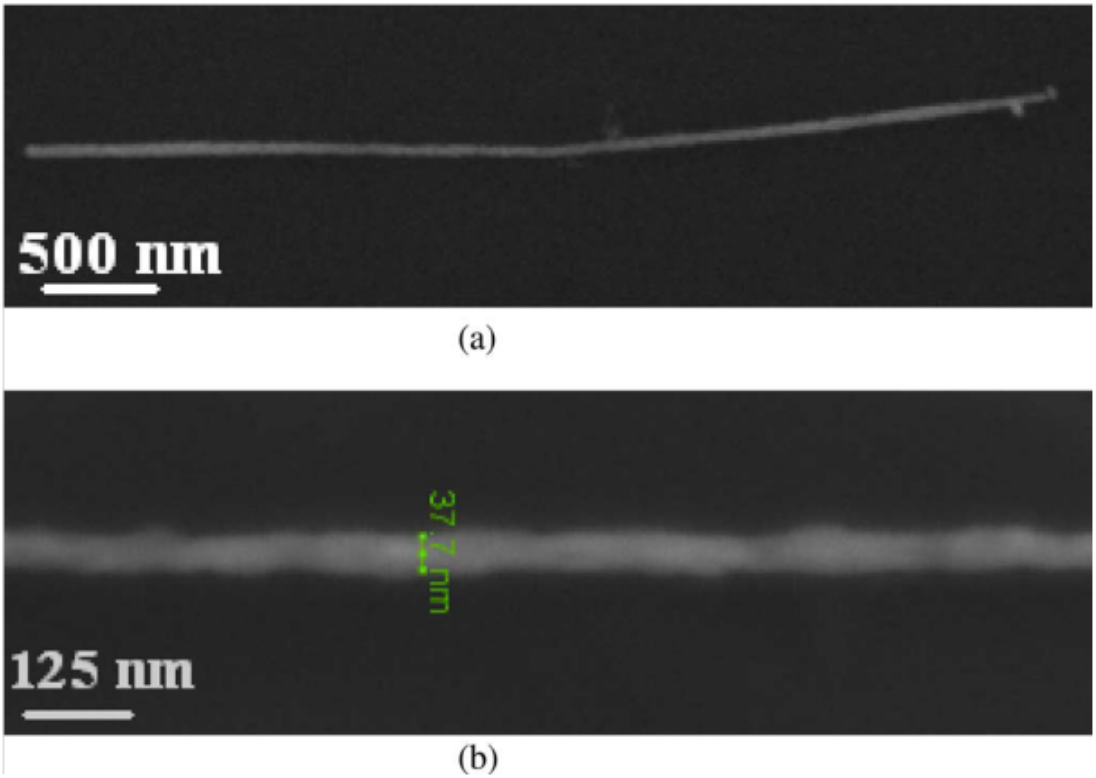

Figure 3.13: Nanowire synthesized in track-etched polycarbonate membrane (a) in full view and (b) with a zoom-in across its width.

of around 40 nm, we synthesized 6 μm long Au NWs, which have diameters of 40 nm (Figure 3.13). It is very demanding to fabricate such high aspect ratio NW structures even using e-beam lithography (EBL) and focused ion beam (FIB) technology. This in-membrane NW synthesis is, on the other hand, a highly parallel and cheap process, enabling us to synthesize our NWs in massive numbers [46].

3.2 Nanogap variation study

For varying gap formation, middle Ag segments of Au/Ag/Au NWs are removed by selective chemical etching with dilute nitric acid (HNO_3) solution and/or by postbaking process at 200 °C for 75 min due to the oxidation of Ag. Difficulties in nanogap formation are sometimes encountered due to the high tendency of Au deposition at the walls of alumina pores, forming a meniscus at the frontline of deposition. This adversely affects the morphology of the NW tips, resulting in a curved profile across the radial axis. In addition to chemical etching, baking process is also employed to remove Ag segments, and this is found to help smoothening of our nanogaps. Such thermal baking enables us to form narrower, uniform gaps, and also strengthens the electrical contacts of the gold segment ends of the NWs to the microelectrodes. Liu et al. heated the Ag segments on their own to understand its effect on NW morphology and concluded that large grains of Ag shrink in size to form smoother gaps [7]. We also characterized gap variation and showed that the length of Ag segment can be precisely controlled by the deposition time. The rate of the silver deposition is 1.5 nm/s. We synthesize Au-Ag-Au segmented NWs that include Ag segments with the lengths of 20-50-100-200-300 nm tuned controllably (Figure 3.14). Figure 3.15 shows different lengths of Ag segments [46]. The length of these Ag segments is linearly proportional to the total charge injected to the pores of the membrane disc during the electrodeposition process. As we drive constant current (I), the injected charge (Q) is also linearly proportional to the deposition time (t) of silver with the simple relation of $Q = I\ t$, which conveniently allows for controlling the lengths of Ag segments. When Ag segment is selectively chemically etched, we form a

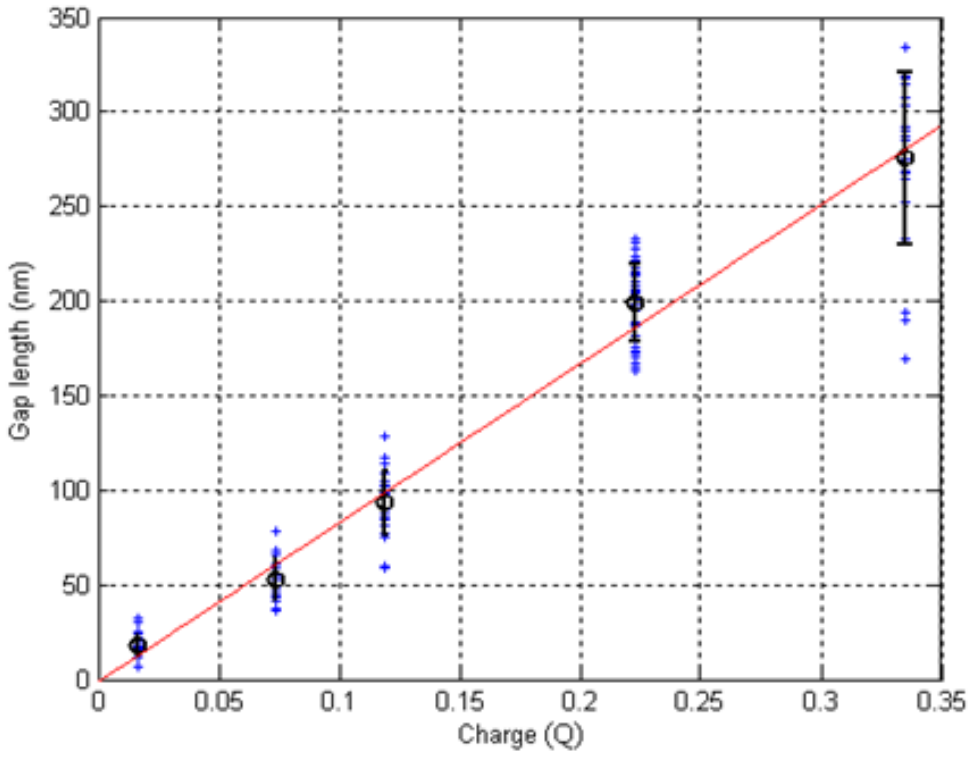

Figure 3.14: Gap length vs. charge. (Blue points represent the lengths of Ag segments, and black lines represent the standard deviation among Ag segment lengths.)

nanogap with a size equal to the size of our Ag segment. The deviation among the lengths of Ag segments stems from not being able to drive the same level of current into the pores across the entirety of the alumina disc, and this deviation increases proportionally with deposition time.

3.3 Suspended and dispersible nanostructures

It is also challenging to fabricate suspended and solution-dispersible structure by standard nanofabrication techniques such as EBL at these dimensions. EBL provides high resolution (possibly down to 10 nm) and high precision. However,

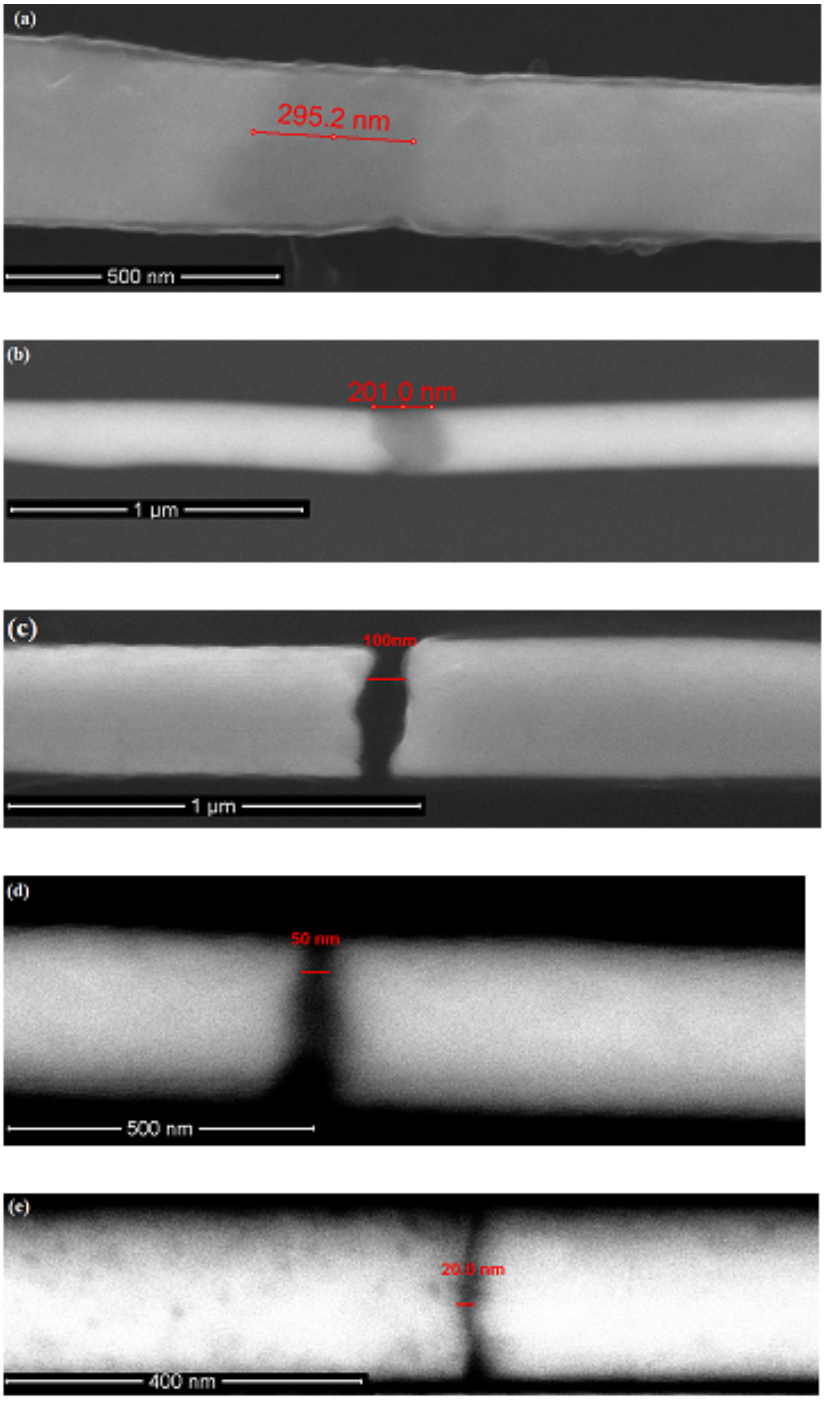

Figure 3.15: Example of Au-Ag-Au segmented nanowires with varied Ag segment lengths of 300 nm, 200 nm, 100 nm, 50 nm, and 20 nm in (a), (b), (c), (d), and (e), respectively.

EBL is a serial process where a nanostructure is patterned one at a time while in-template synthesis is massively parallel. Sioss and Keating presented a method for fabricating chains of Au and Ag nanoparticles by selective wet-etching of the alternating segments, after the wires are removed from the membrane and were coated with silicon oxide (SiO_2) by surface sol-gel method [47, 48]. They demonstrated assemblies of metal nanoparticle with desirable particle and gap sizes while those particles are kept together by SiO_2 layer. Similarly, Mirkin group reported a method for fabricating arrays of nanodiscs, which is called on-wire lithography [6]. This method uniquely combines in-template electrodepostion of different compositions of nanowires and their selective wet-chemical etching to form nanodisc arrays with gaps ranging from few nanometers to several hundred nanometers. The process relies on depositing segmented nanowires consisting of two types of materials, one of which is susceptible and the other of which is resistant to etching. Followingly, these segments were blanketed by a bridging material so that the sacrificial segments can be removed while the nanodisc array is formed with previously defined disc-widths and gap-widths. Using on-wire lithography, we prepared arrays of suspended plasmonic Au nanodiscs [49]. We used a porous aluminum oxide (Al_2O_3) membrane as the template, with a pore size of approximately 250 nm, and electrodeposited Au and Ni segments into the pores of the membrane at a driving current level of -1.6 mA, alternating Ni and Au baths (Orotemp Italgalvano), using a Versastat3 potentiostat. Ni segments served as the sacrificial layers, which determine the gap-widths between the Au nanodiscs after selective etching. Controlling the amount of charge passing through the pores of the membrane, we fabricated discs with size controllable disc-heights of 50 nm. After the deposition of each disc, the structure was annealed at 250 °C to form more uniform discs and gaps. Completing the deposition steps, the aluminum oxide membrane was dissolved in sodium hydroxide (NaOH) solution of 3 M, while the deposited segments remained together in the base solution during dissolution. Subsequently, they were centrifuged in water. Au and Ni segments were further immobilized on a glass slide by drop-casting and a 50 nm thick SiN dielectric film was deposited on them by plasma enhanced chemical vapour deposition (PECVD) at 250 °C, partially wrapping them as a blanket-layer. After the sonication of these glass slides, one side coated segments were detached from

the glass surface and dropped into solution. Sonication duration of 30 s was found critical not to damage structure with Au discs kept firmly inside the SiN support. The sacrificial Ni segments were finally selectively etched in 30% nitric acid (HNO_3) solution, leaving behind arrays of suspended Au nanodiscs kept together in a partial SiN dielectric-wrap (Figure 3.16 and Figure 3.17).

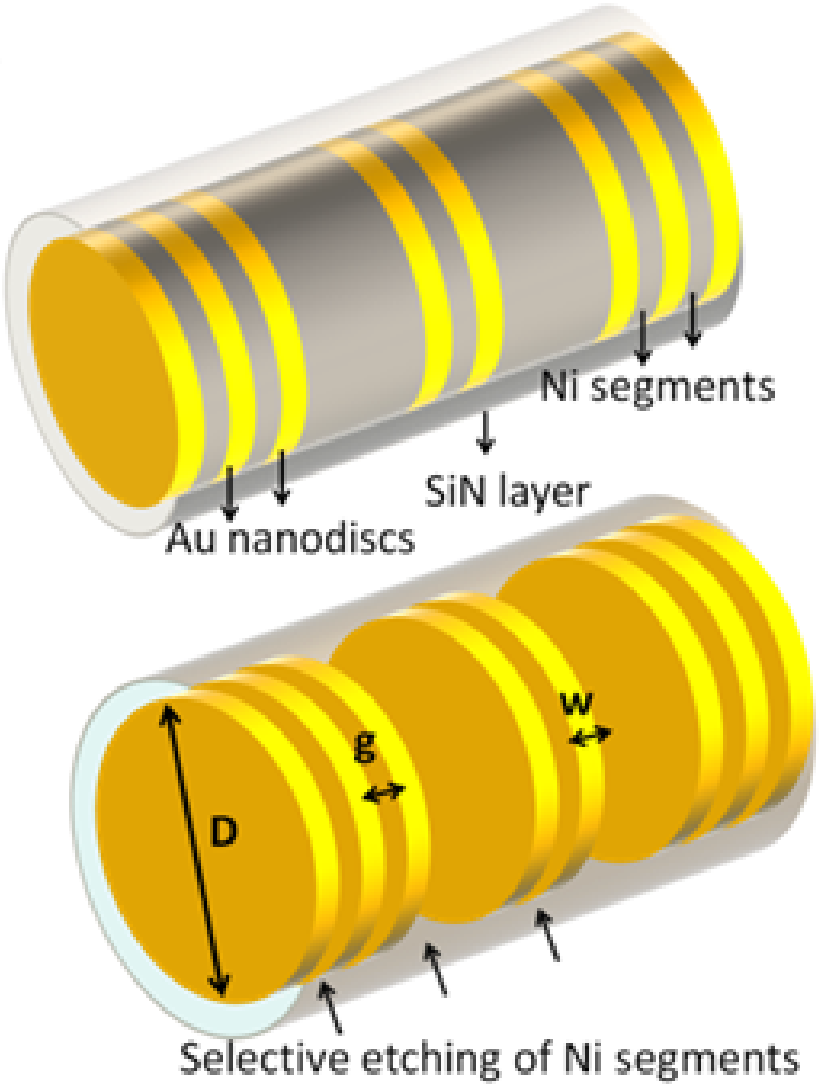

Figure 3.16: Silver backing is etched, membrane is dissolved and nanowires are dispersed inside solution.

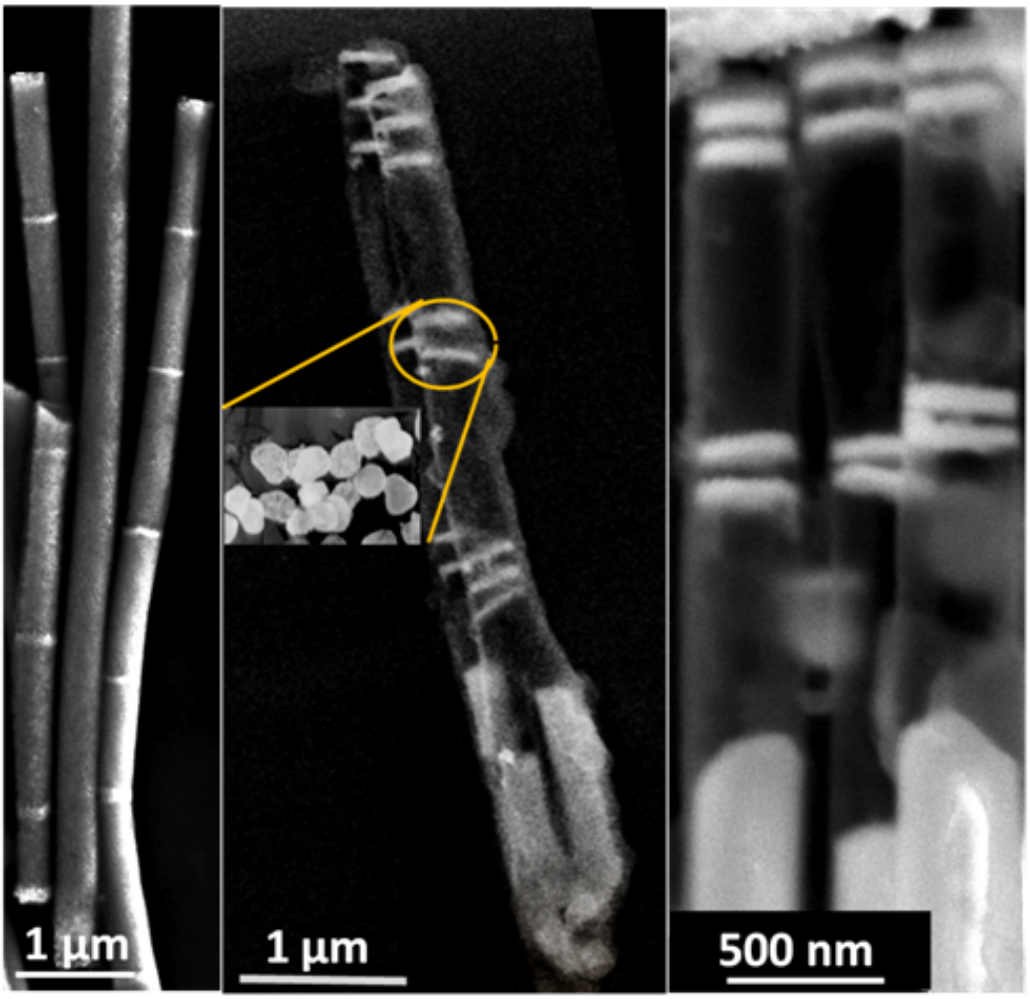

Figure 3.17: Nanowire synthesized in track-etched polycarbonate membrane (a) in full view and (b) with a zoom-in across its width.

Chapter 4

Magnetically aligned segmented nanowires integrated with isotropic nanocrystals

4.1 Introduction

Linear optical polarizers are passive components that selectively transmit the light with electric field parallel to the transmission axis (s-polarization) and block the transmission of the electromagnetic field in the orthogonal polarization (p-polarization). Polarizers are crucial for various optical systems and extensively used in applications ranging from imaging [50] and liquid crystal displays (LCDs) [51]. In the case of LCDs, an unpolarized light generated in the backlight unit is converted into polarized light via a polarizer. This polarization process contributes to the most significant loss in the LCDs. Thus, achieving polarized light-emitting sources are highly welcomed, which are expected to increase the optical efficiency of the LCDs. To date, various polarizing optical media were integrated with light-emitting materi-als to achieve polarized light sources. For example, wire-grid based polarizers [52], resonant cavities [53], plasmonic nanocavities [17], birefringent crystals [18], and liquid crystal integrated

fluorescent materials [19] can be employed to realize polarized light emission.

Wire-grid polarizers have shown very good performance in terms of the degree of emission polarization. Zhang et al. reached a vertical (s) to parallel (p) polarization contrast of 7:1 using metallic nanogratings fabricated by electron beam lithography on top of a conventional InGaN/GaN LED [20]. Ma et al. obtained an s/p polariza-tion contrast as high as 50:1, corresponding to a polarization degree of about 0.96 [21]. However, such approaches require special nanolithography techniques to achieve polarized light in the visible spectrum [52]. Sub-wavelength parallel metallic features are usually fabricated using techniques in-cluding focused ion beam lithography [54], electron beam lithography [55], and nanoimprint lithography [56], [57]. Nevertheless, these techniques are expensive, time consuming and low throughput. Alternatively, deposition of metal nanoparticles via layer-by-layer assembly was employed to realize polarized emission via utilizing the plasmonic nanocavity effect by Ozel et al. [17]. In these multi-layered plasmonic nanocavities polarized light emission with an s/p polarization degree of 0.80 was observed.

As an alternative approach, in this chapter, we show highly polarized light emission in coupled thin films of colloidal quantum dots (QDs) and magnetically aligned multi-segmented nanowires (NWs) [58]. These NWs consist of ferromagnetic (Ni) parts that enable alignment under externally applied magnetic field. In-template synthesis of these NWs together with their magnetic field assisted alignment facilitates the fabrication of massive number of highly parallel NWs over large area thin films with low cost and fast production technique. Previously, various alignment techniques have been employed including Langmuir-Blodgett [59] and external electric assisted alignment [60, 46] as well as those based on magnetic field assisted alignment [61, 62]. Among these techniques, some may require a more complex alignment setup as in the case of Langmuir-Blodgett assembly or pre-defined electrodes as in the case of electric field assisted assembly. Among these, magnetic field assisted assembly using centimeter sized commercially available magnets is a versatile tool to align NWs having ferromagnetic parts on surfaces or NWs inside a host medium without the requirement for a pre-defined electrode or surface functionalization. This makes magnetic field

assisted alignment a promising candidate for making polarizing structures.

As a proof-of-concept demonstration, here we demonstrate highly polarized emission using the isotropic emitter cadmium telluride (CdTe) QDs by integrating them with the aligned three-segment Au/Ni/Au NWs. The NWs were plated using template-assisted electrodeposition method [63] and aqueous CdTe QDs were synthesized colloidally as described elsewhere [64]. QDs represent an important class of emitters, which are highly suitable as white-light engines for backlight of the LCDs owing to their spectrally pure color emission that can be easily matched to the color filters of LCDs to boost the optical performance. The resulting hybrid system exhibited polarized emission in visible spectrum with an s/p polarization contrast as high as 15:1 corresponding to a polarization degree of 0.88.

4.2 Results and discussion

For synthesis of aqueous CdTe colloidal QDs, 4.59 g of $Cd(ClO_4)_26H_2O$ was dissolved in 0.5 L of dionized water. Subsequently, 1.33 g of thioglycolic acid (TGA) was added to the solution and the pH of the mixture was set to 12.0 by addition of NaOH. Later, 0.8 g of Al_2Te_3 was deaerated under Ar flow for approximately 60 min. Following the addition of 0.5 M H_2SO_4 onto Al_2Te_3 to produce H_2Te gas, the solution was heated until boiling point, at which temperature the nanocrystal quantum dots start to form. The reaction was continued about 20 h, at the end of which the QDs exhibited an emission peak at 625 nm. The absorption (black line) and emission spectra (red line) of the synthesized CdTe quantum dots are given in Figure 4.1.

Using the Whatman Anodisc membrane (with a pore density of 10^9 cm^{-2}) as our template, three-segment Au/Ni/Au NWs having diameters of ca. 250 nm were plated by employing electrodeposition method. Prior to the plating, a 200 nm thick silver layer serving as the working electrode was thermally evaporated on the backside of the membrane. As the counter electrode mesh platinum was

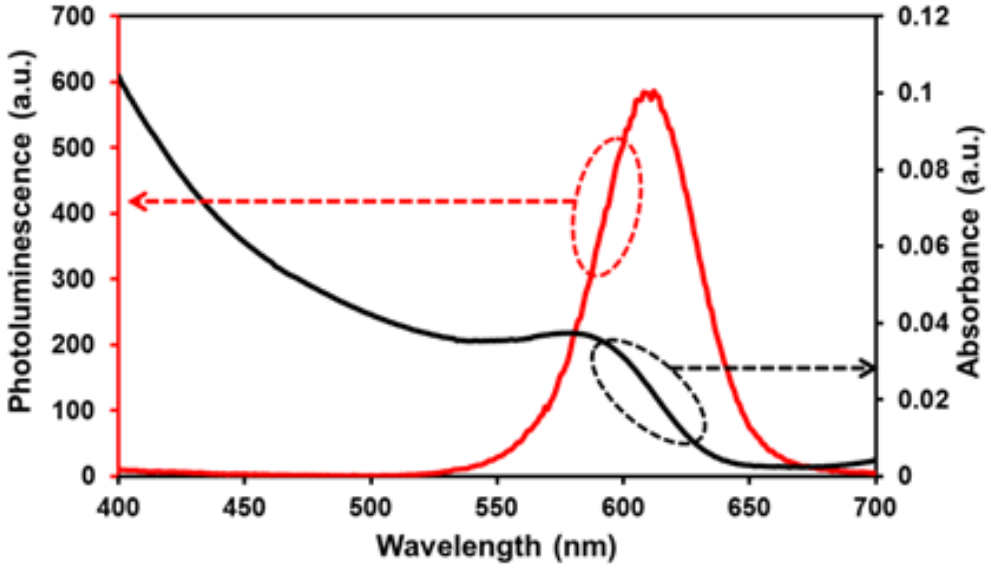

Figure 4.1: Absorption (black line) and emission spectra (red line) of the synthesized CdTe QDs emitting around 625 nm.

used and placed 5 cm above the membrane inside an O-ring glass tube. The process started with the electrodeposition of 2 μm thick silver using the silver bath (TechniSilver E-2, Italgalvano, 11.5 % potassium silver cyanide) to clog the branching portion of the membrane. For gold segments, we used Orotemp 24 (6.87 % potassium aurocyanide) and drove -1.6 mA by Versastat 3 potentiostat to deposit approximately 1.5 μm long Au segments. After rinsing, we drove -1.6 mA again to deposit nickel using the nickel bath, which is composed of nickel sulfamate (20-35 %), nickel bromide (0.5-1.5 %), and boric acid (1-3 %), to obtain 7 μm long nickel segments. The final gold segments of 1.5 μm in length were plated as in the first step following the rinsing. At these current levels, the average deposition rates of gold and nickel were 2 nm/s and 1.5 nm/s, respectively. Gold segments constituted of ca. 3 μm and the remaining 7 μm of the NWs was nickel (Figure 4.2). After deposition, the silver back-coating was etched with a nitric acid solution (HNO_3 of 30 %) and the alumina disc was dissolved in a sodium hydroxide solution (NaOH of 3M). The synthesized NWs remained in the base solution. Finally, the NWs were centrifuged three times in DI water at 3000 rpm and stored in DI water.

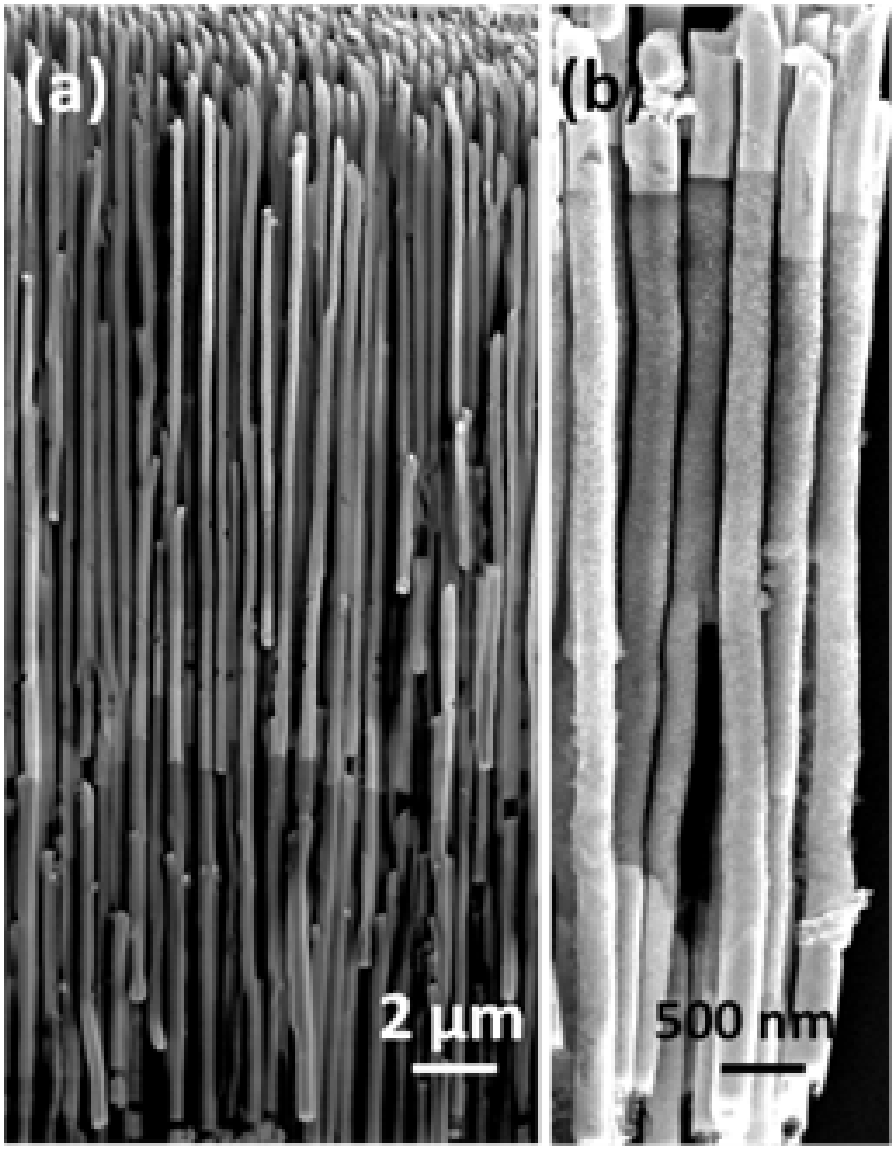

Figure 4.2: (a) Arrays of Au/Ni/Au segmented NWs inside the alumina membrane and (b) the NWs immobilized on glass after etching of the membrane.

An externally applied magnetic field enables magnetization of these NWs and helps to rotate and position them along the direction of the applied field. This is mainly due to their high aspect ratio geometry, which allows the Ni parts of the NWs to experience higher magnetization and induce magnetic charges to interact with the external magnetic field. As a result, a torque is exerted on the NWs causing them to align in the direction of the field. The induced magnetic moment (L) can be expressed using the relation L=mlHsinΘ, where m, l, H, and Θ denote the induced dipole strength, the ferromagnetic segment length, the external magnetic field, and the angle between the magnetic field and the longitudinal axis of the NW, respectively 17. Longer the ferromagnetic segment length (l) of the NWs and/or higher the external magnetic field (H), we observe a higher torque induced on the wires, thus leading to a better alignment. The aligned metal NWs constructed a grid-like architecture in which they act as a good reflector for one polarization while they transmit a higher portion of the electromagnetic field with the perpendicular polarization.

To investigate the potential of the assemblies of these segmented NWs to achieve polarized light from the QDs, we numerically investigated the hybrid architecture comprising of aligned metal NWs and CdTe QDs using finite difference time domain (FDTD) technique (Figure 4.2). Single segment NWs comprising of 10 μm long Ni were used in the simulations in addition to Au-Ni-Au three segment NWs having 1.5 μm long Au segments and 7 μm long Ni segment to understand the effects of Au segments in the polarizing effect of the obtained emission. The QD layer is modeled using the real and imaginary parts of the refractive index as measured by optical ellipsometry. In the FDTD simulations, light emitted by the QD film is assumed to pass through the aligned NW networks, each of which contain randomly positioned NWs having an average NW-to-NW separation of 250, 300, 350, and 400 nm. This randomly distributed NW matrix is along the lateral plane to account for the very large area of the sample that can be up to a few cm^2 in size. We separately investigated the parallel and perpendicular polarization that is emitted by the QDs and monitored the transmitted power for these two orthogonal polarizations.

Along the longitude of the NWs, parallel polarized electric field components of

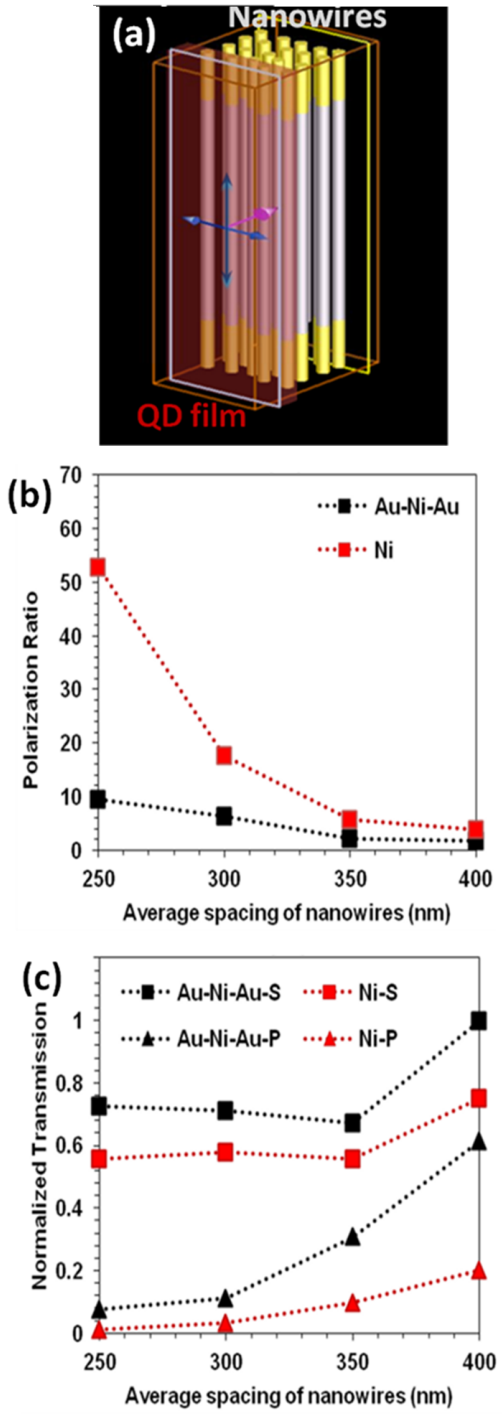

Figure 4.3: A representative image illustrating FDTD simulation structure. (b) Numerical simulation results indicating the ratio of s- and p-polarizations transmitted through Au/Ni/Au and Ni NWs at the emission peak of QDs (650 nm). (c) Normalized transmitted intensities through Au/Ni/Au and Ni NWs at the emission peaks of QDs for s- and p-polarizations.

the emitted light experiences a conductive medium and is absorbed/scattered. On the other hand, perpendicular polarized electric field components of the emitted light interact much less with the aligned NWs; thus, perpendicular polarized light is transmitted more. The results of the simulations are presented in Figures 4.3 (b) and 4.3 (c). According to these results, aligned Au/Ni/Au and Ni NWs exhibit anisotropic character (i.e., increasing s/p polarization contrast for the transmission) that is enhanced as the inter-NW distance is decreased. In the case of Au/Ni/Au NWs, polarization contrast larger than 10:1 is possible to achieve with inter-NW distance that is smaller than 250 nm. In the case of Ni NWs, a higher polarization contrast could be achieved at the expense of reduced transmitted power since Ni introduces extra loss due to their optical absorption.

For the magnetic alignment, two neodium magnets, each of 5 mm by 10 mm by 40 mm in size and generating a magnetic field of 400 Gauss, were used to align the NWs. For a proof-of-concept demonstration, Au/Ni/Au NWs were used instead of Ni NWs, which tend to break during the etching process of the silver from the back of the membranes. In addition, post thermal baking process strengthens the Au/Ni interface to keep segmented NWs robust and undamaged. To avoid quenching of the emission from the QDs and obtain an appropriate level of viscosity so that the NWs were not pulled to the sides of the film while drying, poly(vinyl pyrolidone) (PVP) was used as a host material. We prepared two different films comprising of the same amount of QDs but having different amounts of NWs. 500 μL of the multi-segmented NW in water was mixed with 750 μL of PVP, and 1600 μL CdTe QD solution was mixed with 1200 μL of PVP. The NW:PVP solutions (375 μL and 500 μL) were drop-casted on a glass substrate and left for drying overnight under magnetic field. Since PVP provides a reasonable level of viscosity, it allows for controlling the positioning of NWs as it is required for a higher polarization contrast. Furthermore, once it dries, PVP is a strong host material to keep the NWs in the orientation that they were aligned and provide a three dimensional structure where the NWs are highly aligned along one dimension. Subsequent to the deposition of the NWs, QD:PVP solution (700 μL) was drop-casted over the NW films and again the system was left for drying overnight. The hybrid film architecture and the alignment setup

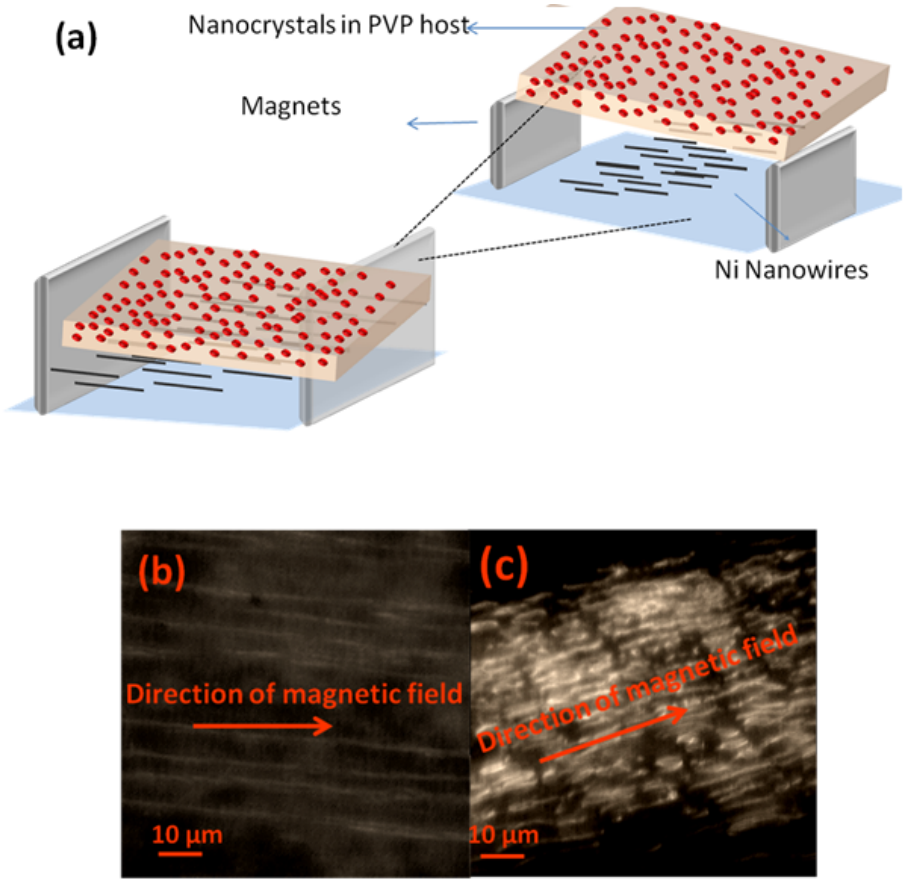

Figure 4.4: (a) Alignment during hybridization of the CdTe QDs with aligned ferromagnetic NWs in PVP host film between two Neodium magnets. Microscopy images of (b) uniformly distributed NWs and (c) dense and uniformly distributed NWs.

are illustrated in Figure 4.4 (a).

As the optical microscopy images show, the NWs were clearly aligned in the direction of the magnetic field and form a one dimensional array. The uniform alignment regions, where the NWs tend to form regular grid like structures are shown in Figures 4.4 (b) and 4.4 (c). Due to the random nature of the alignment process, non-uniformities cannot be completely avoided, which would limit the extinction ratio (i.e., the ratio of the s-polarized light to p-polarized light). However, still reasonably large values were obtained depending on the amount of the NWs as explained in the characterization section.

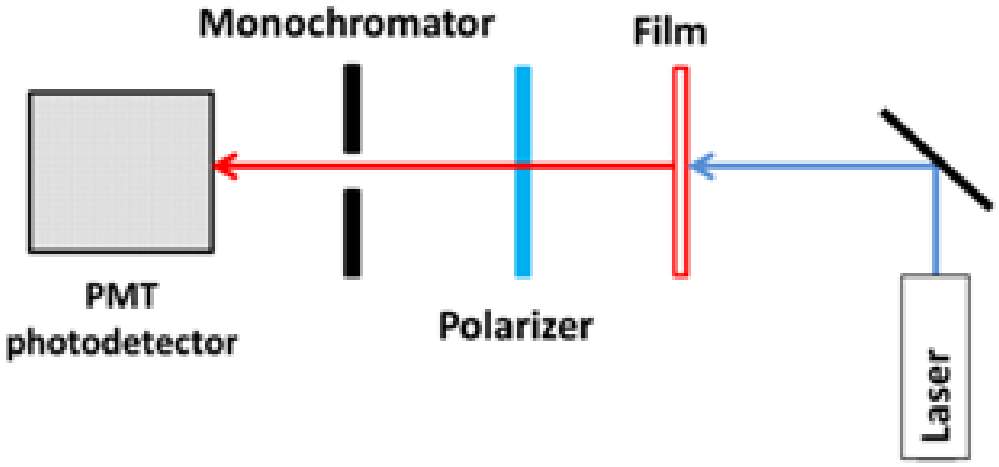

Figure 4.5: Illustration of the characterization setup for the polarization degree of the QD integrated aligned NW films.

Our optical characterization setup is illustrated in Figure 4.4. These QD integrated NW hybrid films were excited using a laser diode emitting at 375 nm. The emitted light by the QDs was collected through a linear polarizer, a monochromator and a photomultiplier tube. The emission intensity of the QDs was recorded as the polarizer is rotated to measure the perpendicular and parallel polarization components of the light emitted by the QDs that is transmitted through the NWs.

When bare CdTe QDs were employed, which were not integrated to the NWs, unpolarized light is emanated at a peak emission wavelength of 650 nm in solid film. The s/p polarization contrast is close to 1:1 when the QDs are decorated on top of two different NW films having different film thicknesses (375 and 500 μL of NW:PVP). The emission intensities of the QDs collected by the detector after the polarizer in s- and p-polarizations at the receiver end are presented in Figure 4.6 for the thin and thick NW matrices. The blue curves in Figure 4.6 show the s/p polarization contrast as a function of the wavelength. Our results reveal that aligned NWs in PVP matrix substantially polarizes the emission of the QDs. For the thin NW:PVP sample, the s/p polarization contrast reaches 10:1, while it gets at 15:1 for the thicker NW:PVP sample. We attribute this to the increased number of aligned NWs that enhance the polarization contrast. We

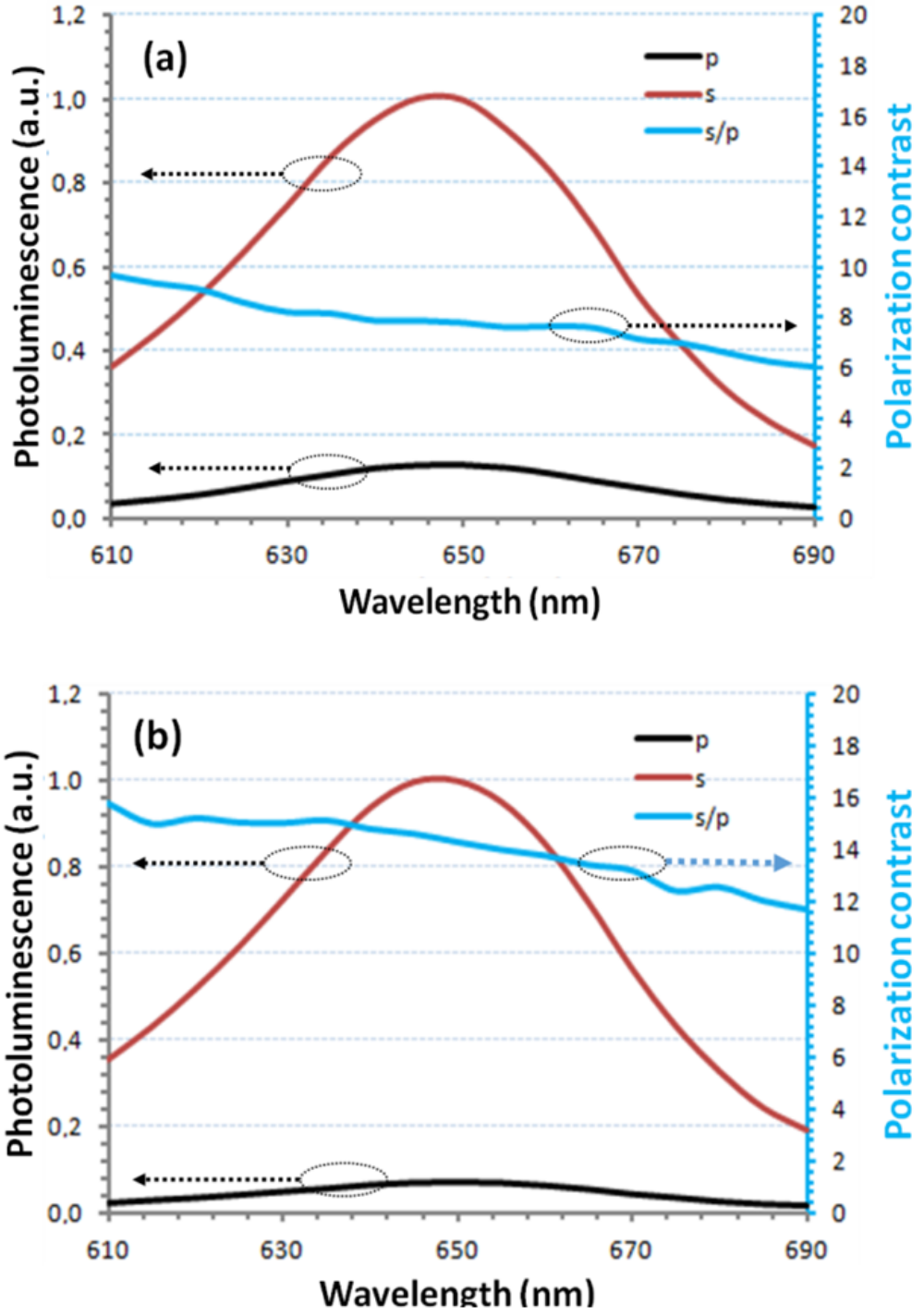

Figure 4.6: Photoluminescence spectra intensity of the QDs integrated on the NW:PVP samples in s- and p- polarizations (red and black lines) along with the s/p contrast (blue line) from (a) the thinner and (b) the thicker NW:PVP films. The maximum contrast of the s/p polarizations was found to be 10:1 for the thinner film and 15:1 for the thicker one.

further observe that the contrast of the optical polarizations has a slowly varying trend with respect to the wavelength. We attribute such a large bandwidth of the polarization contrast due to the random nature of the hybrid films, where the distribution of aligned NWs is not perfectly uniform within the film.

4.3 Conclusion

In summary, we proposed and demonstrated a proof-of-concept hybrid thin film system for the generation of polarized light with a contrast of polarizations perpendicular to parallel larger than 15:1 in the visible range by employing multi-segmented NWs having ferromagnetic parts, which are well aligned under external magnetic field. The proposed approach makes use of a much cheaper and easier fabrication procedure compared to the conventional expensive fabrication techniques. Furthermore, we verified the experimental results of highly polarized light generation by FDTD simulations, which revealed the relation between inter-NW distance and the achieved polarization contrast.

Chapter 5

Arrays of suspended plasmonic nanodiscs

5.1 Introduction

Plasmonic structures enable enhanced light utilization for optoelectronic devices owing to their unique, strong and tunable electric field localization leading to increased scattering and absorption properties [1, 2, 3]. Various nanopatterned plasmonic structures have been proposed to date, which typically use the nanofabrication method of electron beam lithography (EBL) or nanoimprint lithography [4, 5]. Although these techniques offer high resolution and allow for a more deterministic nanostructure layout for plasmonics, these technologies are quite costly and limited in high throughput. Alternatively, solution processed nanostructures have emerged, for example, metallic nanodiscs, which are synthesized using in-template electrodeposition [46, 65], followed by simple selective etching of sacrificial metal layers. These nanodiscs are promising for nanoplasmonics because their optical properties may be fine-tuned either via the disc-gap or the disc-width [13, 12, 66]. The spectral line shape of the localized surface plasmon (LSP) resonance of a metallic nanoparticle, as obtained when measuring absorption, or scattering cross sections as a function of photon energy, depends on the

material and particle size. These absorption and scattering mechanisms determine the local field enhancement around the plasmonic nanoparticles, which are important issues in sensing [67], surface enhanced Raman spectroscopy (SERS) [8] and plasmon enhanced fluorescence [11].

In this chapter, we demonstrate lateral arrays of Au nanodiscs with controlled disc-gap and disc-width, which can range from 20 nm to several hundred nanometers using the in-template synthesis to allow for the tailoring of the scattering properties [49]. This has resulted in massive numbers of easily and inexpensively fabricated arrays of nanodisc structures. The achievable resolution of our fabrication approach reaches down to approximately 20 nm. Fabricating such three-dimensional suspended and liquid dispersible architectures is not easily possible by other techniques such as EBL. Here, we report the plasmonic properties of these suspended nanodisc structures including the polarization-dependent scattering spectra as a function of disc-gap/-width parameters computed numerically and measured experimentally.

5.2 Results and discussion

We study the polarization dependent absorption and scattering properties of the nanodisc arrays presented in Figure 5.1. We model our discs to tailor the light spectra scattered from these Au discs with varying disc-widths (w) for different disc-gaps (g) (Figure 5.2 (a)). Under unpolarized illumination incident on discs, we observe different scattering spectra with respect to the position of the polarizer with respect to nanodiscs. Figures 5.2 (b) and (c) present the computed quality scattering factors of the nanodisc array for polarization normal and parallel to the discs by finite-difference time-domain (FDTD) simulations. Here the disc diameter (D) is 250 nm, which is the membrane pore size of our template used during electrodeposition.

For polarization normal to the discs, we observe strong plasmonic coupling depending on the gap size (g) between the discs. The electric field localized between

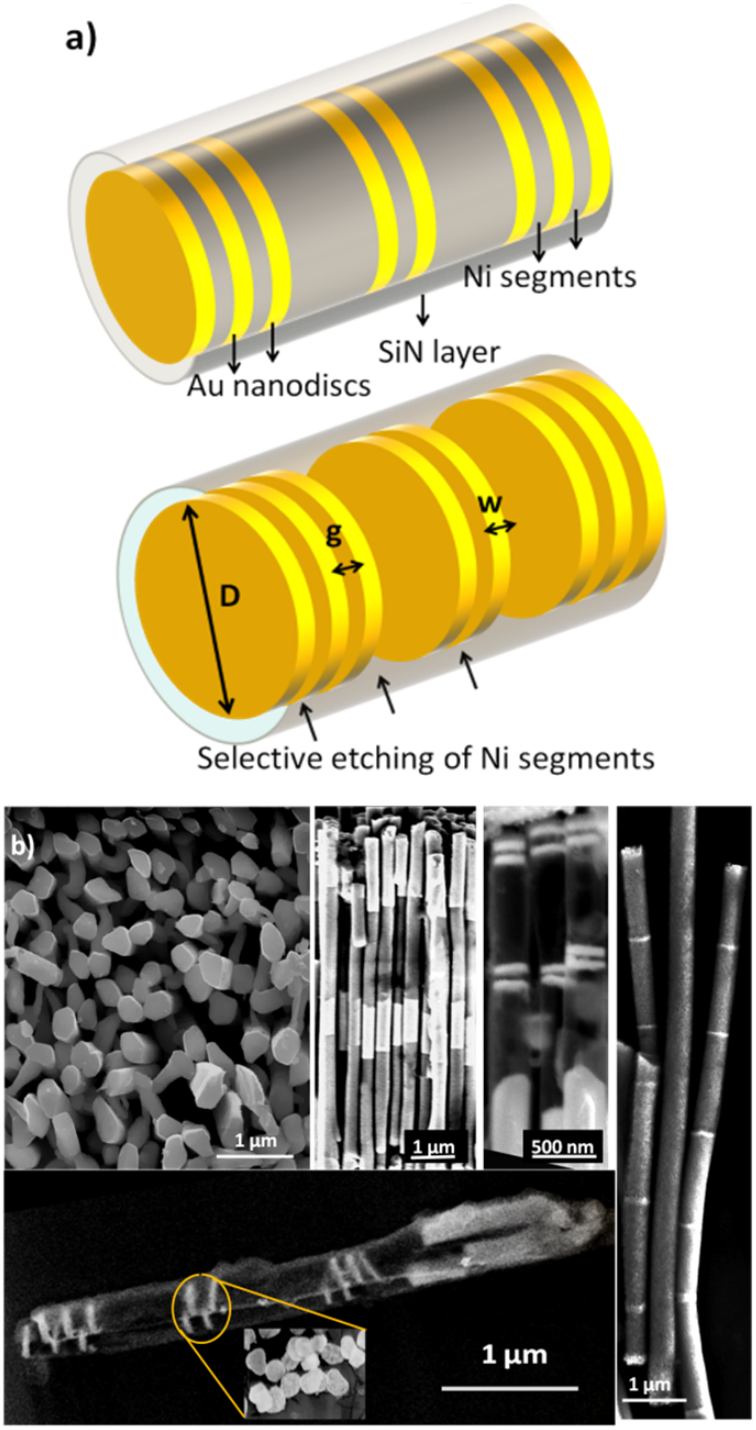

Figure 5.1: (a) Illustration of the suspended plasmonic nanodisc array fabrication using in-template synthesis. (b) SEM images of the suspended gold nanodisc array fabrication steps from in-template synthesis of segmented nanowires to selective etching of Ni segments leaving behind arrays of suspended gold nanodiscs inside SiN dielectric-wrap.

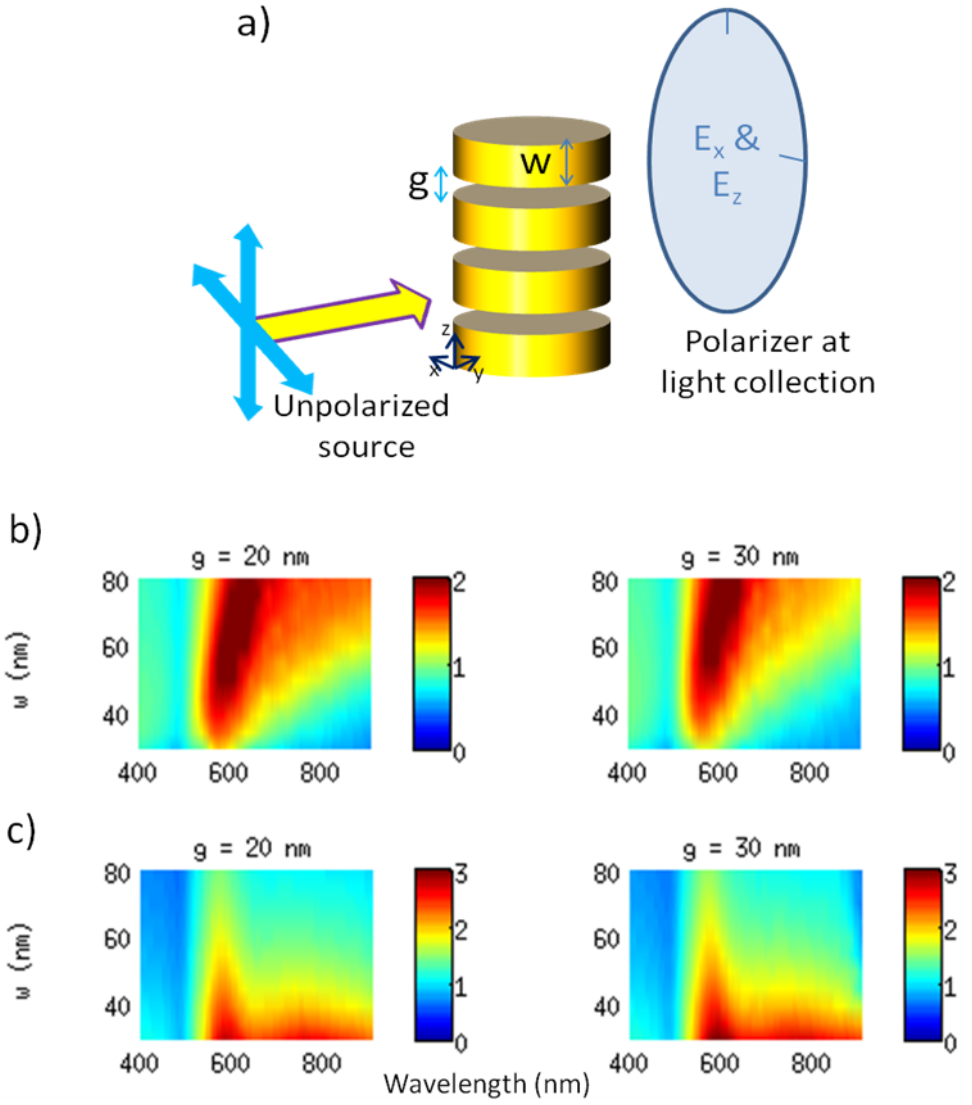

Figure 5.2: (a) A representative image indicating FDTD simulation structure. Scattering quality factor under unpolarized illumination: (b) Strong plasmonic coupling (at shorter wavelengths) depending on the gap-width (g) for polarization normal to nanodiscs. (c) Weak coupling (at longer wavelengths) between the discs for polarization parallel to the discs for varying disc-width (w).

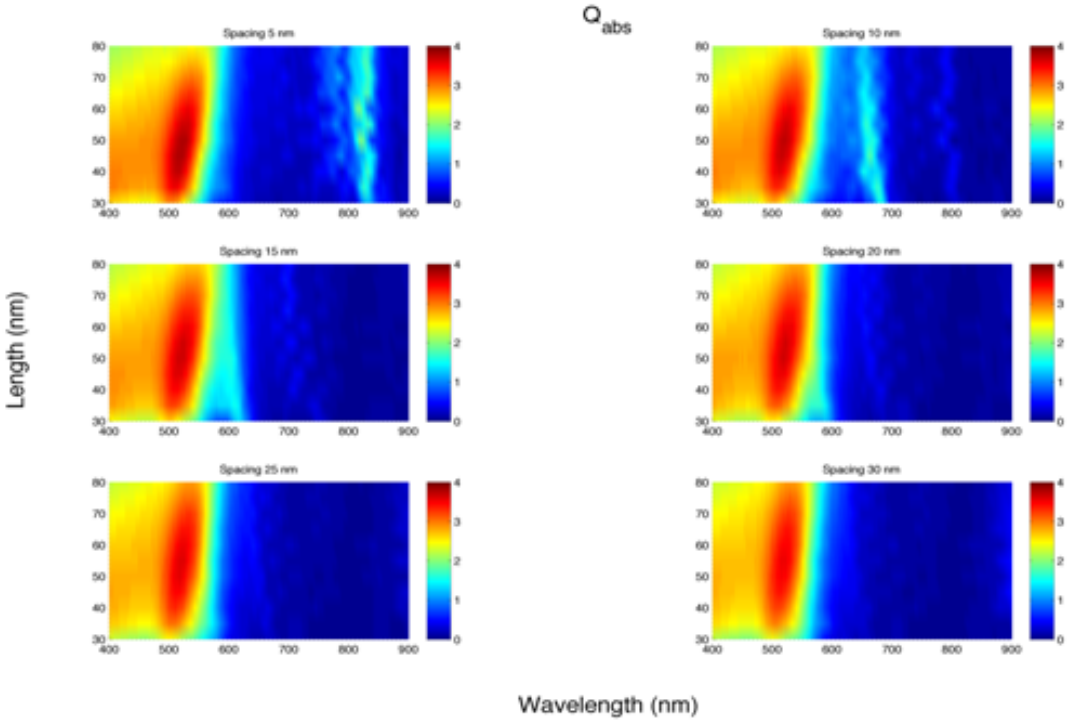

Figure 5.3: Absorption quality factor of the nanodiscs vs. their gap-width. Strong plasmonic coupling is observed at longer wavelengths depending on the gap-width.

the discs is found to increase with this coupling. We observe a scattering peak at shorter wavelengths in Figure 5.2 (b) with a disc width (w) of approximately 50 nm and above. However, in the case when the polarization is horizontal to discs, we do not observe strong coupling between the discs in that direction. With 250 nm disc diameter (D), we observe scattering at longer wavelengths in Figure 5.2 (c).

Absorption and scattering quality factor of the nanodiscs vs. their gap-width. Strong plasmonic coupling is observed at longer wavelengths depending on the gap-width (Figures 5.3, 5.4 and 5.5).

For the in-template synthesis of the gold nanodisc array, we used a porous aluminum oxide (Al_2O_3) membrane as the template, with a pore size of approximately 250 nm, and electrodeposited Au and Ni segments into the pores of the membrane at a driving current level of -1.6 mA, alternating Ni and Au baths

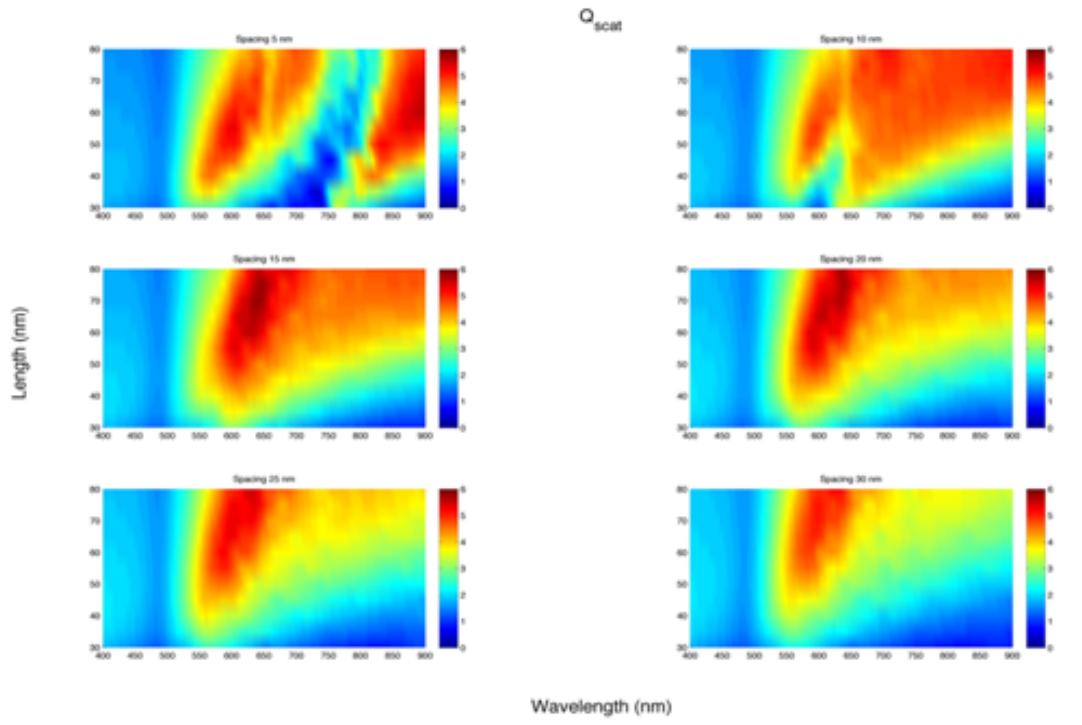

Figure 5.4: Scattering quality factor of the nanodiscs vs. their gap-width. Strong plasmonic coupling is observed at longer wavelengths depending on the gap-width.

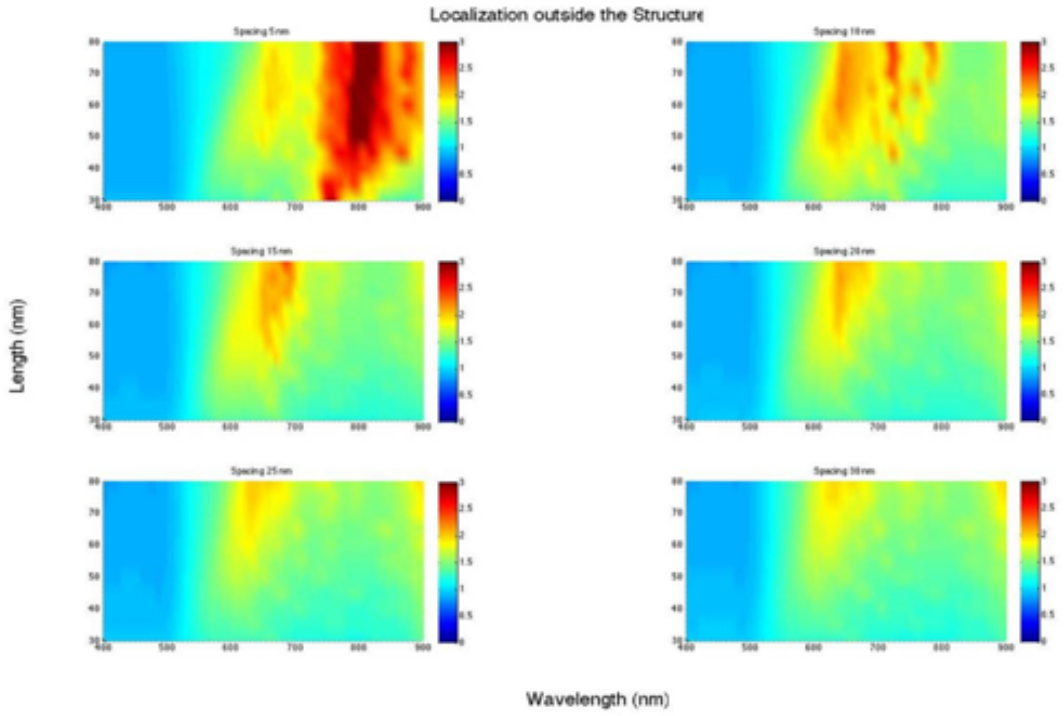

Figure 5.5: Localized electric field outside the nanodiscs vs. their gap-width. Strong plasmonic coupling is observed at longer wavelengths depending on the gap-width.

(Orotemp Italgalvano), using a Versastat3 potentiostat (Figure 3.1). Ni segments served as the sacrificial layers, which determine the gap-widths between the Au nanodiscs after selective etching. Controlling the amount of charge passing through the pores of the membrane, we fabricated discs with size controllable disc-widths of 50 nm.

After the deposition of each disc, the structure was annealed at 250 °C to form more uniform discs and gaps. Completing the deposition steps, the aluminum oxide membrane was dissolved in sodium hydroxide (NaOH) solution of 3 M, while the deposited segments remained together in the base solution during dissolution. Subsequently, they were centrifuged in water. Au and Ni segments were further immobilized on a glass slide by drop-casting and a 50 nm thick SiN dielectric film was deposited on them by plasma enhanced chemical vapour deposition (PECVD), partially wrapping them as a blanket-layer. After the ultrasonication of these glass slides, one side coated segments were detached from the glass surface and dropped into solution [49]. Ultrasonication duration of 30 s was found critical not to damage structure with Au discs kept firmly inside the SiN support. The sacrificial Ni segments were finally selectively etched in 30% nitric acid (HNO_3) solution, leaving behind arrays of suspended Au nanodiscs kept together in a partial SiN dielectric-wrap (Figure 3.1 (b)).

We present the measured scattering spectrum from the nanodiscs on quartz in (Figure 5.6). For polarization normal to discs, we observed scattering stronger in the short wavelength range and weaker in the long wavelength range (blue line). On the other hand, for polarization parallel to discs, we observed scattering stronger in the long wavelength range and weaker in the short wavelength range (red line). Compared to the computed scattering spectra, the red-shift in the experimental data stems from the nanodiscs being placed on quartz substrate in the experimental measurements.

Using suspended plasmonic nanodisc arrays, we observed the vertical and horizontal components of the scattered light sensitive to the disc size parameters such as width, diameter and gap. These developed plasmonically tunable nanostructures offer applications in photodetection with polarization sensitivity. As

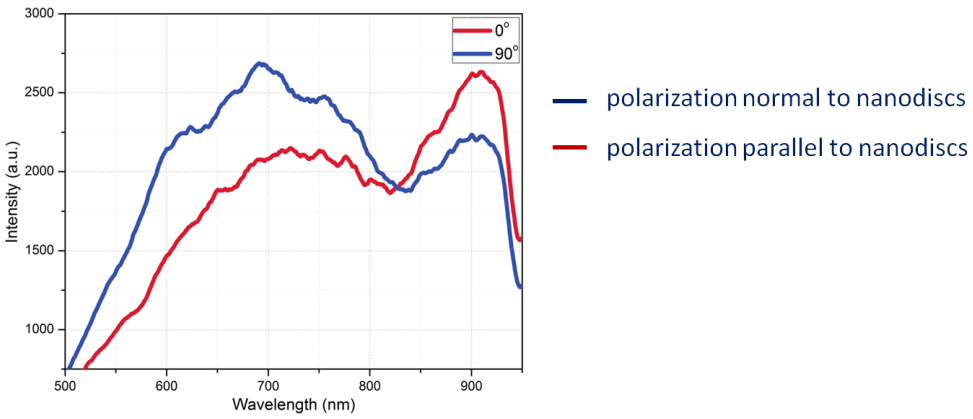

Figure 5.6: Strong scattering at shorter wavelengths for polarization normal to discs and strong scattering at shorter wavelengths for polarization parallel to discs.

mentioned before in this chapter, solution processed colloidal nanoparticles such as nanocrystals (NCs) [68, 69] and metallic nanodiscs (NDs) [13, 12] are very promising for optoelectronic devices such as light-emitters, sensors and scintillators due to their light tunability and faciliability for integration with nanostructures on any type of substrate over large areas [22, 23]. In previous works [70], light-sensitive nanoskin devices (LS-NS), which are operating on the basis of photogeneretaed potential build-up rather than conventional charge collection devices with thick ($>$ 100 nm) active layers. In operation, electron-hole pairs created in the NC quantum dots (QDs) of the LS-NS are dissociated at the NC monolayer metal interface in the absense of external bias. In addition, noise generation is remarkably lowered due to the very thin NC monolayer.

Gold (Au) nanodiscs with disc-widths of 50 nm, embedded into the LS-NS devices enhance the sensitivity in a specific wavelength range depending on the thickness and diameter of the nanodisc (Figure 5.7). Free electrons confined inside metallic nanoparticles can be excited under electromagnetic radiation. These collective charge oscillations excited by light are called plasmons. At the resonance, evanescent fields are few orders of magnitude strong in the close vicinity of Au nanodiscs. As a result, this field enhancement increases the optical absorption and electronhole pair generation inside nanocrystals (NCs) which are assembled on Au nanodiscs by dielectric spacer [71, 72, 73].

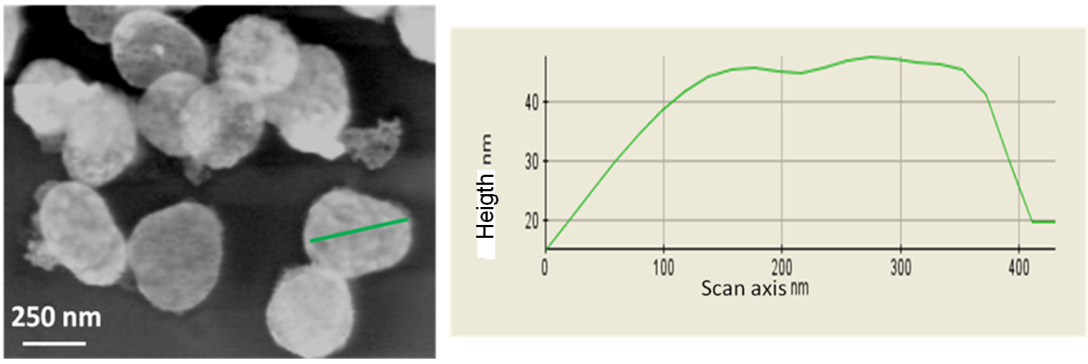

Figure 5.7: (a) Au nanodiscs immobilized on a substrate and (b) AFM topography of a single disc along the diameter.

The proposed plasmonic photosensor relies on the photogenerated voltage buildup rather than the photogenerated charge collection out of the device. For this reason, the plasmonic enhancement in the close vicinity of gold nanodiscs embedded inside the LS-NS device promote dissociating excitons at the NC/Al interface, which determines the performance of the photosensor response. The absorption needs to be increased in the QDs for higher photovoltage buildup. Thus, any other increased absorption without contributing to this voltage buildup would be considered as loss for the device performance.

ITO coated glass substrates are sonicated to be cleaned in a mixture of 2 mL Hellmanex in 100 mL water for 15 min, followed by subsequent washes inside dioinized water, acetone and isopropanol for 15 min. A 100 nm thick HfO_2 dielectric film is deposited on the substrate via atomic layer deposition (ALD). Nanodiscs are uniformly drop-casted on the dielectric film, which are subsequently blanketed by sputtered 3 nm HfO_2 dielectric film with ALD as the spacing between the metal nanodiscs and semiconductor QDs affect the strength of the plasmonic coupling and the resulting enhancement factor. This spacing is carefully handled to prevent the restraint of charge accumulation. Afterwards, we used layer-by-layer assembly by dip coating to deposit NCs. We found that the formation of 4 bilayers of polydiallyldimethylammonium chloride and polysodium 4-styrenesulfonate (PDDA - PSS) gives a uniform film for the subsequent cadmium telluride (CdTe) NC monolayer. After each self-assembly step, the sample is rinsed inside water to remove unbound molecules on the substrate.

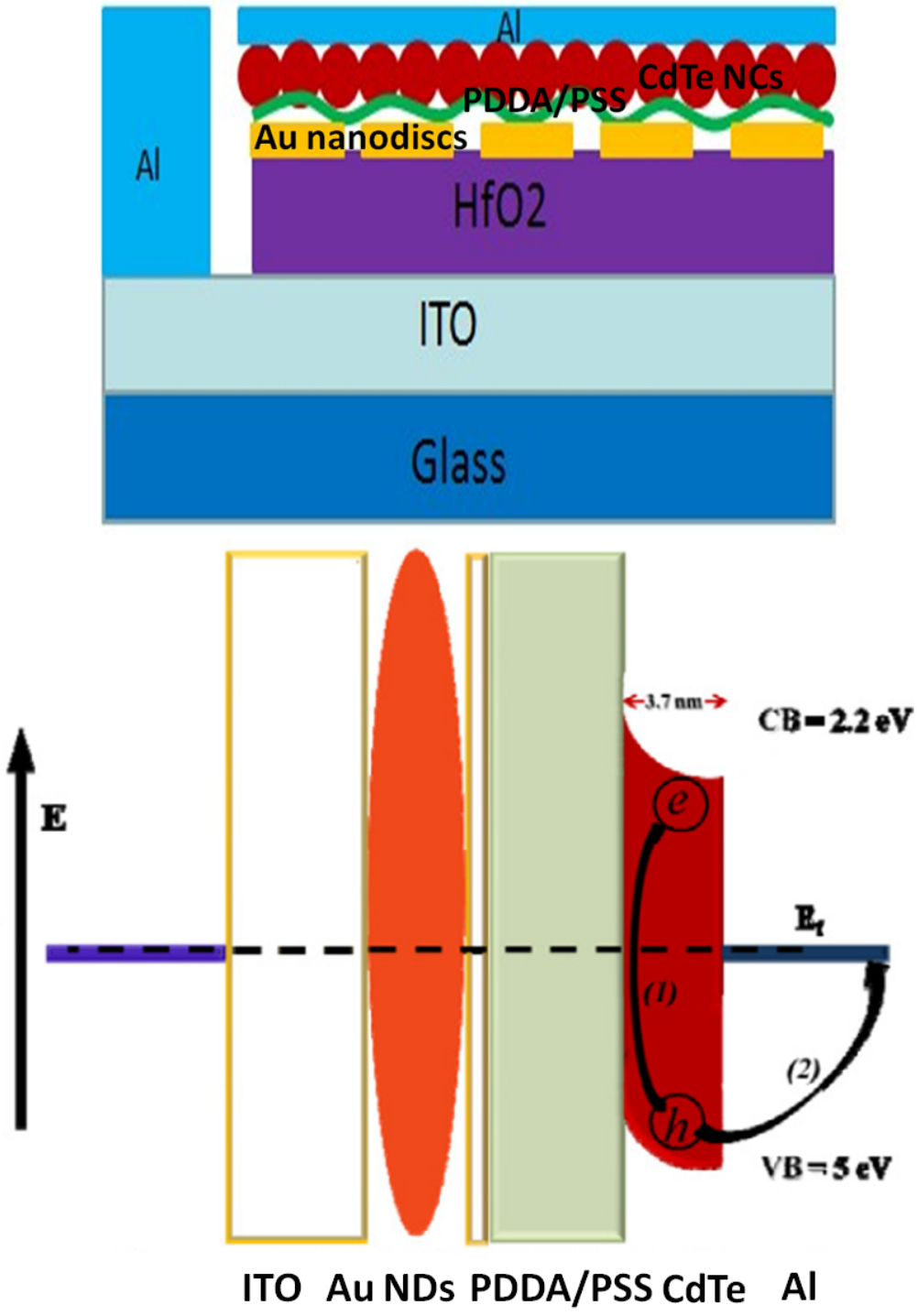

Figure 5.8: Plasmonic Au nanodiscs embedded LS-NS device with energy band diagrams.

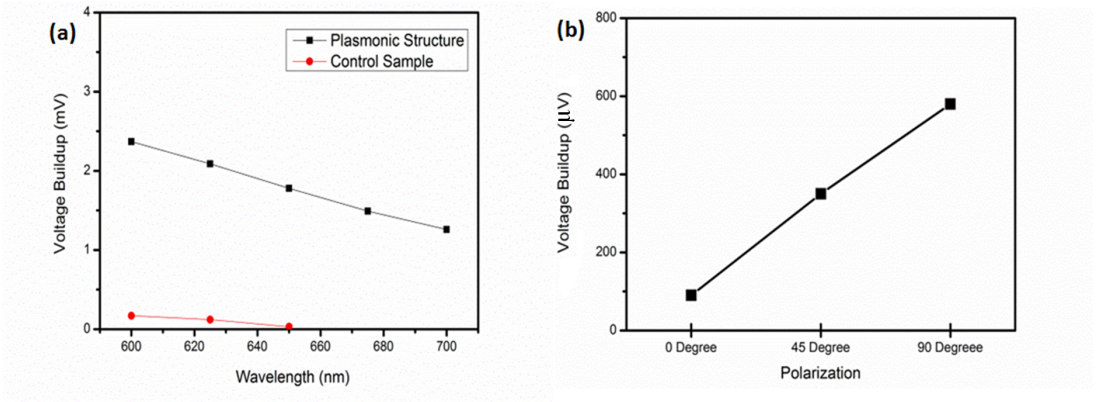

Figure 5.9: Plasmonic Au nanodiscs embedded LS-NS device with energy band diagrams.

Lastly, Al contact layer of 15 nm in thickness, which is semi-transparent, is carefully coated on top of the CdTe NC monolayer by thermal evaporation. In our measurements, we illuminate our device on substrate side by xenon light source integrated by a monochromator. The illumination intensity was measured with Newport optical powermeter . In operation, the devices were connected to a shunt resistor of 300 MΩ for sufficient voltage build-up, which is measured by Agilent B1500A parameter analyzer (Figure 5.8).

For LS-NS device with Au NDs (in black), we observe higher voltage build-up compared to LS-NS devices without NDs (in red) for wavelength range 600-700 nm (Figure 5.9 (a)). In Figure 5.9 (b), we observe polarization dependent voltage buildup for polarizer position with respect to nanodiscs at the fixed wavelength of 675 nm. With polarization normal to the discs, voltage buildup is enhanced compared to the case when the polarization is parallel to discs.

5.3 Conclusion

We proposed in-template electroplated suspended plasmonic nanodisc arrays with tunable width and gap. We demonstrated that these arrays of suspended nanodiscs exhibit polarized light scattering as a function of disc-gap/-width parameters.

Chapter 6

Large-area photosensors of nanocrystals

6.1 Introduction

Solution-processed colloidal semiconductor nanocrystals (NCs) are praised for their color tuning, large-area surface coverage and the possibility for low cost fabrication of flexible electronics [74]. These properties promote them to be selected materials for the photoactive absorbing layer in photosensors [75]. The photosensitivity of solution-cast NC photodetectors, either photoconductor [76] or photodiode type [24] is quite impressive with high photoconductive gain and low noise.

Conventional NC-based photosensors, with ultrasensitive and fast detection, are reported in literature [25, 23]. Such photosensors require an externally applied potential difference to collect the photogenerated charges. Principally, operation without an external bias is possible resulting lower sensitivity levels. However, they are usually operated under negative bias and show high dark current, again causing high noise and low sensitivity. Furthermore, the required external bias may affect the photoactive layers causing defects that lead to device

degradation.

Even though the overall performance efficiency of photosensors is crucially dependent on the ratio of photons absorbed in the photoactive layer, there is a compromise for the thickness of this layer, which is still a remaining challenge in the electronic properties of NC solids. Indeed, the active region thickness is restricted in the order of, or considerably less than, 100 nm due to the relatively short minority carrier diffusion length within NCs [77]. Therefore, in order to enhance the absorbance, increasing the film thickness is not a good approach since it may exceed the diffusion length [78]. Similarly, thick film reduces the device transparency and influences the noise generation-recombination. Thus, the use of a thin film based photoactive layer is especially advantageous for avoiding the self-absorption effect.

In this chapter, we present a new device structure to overcome the aforementioned challenges for solution processed light-sensitive devices. Here, highly photosensitive nanocrystal skins (PNSs) are achieved by dip-coating a monolayer of UV-vis active CdTe NCs and UV-vis-near infrared (NIR) active CdHgTe NCs on top of large-area flexible plastics [30]. Using a NC monolayer and few nanometers (8 nm) aluminum (Al) as an electrode, a semi-transparent tandem PNS is obtained. Owing to the monolayer of NCs in the active area of the device, noise signal is notably reduced, which results in high sensitivity [70]. In operation, photogenerated excitons are not allowed to pass directly through the device. With exciton dissociation because of the difference between the work functions of the NCs and the metal contact, holes move to the metal contact while most of the electrons are trapped inside the NCs, resulting in a potential buildup across the device. When light irradiates the PNS, it passes through the monolayer of NCs with very little absorption. Although a monolayer of NCs is sufficient to accumulate the charges for photovoltage buildup, decreasing the active layer thickness down to a single NC monolayer for absorbing incident light may result in performance drop. In this type of devices, higher sensitivity can be obtained if the absorption of the photoactive layer is increased. It was previously reported that by adapting a thick photoactive NC layer, a much lower photovoltage buildup was observed, which was attributed to the self-absorption effect [79]. Another work

on the PNS devices demonstrated that enhancing the absorption of the photoactive layer via plasmonic nanoparticles increases the PNS sensitivity, but limits the operating wavelength range of the device on localized plasmonic resonance band [71].

Here we demonstrate a tandem PNS (Figure 6.1). It is composed of two constituent junctions, each consisting of a single NC layer. The operation of the tandem PNSs relies on the Schottky barrier between the monolayer of NCs and Al contact in each junction. Usage of a single NC monolayer as the photoactive layer in each junction significantly reduces the noise generation and recombination, which further enhances the sensitivity of the device (Figure 6.2).

6.2 Results and discussion

Due to the device structure each junction acts as a capacitor because of the total surface coverage of the insulating dielectric film of 50 nm hafnium dioxide (HfO_2) and four bilayers of poly(diallyldimethylammonium) chloride-polysodium 4-styrenesulfonate (PDDA-PSS). During fabrication, the NC monolayers are dip-coated on top of HfO_2 film. Layer-by-layer assembly is one of the most employed and convenient methods to form a uniform, crack-free and large-area thin film for various electronic and photonic devices at low fabrication cost [80, 81]. Four bilayers of PDDA-PSS are needed to supply a uniform film for high surface coverage before coating the NC monolayer on top of these bilayers [82].

To fabricate flexible devices, we use a 35 μm thick polyimide (Kapton) substrate. As shown in Figure 6.1 (b), the flexible tandem PNS configuration is Kapton/indium tin oxide (ITO)/ HfO_2/ PDDA-PSS/ CdHgTe NCs/ Al/ HfO_2/ PDDA-PSS/ CdTe NCs/ Al. The monolayers of UV-vis light-sensitive CdTe NCs and UV-vis-NIR light-sensitive CdHgTe NCs are sandwiched between transparent polyelectrolyte polymers and semi-transparent Al electrodes. Absorption spectra of the photoactive layer consisting of a monolayer of CdTe NCs and CdHgTe NCs show that their absorption onsets are located below 650 and 850 nm, respectively

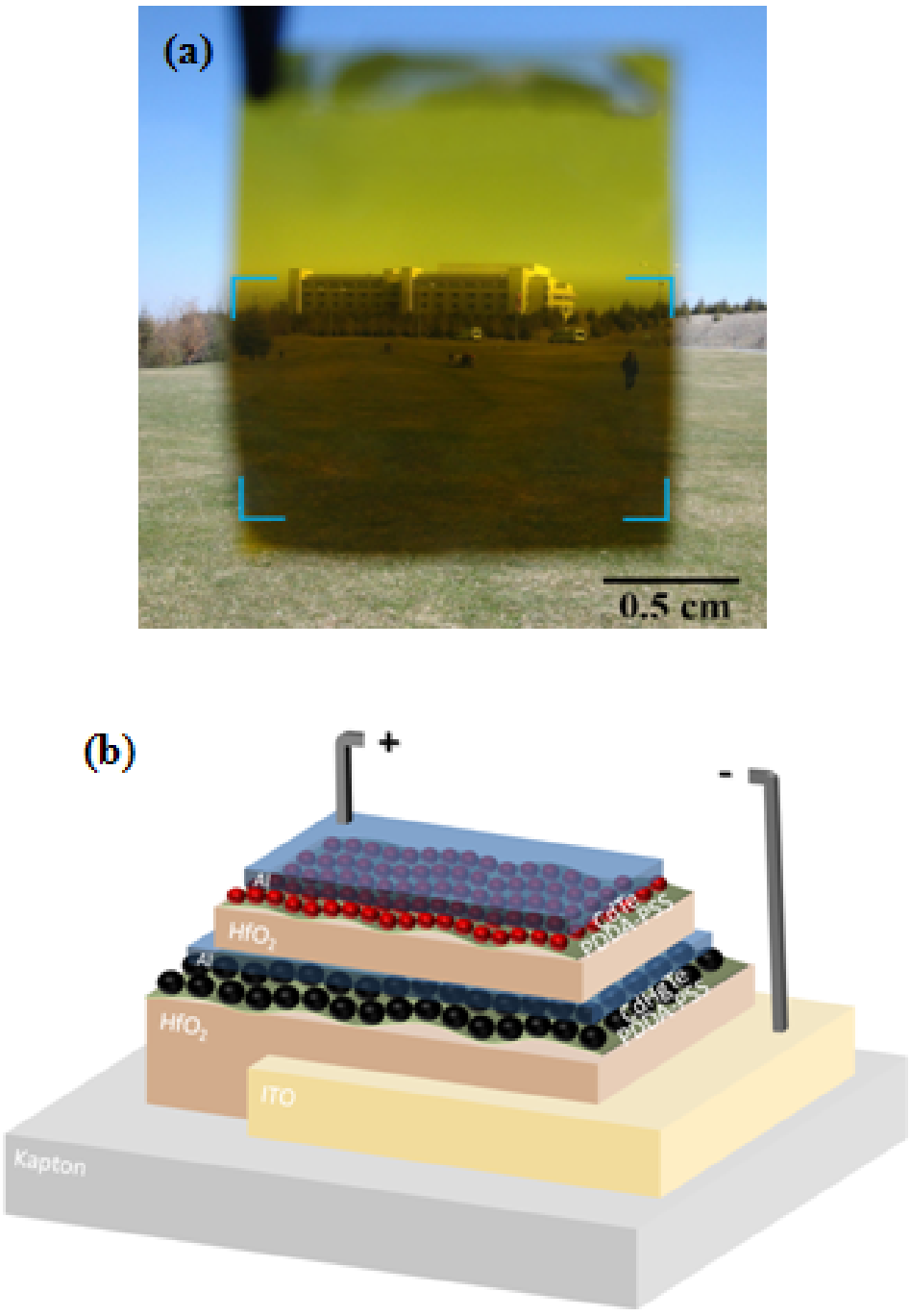

Figure 6.1: (a) Photograph of a semi-transparent large-area tandem photosensitive nanocrystal skin fabricated on a flexible tape. The brackets indicate the device active area, which is 1.5 cm by 1.1 cm. (b) Device schematic of the tandem photosensitive nanocrystal skin.

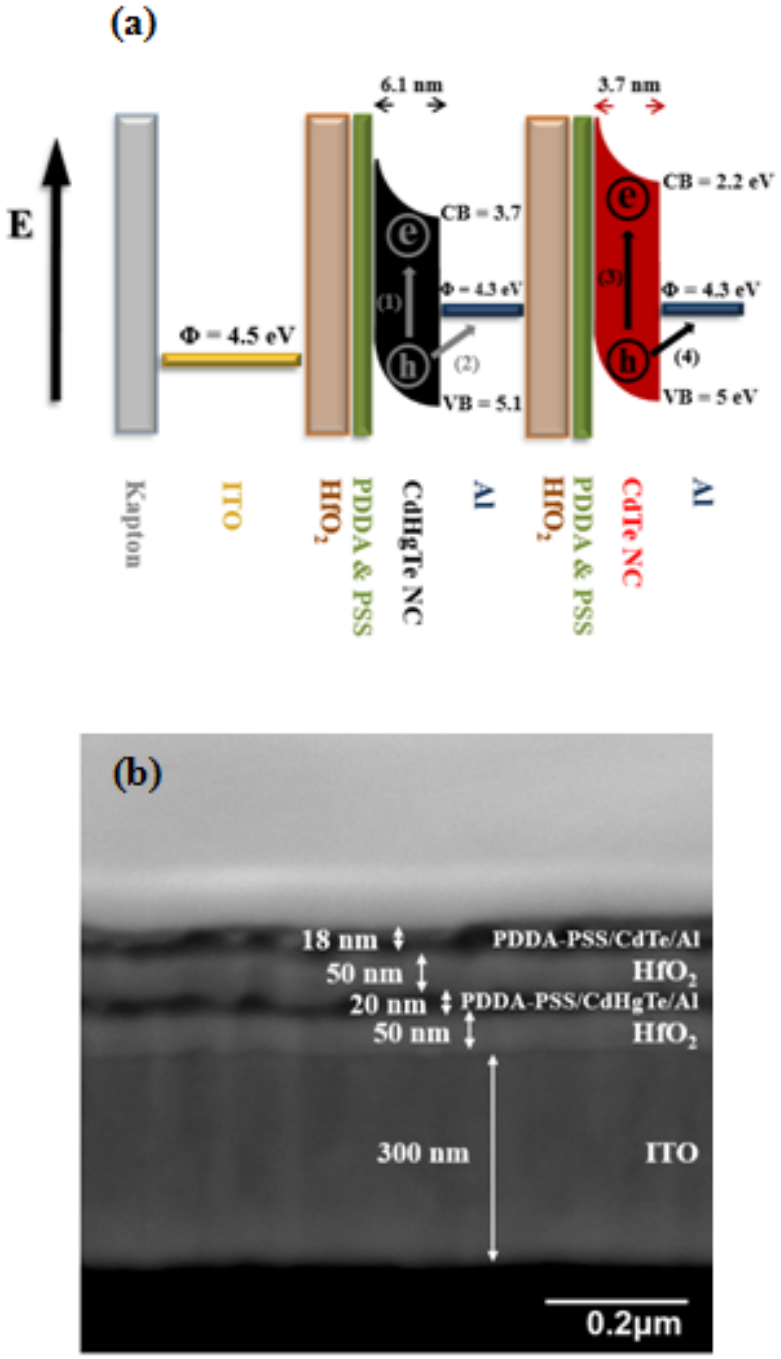

Figure 6.2: (a) Energy level diagram showing the NCs conduction band (CB), valence band (VB), and the workfunction (Φ) of ITO and Al. After the excitons are photogenerated in each junction [(1) and (3)], the electrons are trapped inside the NCs while the holes migrate to the Al side [(2) and (4)]. (b) Cross-section scanning electron microscopy image of the tandem photosensitive nanocrystal skin on top of the Kapton substrate.

(Figure 6.3 (a)). Due to the absorption of the Kapton substrate, all devices are illuminated from the top side (Figure 6.3 (b)). Subsequently, because of their higher absorption coefficient, CdHgTe NCs are preferred for the bottom junction due to the effect of fraction of light absorbed by each of these NC layers. It is expected to accumulate larger photovoltage buildup when light is firstly incident on the CdTe NC layer, which has higher quantum efficency at the range between 350 and 475 nm.

In addition, these as-synthesized NCs are capped with ligands to impart them with colloidal stability [83]. However, these ligands are insulating so they prevent charge transport through the NCs at the same time [84]. In literature, it has been already shown that NCs partially exempted from ligands can be assembled to form a uniform, crack free, and close packed NC thin film [79]. To bring the NCs into close proximity, we partially remove the ligands by adding isopropanol to the solution. Removal of the MPA-capped and TGA-capped ligands from the CdHgTe NCs and CdTe NCs, respectively, is monitored through Fourier transform infrared (FT-IR) spectroscopy and time-resolved fluorescence (TRF) spectroscopy. The FT-IR study shows no appreciable vibration on the carbon-sulphur (C-S) bond, indicating partial removal of ligands (Figure 6.4). Furthermore, the removal of ligands is observed with TRF measurements of the NC solution at the emission peak of 635 nm for CdTe NCs and 795 nm for CdHgTe NCs. As observed, there is a clear TRF decay rate difference between samples with and without ligands, which supports the partial removal of ligands from the NCs and the emergence of potentially nonradiative decay channels as a result of trapped states in the ligand-removed NCs. The NC solution is carefully stirred with the purpose of preventing the precipitation during the layer-by-layer assembly.

To ensure the transmission of incident light, for both electrodes on top of the NCs we deposite only 8 nm thick Al via thermal evaporation in vacuum. The tandem PNS shows 10% optical transparency in the wavelength range of 350-800 nm (Figure 6.3 (c)). Moreover, an 8 nm thick Al layer is evaporated immediately onto the NCs monolayers serving both as the electrode layer and as a protective film to avoid oxidation of the NCs. Because of the energy band alignment between

the NCs and Al, the NCs photoactive layer placed underneath the electrode helps to avoid the need for any external bias to dissociate the photogenerated excitons [85]. Hence, the absence of any energetic barrier between the NCs and Al electrode allows the photogenerated holes to immediately migrate to Al, resulting in higher photosensitivity. Moreover, the independence of the device on the external bias boosts the stability of the device, since the NC film degradation decreases significantly [86]. A schematic band diagram of the tandem PNS is shown in Figure 6.2 (a).

ITO coated atop a Kapton substrate is chosen as the bottom electrode. A 300 nm thick ITO film is deposited on Kapton by means of radio frequency (RF)-sputtering. Afterward, it is annealed by a rapid thermal treatment in vacuum at 200 °C for 20 min in order to decrease the sheet resistivity of ITO. Then the substrate is exposed to oxygen plasma to create additional hydroxyl groups necessary for the atomic layer deposition (ALD) of the high dielectric constant HfO_2 layer [84]. The great challenge in fabricating the tandem PNS is to deposit a thin enough dielectric spacer layer on top of the large-area ITO in order to block any charges migrating from the NCs to ITO. Thus, we deposit 50 nm HfO_2 via ALD at 200 °C. ALD preferentially coats hydrophilic surfaces owing to the usage of pulses of water, which improves the quality of the self-assembled film [87]. Moreover, the encapsulation with HfO_2 averts cracking of the plastic substrate in the further fabrication steps. Following that, oppositely charged PDDA and PSS bilayers are coated via a fully computerized dip-coater system. Then, dipping the sample into the dispersion of the CdHgTe NCs is applied. The coated substrate is then washed with dionized water to remove unbound NCs [88, 89]. Finally, immediately after coating the NC monolayer film, the Al contact (8 nm) is deposited via thermal evaporation. The second constituent junction is fabricated similarly on top of the first one but at a different operating temperature of the ALD. We deposit 50 nm HfO_2 at low temperatures of 80 °C to prevent any damage to the NCs. The cross-section scanning electron microscopy (SEM JEOL JIB-4501) images of the tandem PNS on the Kapton substrate are shown in Figure 6.2 (b), and Figure 6.5 demonstrates its well-defined structure.

For the device fabrication, we synthesize water-soluble thioglycolic acid

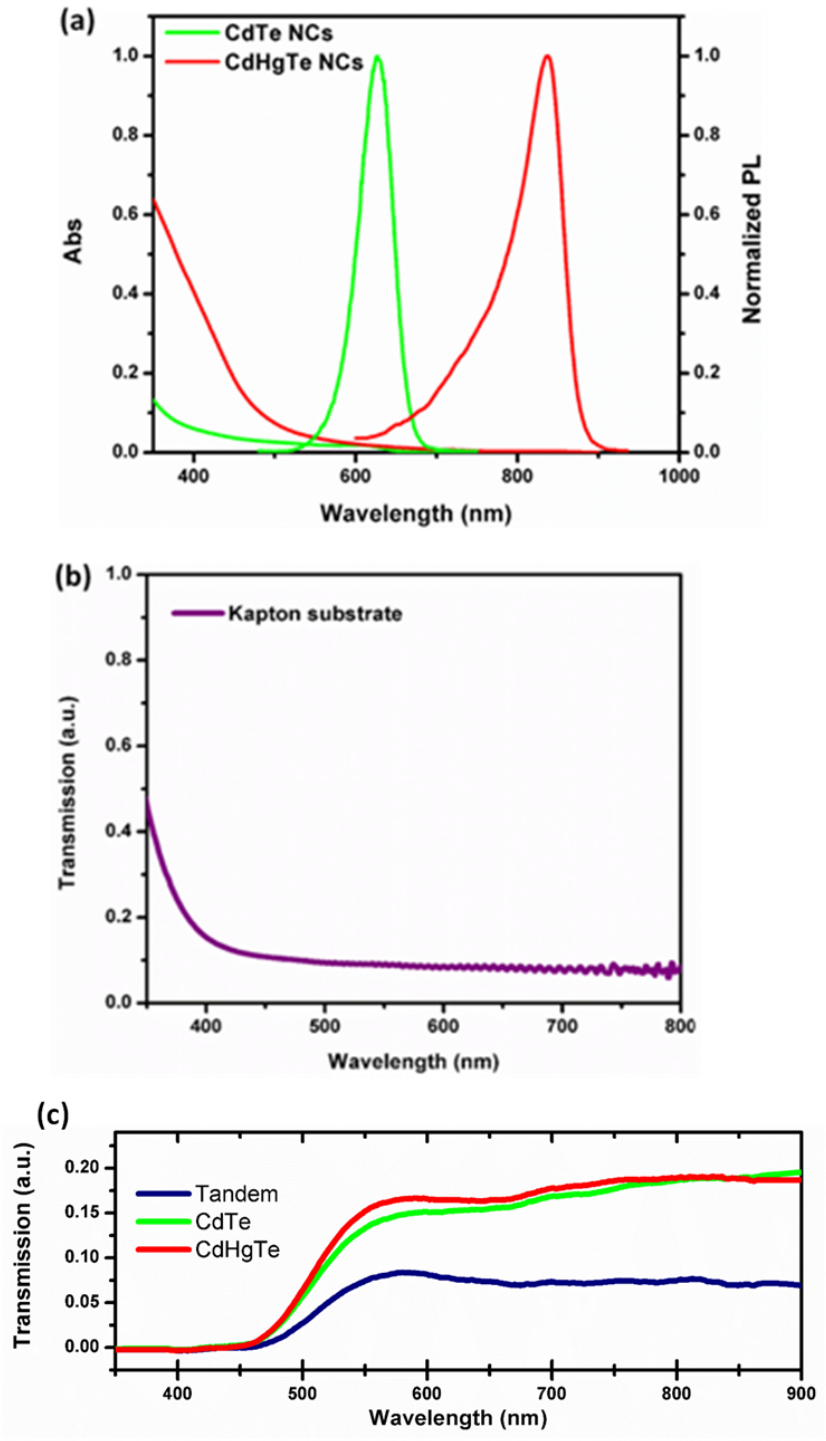

Figure 6.3: (a) Absorption and photoluminescence spectra of a monolayer of CdTe NCs and CdHgTe NCs on glass. (b) Absorption spectra of Kapton (35-μm thick polyimide) substrate. (c) Transmission spectra of the semi-transparent CdTe NCs based PNS, the CdHgTe NCs based PNS, and the tandem PNS atop a Kapton substrate.

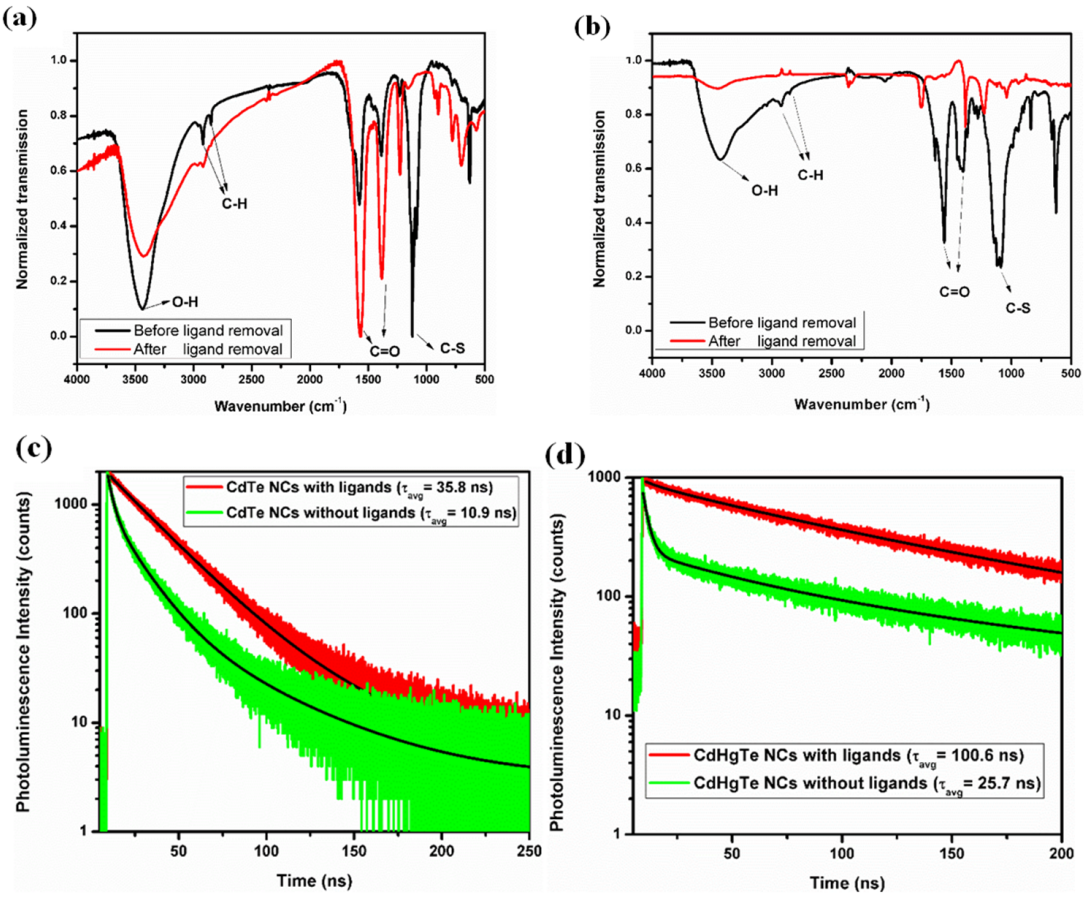

Figure 6.4: Normalized FT-IR spectra of (a) CdTe NC-capped TGA ligands and (b) CdHgTe NC-capped MPA ligands. TRF measurement of (c) CdTe NC and (d) CdHgTe NC solution before and after the ligand removal.

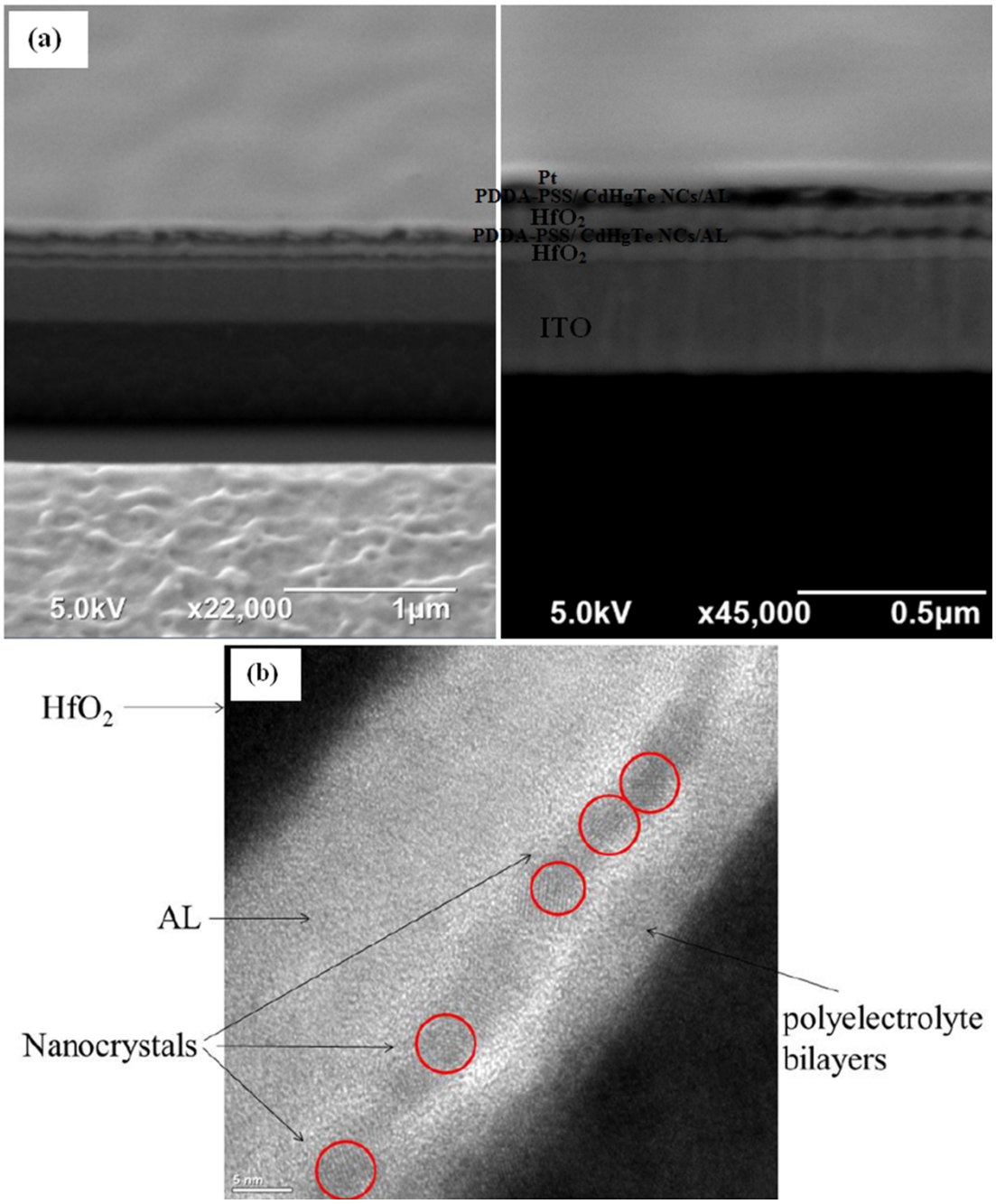

Figure 6.5: (a) and (b) Cross-sectional scanning electron microscopy images of the tandem PNS on the Kapton substrate. Ion milling is performed with a protective platinum (Pt) layer.

(TGA)-capped CdTe NCs and 3-mercaptopropionic acid (MPA)-capped CdHgTe NCs [31, 32, 33]. The aqueous CdTe NCs are synthesized following a previously reported procedure [31] using a synthetic setup given elsewhere [33].

In order to provide a sufficiently uniform film with high surface coverage for coating the NC monolayer we use four bilayers of PDDA-PSS. We remove the ligands partially by adding isopropanol to the NCs solutions and centrifuging the mixtures for three times. A fully automated dip-coater system is used with the purpose of film deposition with layer-by-layer assembly. The PDDA-PSS film is assembled by sequentially dipping the substrate into the prepared solution for 5 min and rinsed with dionized water for 1 min. After coating one extra layer of positively charged PDDA on top of subsequent bilayers, negatively charged water soluble NCs are coated by immersing the substrate.

In operation, after the generation of electron-hole pairs without applying any external bias, charges are dissociated at the NC monolayer and electrode interfaces. Subsequently, owing to proper work functions of Al and the NCs, the holes move to the Al electrode and lead to a voltage buildup. However, the electrons are trapped inside the NCs due to the presence of HfO_2 and four bilayers of PDDA-PSS as a dielectric film. Under light illumination, a net potential buildup is observed. This voltage buildup diminishes over time after charging upto the peak point, as shown in Figure 6.6.

We observe that capacitive charges across the Al electrodes continuously decay with the instantaneous resistor-capacitor (RC) decay of the whole circuitry (the device plus the external shunt resistor). After turning off the light at the peak point, the potential decreases and even goes to negative values until it returns back to the initial point. The reason behind is the time taken for sweeping the trapped charges outside the NCs. These trapped electrons inside the NCs are observed to be residing in trap states for quite long times. These states are considered as deep trap states, as reported by Bulovic et al. [90]. A higher voltage buildup results in a further negative voltage value. This relation is in good agreement with the kinetic components of the device as it is mentioned above.

The proposed platform demonstrates a higher level of sensitivity if we manage to increase the number of photogenerated electron-hole pairs. Therefore, we propose an extra NC monolayer to be integrated inside the device in order to increase the photogenerated potential buildup. Since we do not apply any external bias during the device operation, we need only one monolayer of NCs exactly below the Al electrode. Consequently, we have added an extra NC-based junction to significantly enhance the sensitivity of the device. Figure 6.6 (c) shows the photoresponse spectra of the tandem structure, under the light radiating from the top side.

A large photovoltage buildup is detected only in the case when the light is incident from the top, since the photovoltage buildup and, consequently, the photosensitivity of the bottom side (ITO side) is near or equal to zero due to the color filter (cut-off at 400 nm) property of the Kapton substrate. In response to the excitation wavelength and illumination intensity we observe a larger potential buildup at shorter wavelengths. Similarly, because of the increased optical absorption at shorter excitation wavelengths, which increases the amount of trapped electrons inside the NCs, we observe a higher negative voltage after switching off the light. Owing to the increased charging of the NCs with the trapped electrons at shorter excitation wavelengths, more time is required to recover after switching off light.

Photovoltage buildup characteristics of the photosensitive nanocrystal skins are measured using Agilent B1500A parameter analyzer under Xenon light source integrated with a monochromator. The light intensity is recorded using an optical power meter. In order to prevent the mixing of the second harmonic coming from Xenon light, at wavelengths longer than 600 nm, a color glass filter with a cut-off of 400 nm is used. In operation, the devices are connected to a shunt resistor of 200 MΩ without any external bias is. Due to the RC decay of the devices, we adjust all shunt resistance in a manner in which all RC kinetics of the devices are identical. The surface sheet resistance of ITO coated Kapton is measured using the four-point probe method to be 40 Ω/sq. The active area is 1.5 cm by 1.1 cm, which is defined by the overlap between the bottom electrode on the Kapton substrate and the top electrode on NCs.

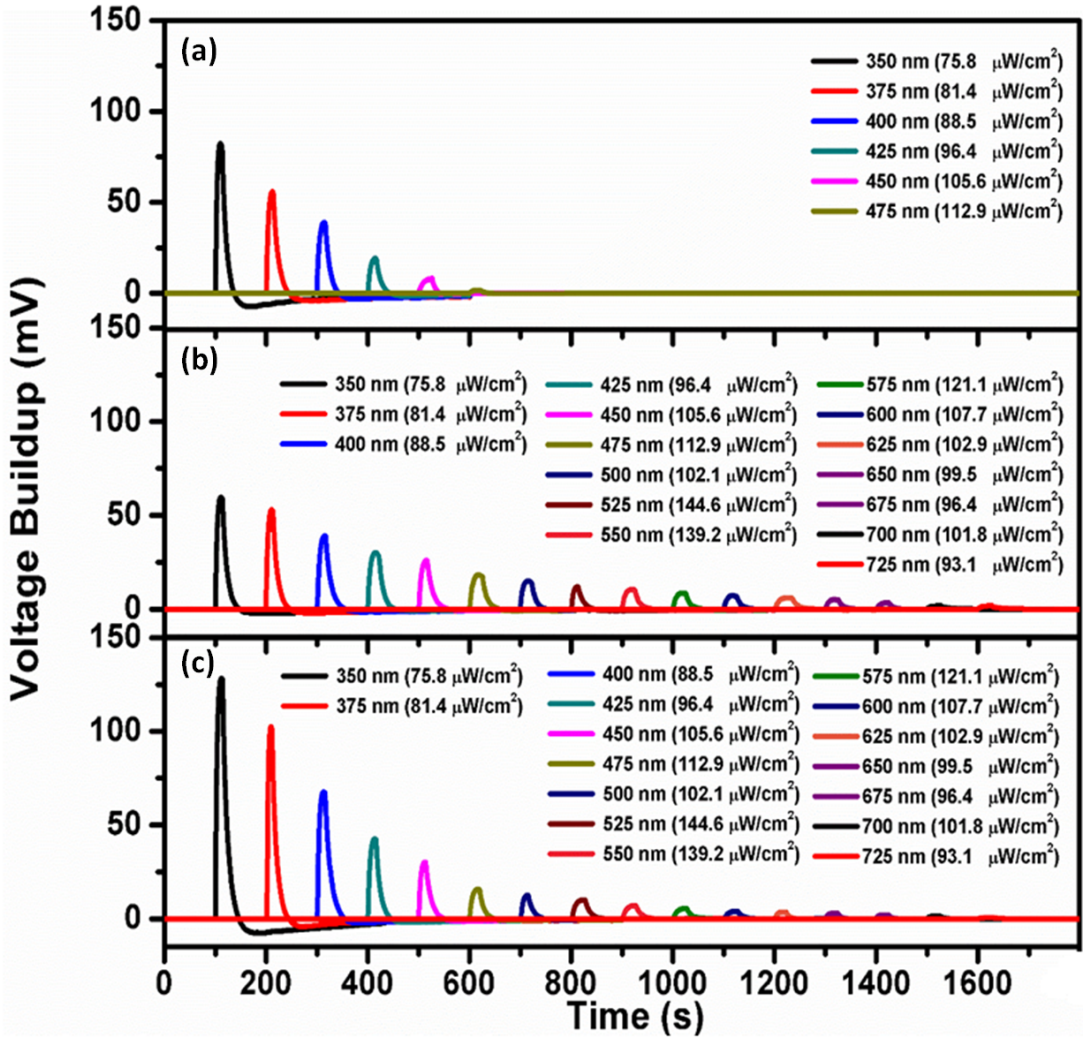

Figure 6.6: Photovoltage buildup at different excitation wavelengths and optical intensity for (a) CdTe NCs based PNS, (b) CdHgTe NCs based PNS, and (c) tandem CdTe-CdHgTe NCs based PNS. CdTe NCs based PNS exhibits no performance after 475 nm wavelength owing to the low absorption of CdTe NCs at longer wavelengths.

We also constructed control devices to elucidate the benefits of the tandem PNS. The performance of the best control devices is depicted in Figure 6.6 (a) and Figure 6.6 (b). By testing the control samples, we measured their performance upon illumination from the top side, similar to the tandem PNS. To compare the tandem and single junction PNS, all measurements were taken under the same conditions. If the fraction of incident photons absorbed by layers between the NCs layers is negligible and the fraction of incident photons absorbed in the active layer is small, then the ideal tandem PNS should reveal a photovoltage buildup equal to the sum of the photogenerated potential buildup of the constituent junctions. The tandem PNS device indicates a total photovoltage buildup at each wavelength, almost equal to the sum of the photovoltage buildup of the individual single junctions. We attribute the observed small difference to the mismatch between the interface layers in the tandem PNS and the fraction of incident photons absorbed by active layer and layers between the NCs layers. To confirm the reproducibility of the results obtained, more than 20 samples were prepared and tested, with the best device demonstrating photovoltage buildup of 128.4 mV for an excitation intensity of 75.8 μW/cm^2 at 350 nm. While conducting our work, we fabricated more than 11 devices with photovoltage buildup larger than 120 mV at impinging optical intensity of 75.8 μW/cm^2 at 350 nm.

To figure out the sensitivity of the photosensitive PNS, a meaningful figure-of-merit is defined by the ratio of the photovoltage buildup across the device and the incident optical power incident on the device. Figure 6.7 shows the corresponding sensitivity as a function of the excitation wavelength. It should be noted that the detection sensitivity remains low in the long wavelength region where the NCs exhibit poor optical absorption. This is because there are fewer electron and hole states available inside a NC at lower photon energies. This behavior indicates the wavelength dependence of the tandem PNS and is strongly dependent on the absorption spectra of NCs (Figure 6.3 (a)). Moreover, the internal quantum efficiency is measured at room temperature with no external bias across the device and the samples were illuminated under Xenon light source integrated with a monochromator (Figure 6.8).

The benefit of introducing a flexible tandem PNS is twofold. It is expected

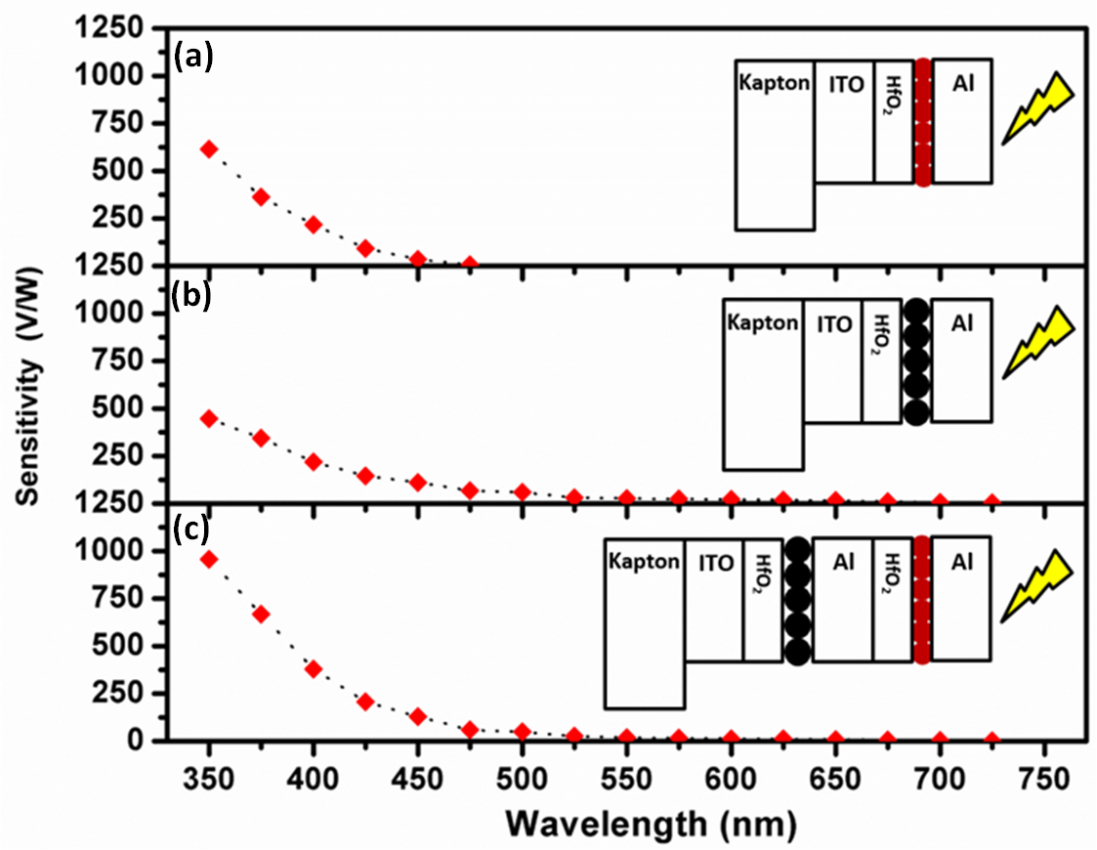

Figure 6.7: Corresponding sensitivities as a function of the excitation wavelength for (a) CdTe NCs based PNS, (b) CdHgTe NCs based PNS, and (c) tandem CdTe-CdHgTe NCs based PNS. A representative schematics is shown in the inset.

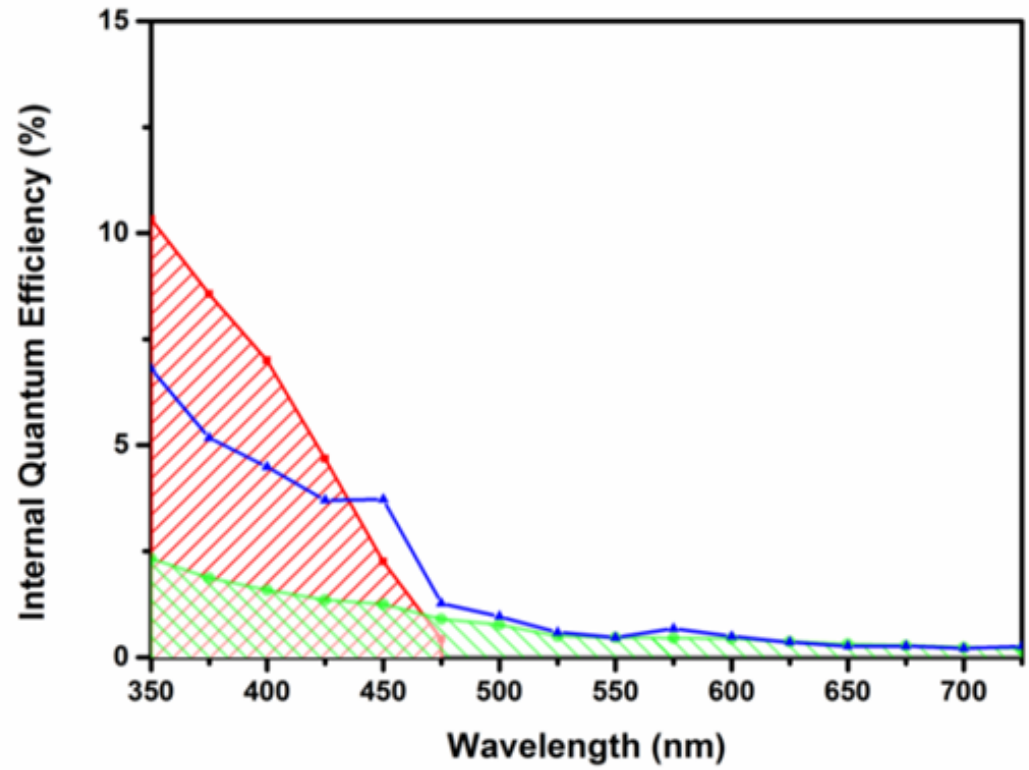

Figure 6.8: Internal quantum efficiency (IQE) spectra of the CdTe NCs based PNS (red), CdHgTe NCs based PNS (green) and tandem CdTe CdHgTe NCs based PNS (blue) as a function of the optical wavelength where no external bias is applied. Figure shows the agreement between the IQE spectrum, the absorbance spectrum of NCs and the top semi-transparent contact, suggesting that the entirety of photoresponse is from excitation of the NCs and subsequent exciton dissociation when the light is incident from the top.

to observe a sensitivity enhancement when we adapt the two separated junctions incorporated into one structure. Furthermore, in contrary to the conventional multi-junction devices for which the current-matching between the junctions is essential, there is no such limitation in tandem PNS devices. The photogenerated holes from an adjacent monolayer are accumulated at the top electrode, contributing their potential buildup to the overall device response. The tandem PNS exhibits comparably high photosensitivity with respectly to typical NC based photodetectors. We measure the minimum noise equivalent intensity to be 0.34 μW/cm^2, which is comparable to the solution-cast NC photodetectors reported previously [91], [92]. Furthermore, in the case of tandem PNS, by decreasing the shunt resistance from 200 MΩ to 200 KΩ, it is possible to speed up the response time from 10.1 s to 100 ms) for an excitation intensity level of 75.8 μW/cm^2. The 3-dB bandwidth increases from 4 Hz to 6 Hz and 10 Hz when the shunt resistance is decreased from 1 MΩ to 500 KΩ and 200 KΩ, respectively. As it can be seen from Figure 6.9 (a), increasing shunt resistance would in fact enhance the voltage buildup. This result indicates a trade-off between the sensitivity and the 3-dB bandwidth. Depending on the requirements of the application, the operation bandwidth should be specifically handled. In order to provide further optoelectronic characterization of the tandem PNS, we measure their linearity from the photovoltage buildup versus incident optical power. Figure 6.9 (b) shows good linearity of the tandem PNS at different illumination intensity.

In addition, the tandem PNS constructed on a Kapton substrate can be cut with scissors without any damage or without any loss in the total sensitivity. Figure 6.10 (a)) shows the tandem PNS and its cutting with scissors into desired geometries of arbitrary shapes. The optical performance of the chopped parts are lower than those of the initial structure as expected from the dependence of the photovoltage buildup on the size of active area. However, by combining the photovoltage buildup of fragments, similar values to the initial structure are obtained as demonstrated in Figure 6.10 (b). As a consequence, a large-area device can be fabricated and then cut into desired smaller pieces of any shape, as long as the bottom and top contacts are intact for the electrical connections.

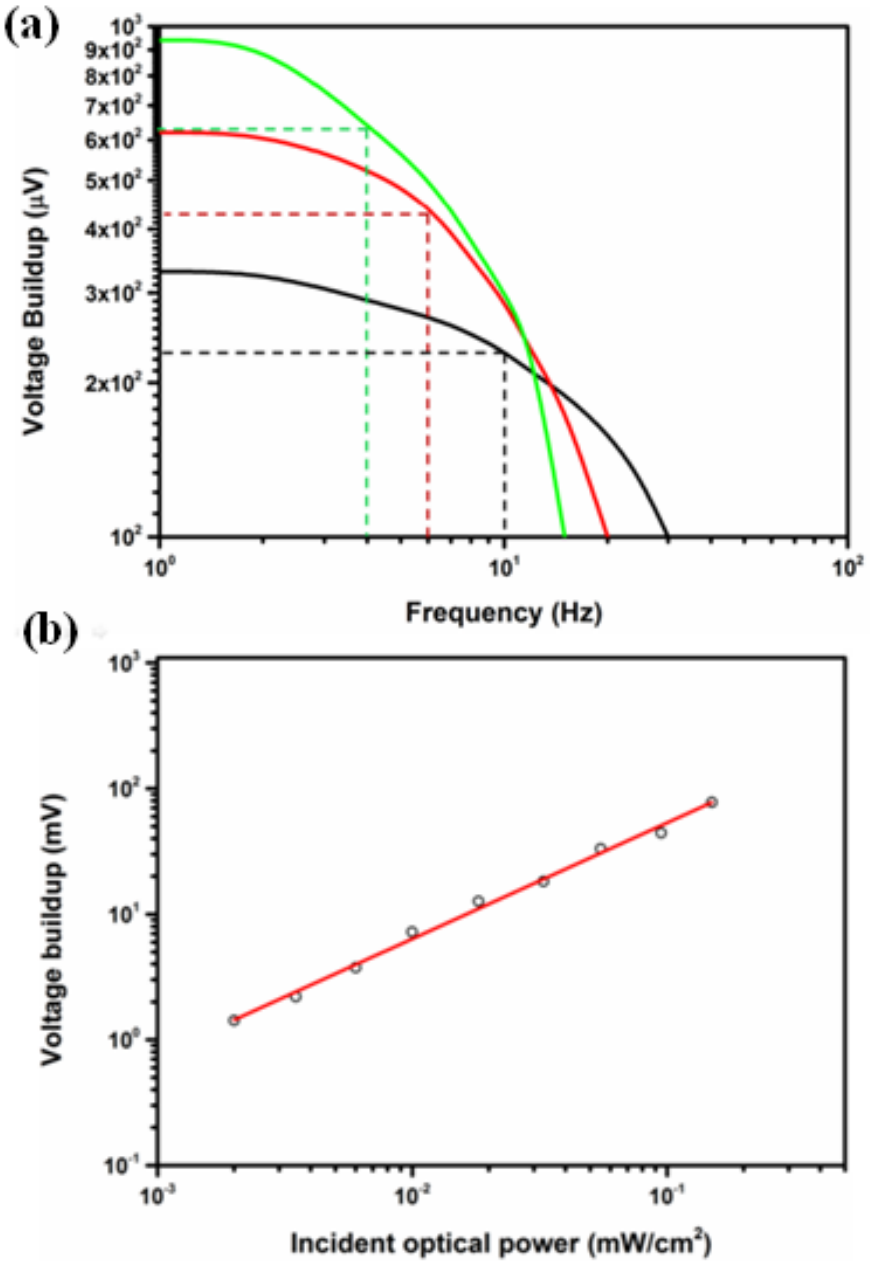

Figure 6.9: (a) Modulation frequency response of the tandem PNS using different shunt resistances at impinging optical intensity of 75.8 μW/cm^2 at 350 nm. The 3-dB bandwidth decreases from 10 Hz (black) to 6 Hz (red) and 4 Hz (green) when the shunt resistance is increased from 200 KΩ to 500 KΩ and, 1 MΩ respectively. (b) Photovoltage buildup as a function of the incident power at 425 nm.

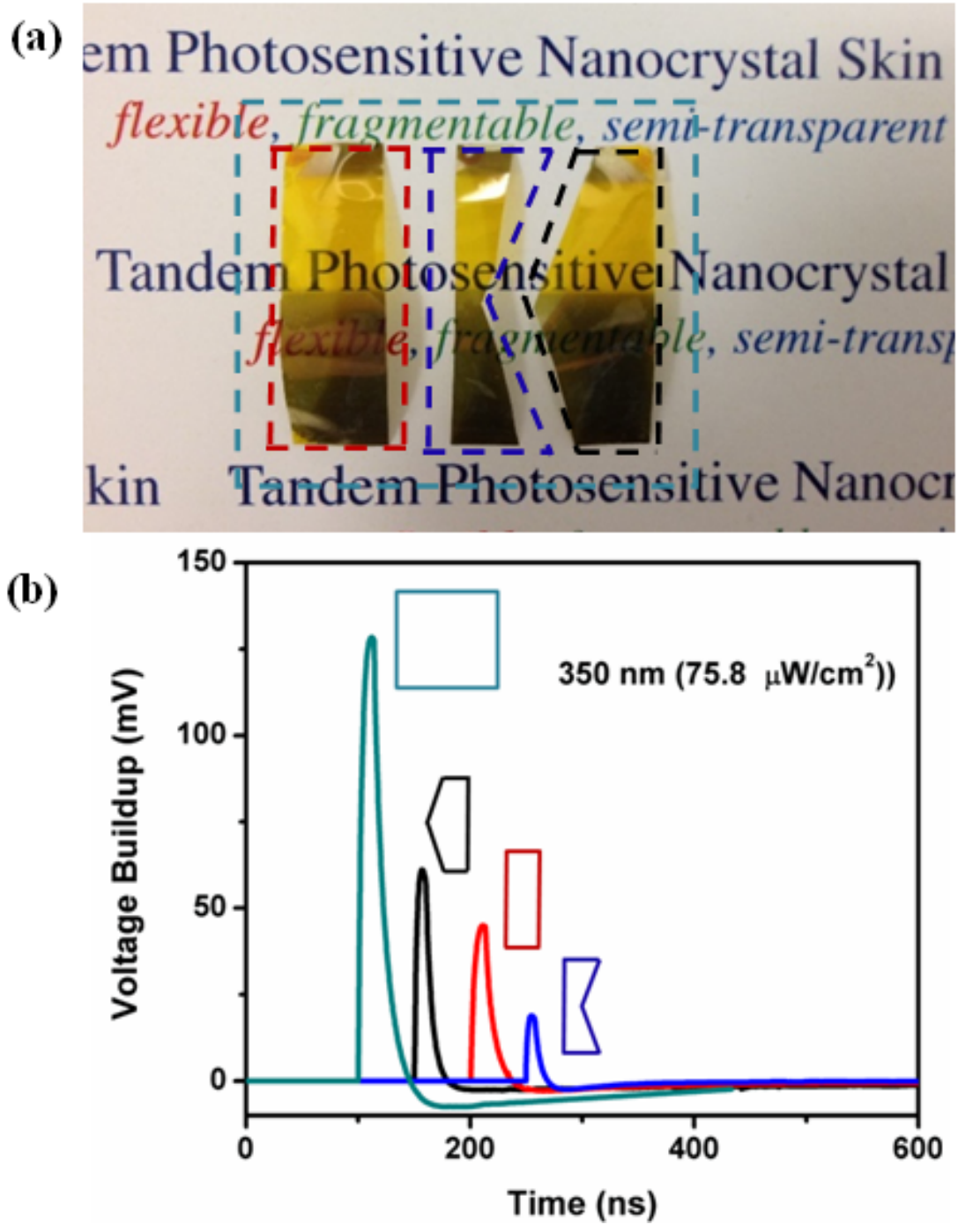

Figure 6.10: (a) Tandem PNS based on Kapton substrate cut with scissor. The device can be designed to be cut into desired smaller pieces of any shape. (b) The addition of the photovoltage buildups from the cut parts yields a similar level as in the initial structure for 75.8 μW/cm^2 at 350 nm.

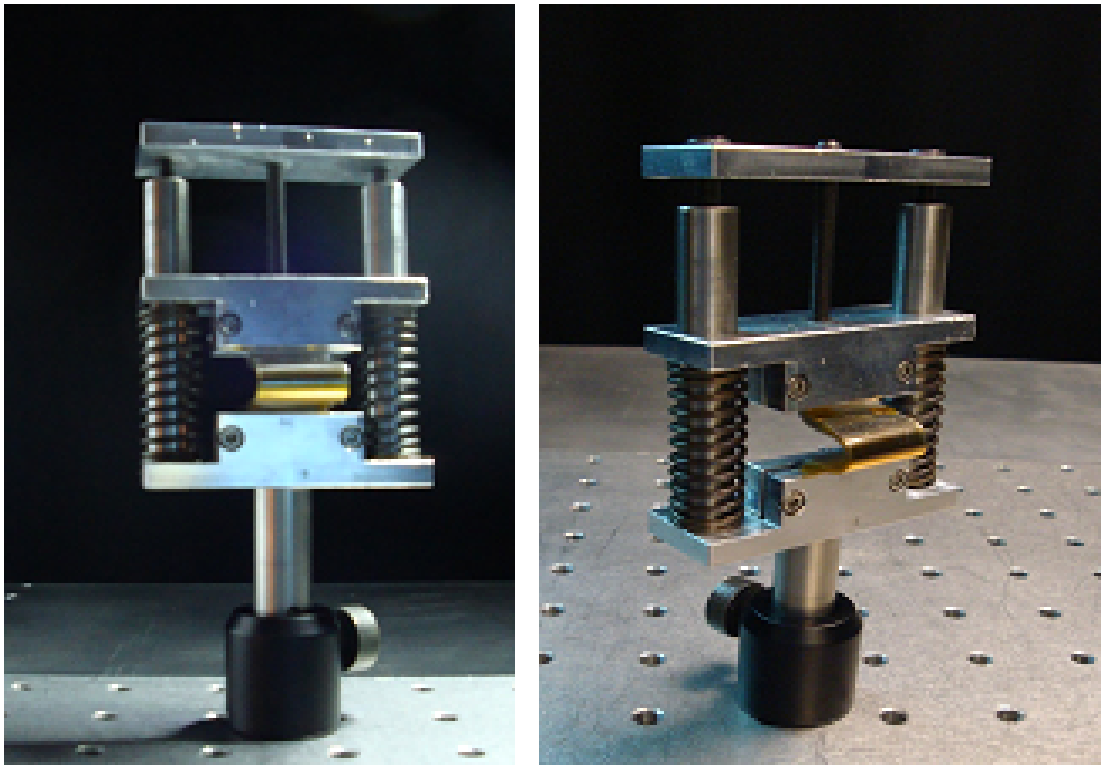

Figure 6.11: Mechanical bending test conducted on the tandem PNS.

The radius of curvature of a bent tandem PNS is defined as the maximum bending curvature that the device can tolerate. In the bending test, the sample is flexed with a designated critical radius of curvature (R_c) during its simultaneous characterization (Figure 6.11). The corresponding R_c value is measured to be 3.5 mm (Figure 6.12 (a)). With further decreasing the radius of curvature, the photovoltage buildup suddenly decreases due to crack formation, especially in the ITO coating. In other words, by a progressive decrease in the Rc, the electrical resistance of the ITO-coated Kapton exhibits a sudden increase. Subsequently, these devices cannot be operated anymore. Furthermore, the device is subjected to subsequent flexing cycles at 7.5 mm radius. The resulting characteristics show excellent device performance indicating that flexible tandem PNS is robust under mechanical deformations, which is highly desirable for applications that require flexibility (Figure 6.12 (b)).

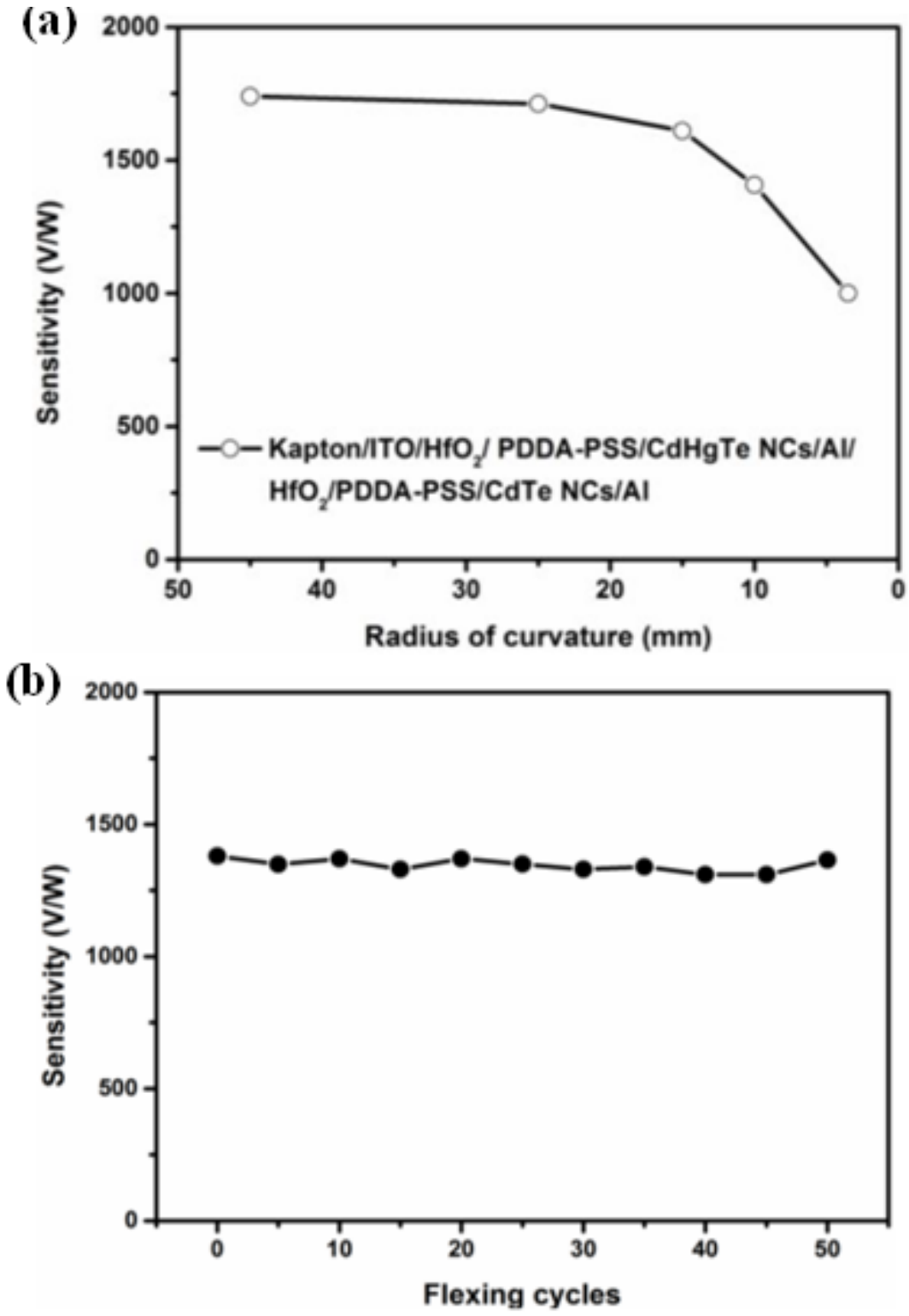

Figure 6.12: Flexible PNS can be bent around a 3.5 mm radius of curvature with device performance degradation to the half of the unbent configuration. (b) Performance characteristics of the device (sensitivity and photovoltage buildup).

6.3 Conclusion

In conclusion, we showed the first highly sensitive tandem PNS through the incorporation of monolayers of CdTe and CdHgTe NCs on a platform, which is also flexible, cuttable and semi-transparent. By taking advantage of an additional NC-based junction, an enhancement in the sensitivity and an extension in the operational wavelength range were observed. The present tandem PNS is fabricated over large areas on flexible plastics and can be used to build photosensitive devices with two or more junctions. Such multi-junction devices enable a route to enhance the sensitivity of PNS. These results carry potential for transparent thin film based colloidal optoelectronic devices including photosensors for applications in smart phones, smart windows and facades.

Chapter 7

Conclusion

In this thesis, we propose and demonstrate hybrid nanostructures consisting of combination of nanowires, nanodiscs, and nanocrystals with their in-solution and in-template syntheses to achieve optoelectronic devices for highly polarized light generation, spectrum shaping and enhanced photosensing. While we present promising fabrication methods for these structures, we show that our metal/semiconductor assemblies together with their strong electrical and optical properties offer great potential in photonics and optoelectronics.

Using in-template electrodepostion, we synthesized segmented nanowires (Au-Ni-Au and/or Au-Ag-Au) in porous membranes with segment or gap lengths from 20 nanometers up to 20 micrometers by controlling the amount of deposition into these membranes. We demonstrate arrays of suspended and in-solution dispersible plasmonic gold nanodiscs via the method of on-wire lithography. Thanks to this method, nanodiscs are securely kept inside the transparent dielectric wrap of nitride film, while the sacrificial nickel segments are selectively etched determining the gap-width between the discs.

We also showed a proof-of-concept hybrid thin nanocrystal film device for the generation of polarized light with a contrast of perpendicular to parallel polarizations larger than 15:1 in the visible range by employing multi-segmented

nanowires having ferromagnetic parts, which are well aligned under external magnetic field. This is a record high polarization contrast ratio for isotropic nanocrystal emitters. The proposed wire grid structure makes use of a much easier fabrication procedure compared to the conventional expensive fabrication techniques. Furthermore, the planar structure of the hybrid thin film allows for more functional geometry compared to three dimensional birefringent crystal based polarizers in terms of compatibility into planar integrated circuits. Our experimental results of highly polarized light generation are also verified by FDTD simulations, which revealed the relation between inter-nanowire distance and the achieved polarization contrast, enabling the possible optimization on the transmission level.

We studied the light interaction of our fabricated gold nanodisc arrays. Our experimental and FDTD simulation results reveal disc-/gap-width size effect on polarized light scattering with their localized electrical field enhancements. We observe that the scattered light intensity is highly dependent on the position of the discs such that the polarization can be enhanced or suppressed depending on whether it is parallel or normal to the discs. Moreover, the sensitivity measurements by the light-sensitive nanocrystal skins integrated with gold nanodiscs verify enhanced voltage buildup performance.

Finally, we showed highly sensitive, flexible tandem photosensitive platforms through the incorporation of monolayers of CdTe and CdHgTe nanocrystals on a platform. The presented tandem photosensitive nanoskin is fabricated over large areas on flexible plastics and can be used to build photosensitive devices with two or more junctions. Such multi-junction devices provide an important enhancement in the sensitivity and an extension in the operational wavelength range. These devices hold great potential for transparent thin film based colloidal optoelectronic devices including photosensors for applications in smart displays and facades.

During this thesis, we published a top-tier peer-reviewed science citation index (SCI) journal paper of the presented work in Chapter 4 [58]. We presented the results of Chapter 3 and Chapter 5 in an international refereed top conference of

IEEE [49]. Also, the demonstrated work in Chapter 6 is in submission process [30]. This thesis work further resulted in an international patent application.

Bibliography

[1] Z. Yu, G. Veronis, S. Fan, and M. L. Brongersma, "Design of midinfrared photodetectors enhanced by surface plasmons on grating structures," *Applied Physics Letters*, vol. 89, no. 15, p. 151116, 2006.

[2] K. Nakayama, K. Tanabe, and H. A. Atwater, "Plasmonic nanoparticle enhanced light absorption in GaAs solar cells," *Applied Physics Letters*, vol. 93, no. 12, p. 121904, 2008.

[3] C. Liu, M. Hong, H. Cheung, F. Zhang, Z. Huang, L. Tan, and T. Hor, "Bimetallic structure fabricated by laser interference lithography for tuning surface plasmon resonance," *Optics Express*, vol. 16, no. 14, pp. 10701–10709, 2008.

[4] B. Zhang, Y. Zhao, Q. Hao, B. Kiraly, I.-C. Khoo, S. Chen, and T. J. Huang, "Polarization-independent dual-band infrared perfect absorber based on a metal-dielectric-metal elliptical nanodisk array," *Optics Express*, vol. 19, no. 16, pp. 15221–15228, 2011.

[5] J. Rosenberg, R. V. Shenoi, T. E. Vandervelde, S. Krishna, and O. Painter, "A multispectral and polarization-selective surface-plasmon resonant midinfrared detector," *Applied Physics Letters*, vol. 95, no. 16, p. 161101, 2009.

[6] L. Qin, S. Park, L. Huang, and C. A. Mirkin, "On-wire lithography," *Science*, vol. 309, no. 5731, pp. 113–115, 2005.

[7] S. Liu, J. B.-H. Tok, and Z. Bao, "Nanowire lithography: Fabricating controllable electrode gaps using Au-Ag-Au nanowires," *Nano Letters*, vol. 5, no. 6, pp. 1071–1076, 2005.

[8] L. Qin, M. J. Banholzer, J. E. Millstone, and C. A. Mirkin, "Nanodisk codes," *Nano Letters*, vol. 7, no. 12, pp. 3849–3853, 2007.

[9] R. Wilson, A. R. Cossins, and D. G. Spiller, "Encoded microcarriers for high-throughput multiplexed detection," *Angewandte Chemie International Edition*, vol. 45, no. 37, pp. 6104–6117, 2006.

[10] Y. C. Cao, R. Jin, and C. A. Mirkin, "Nanoparticles with Raman spectroscopic fingerprints for DNA and RNA detection," *Science*, vol. 297, no. 5586, pp. 1536–1540, 2002.

[11] F. Tam, G. P. Goodrich, B. R. Johnson, and N. J. Halas, "Plasmonic enhancement of molecular fluorescence," *Nano Letters*, vol. 7, no. 2, pp. 496–501, 2007.

[12] C. Langhammer, B. Kasemo, and I. Zorić, "Absorption and scattering of light by Pt, Pd, Ag, and Au nanodisks: Absolute cross sections and branching ratios," *The Journal of Chemical Physics*, vol. 126, no. 19, p. 194702, 2007.

[13] C. Rockstuhl and F. Lederer, "Photon management by metallic nanodiscs in thin film solar cells," *Applied Physics Letters*, vol. 94, no. 21, p. 213102, 2009.

[14] S.-S. Lin, K. M. Yemelyanov, E. N. Pugh Jr, N. Engheta, *et al.*, "Separation and contrast enhancement of overlapping cast shadow components using polarization," *Optics Express*, vol. 14, no. 16, pp. 7099–7108, 2006.

[15] P. Yeh and C. Gu, *Optics of liquid crystal displays*, vol. 67. John Wiley & Sons, 2010.

[16] H. Tamada, T. Doumuki, T. Yamaguchi, and S. Matsumoto, "Al wire-grid polarizer using the s/p polarization resonance effect at the 0.8-μm-wavelength band," *Optics Letters*, vol. 22, no. 6, pp. 419–421, 1997.

[17] T. Ozel, S. Nizamoglu, M. A. Sefunc, O. Samarskaya, I. O. Ozel, E. Mutlugun, V. Lesnyak, N. Gaponik, A. Eychmuller, S. V. Gaponenko, and H. V. Demir, "Anisotropic emission from multilayered plasmon resonator

nanocomposites of isotropic semiconductor quantum dots," *ACS Nano*, vol. 5, no. 2, pp. 1328–1334, 2011.

[18] S.-T. Wu, U. Efron, and L. D. Hess, "Birefringence measurements of liquid crystals," *Applied Optics*, vol. 23, no. 21, pp. 3911–3915, 1984.

[19] A. Szabo, "Theory of polarized fluorescent emission in uniaxial liquid crystals," *The Journal of Chemical Physics*, vol. 72, no. 8, 1980.

[20] L. Zhang, J. H. Teng, S. J. Chua, and E. A. Fitzgerald, "Linearly polarized light emission from InGaN light emitting diode with subwavelength metallic nanograting," *Applied Physics Letters*, vol. 95, no. 26, 2009.

[21] M. Ma, D. S. Meyaard, Q. Shan, J. Cho, E. F. Schubert, G. B. Kim, M.-H. Kim, and C. Sone, "Polarized light emission from GaInN light-emitting diodes embedded with subwavelength aluminum wire-grid polarizers," *Applied Physics Letters*, vol. 101, no. 6, 2012.

[22] H. V. Demir, S. Nizamoglu, T. Erdem, E. Mutlugun, N. Gaponik, and A. Eychmüller, "Quantum dot integrated LEDs using photonic and excitonic color conversion," *Nano Today*, vol. 6, no. 6, pp. 632–647, 2011.

[23] G. Konstantatos, I. Howard, A. Fischer, S. Hoogland, J. Clifford, E. Klem, L. Levina, and E. H. Sargent, "Ultrasensitive solution-cast quantum dot photodetectors," *Nature*, vol. 442, no. 7099, pp. 180–183, 2006.

[24] B. N. Pal, I. Robel, A. Mohite, R. Laocharoensuk, D. J. Werder, and V. I. Klimov, "High-sensitivity p–n junction photodiodes based on PbS nanocrystal quantum dots," *Advanced Functional Materials*, vol. 22, no. 8, pp. 1741–1748, 2012.

[25] F. Prins, M. Buscema, J. S. Seldenthuis, S. Etaki, G. Buchs, M. Barkelid, V. Zwiller, Y. Gao, A. J. Houtepen, L. D. Siebbeles, *et al.*, "Fast and efficient photodetection in nanoscale quantum-dot junctions," *Nano Letters*, vol. 12, no. 11, pp. 5740–5743, 2012.

[26] R. Rossetti, S. Nakahara, and L. Brus, "Quantum size effects in the redox potentials, resonance Raman spectra, and electronic spectra of CdS crystallites in aqueous solution," *The Journal of Chemical Physics*, vol. 79, no. 2, pp. 1086–1088, 1983.

[27] D. V. Talapin, A. L. Rogach, A. Kornowski, M. Haase, and H. Weller, "Highly luminescent monodisperse CdSe and CdSe/ZnS nanocrystals synthesized in a hexadecylamine-trioctylphosphine oxide-trioctylphospine mixture," *Nano Letters*, vol. 1, no. 4, pp. 207–211, 2001.

[28] M. A. Hines and G. D. Scholes, "Colloidal PbS nanocrystals with size-tunable near-infrared emission: observation of post-synthesis self-narrowing of the particle size distribution," *Advanced Materials*, vol. 15, no. 21, pp. 1844–1849, 2003.

[29] M. Gao, S. Kirstein, H. Möhwald, A. L. Rogach, A. Kornowski, A. Eychmüller, and H. Weller, "Strongly photoluminescent CdTe nanocrystals by proper surface modification," *The Journal of Physical Chemistry B*, vol. 102, no. 43, pp. 8360–8363, 1998.

[30] S. Akhavan, C. Uran, B. Bozok, K. Gungor, V. Lesnyak, N. Gaponik, A. Eychmller, and H. V. Demir, "Large-area tandem photosensitive nanocrystal skins: Fragmentable and flexible," *(In submission)*.

[31] A. L. Rogach, T. Franzl, T. A. Klar, J. Feldmann, N. Gaponik, V. Lesnyak, A. Shavel, A. Eychmüller, Y. P. Rakovich, and J. F. Donegan, "Aqueous synthesis of thiol-capped CdTe nanocrystals: state-of-the-art," *The Journal of Physical Chemistry C*, vol. 111, no. 40, pp. 14628–14637, 2007.

[32] V. Lesnyak, A. Lutich, N. Gaponik, M. Grabolle, A. Plotnikov, U. Resch-Genger, and A. Eychmüller, "One-pot aqueous synthesis of high quality near infrared emitting $Cd_{1-x}Hg_x$ te nanocrystals," *Journal of Materials Chemistry*, vol. 19, no. 48, pp. 9147–9152, 2009.

[33] V. Lesnyak, N. Gaponik, and A. Eychmüller, "Colloidal semiconductor nanocrystals: the aqueous approach," *Chemical Society Reviews*, vol. 42, no. 7, pp. 2905–2929, 2013.

[34] V. M. Agranovich, *Surface polaritons*. Elsevier, 2012.

[35] K. L. Kelly, E. Coronado, L. L. Zhao, and G. C. Schatz, "The optical properties of metal nanoparticles: The influence of size, shape, and dielectric environment," *The Journal of Physical Chemistry B*, vol. 107, no. 3, pp. 668–677, 2003.

[36] P. Drude, "Zur elektronentheorie der metalle," *Annalen der Physik*, vol. 306, no. 3, pp. 566–613, 1900.

[37] A. Powell, N. Hjerrild, A. Watt, H. Assender, and J. Smith, "Directional plasmonic scattering from metal nanoparticles in thin-film environments," *Applied Physics Letters*, vol. 104, no. 8, p. 081110, 2014.

[38] C. Uran, "Fabrication of an on-chip nanowire device with controllable nanogap for manipulation, capturing, and electrical characterization of nanoparticles," *http://www.thesis.bilkent.edu.tr/0006139.pdf*, 2008.

[39] D. J. Pena, J. K. Mbindyo, A. J. Carado, T. E. Mallouk, C. D. Keating, B. Razavi, and T. S. Mayer, "Template growth of photoconductive metal-CdSe-metal nanowires," *The Journal of Physical Chemistry B*, vol. 106, no. 30, pp. 7458–7462, 2002.

[40] D. Xu, Y. Xu, D. Chen, G. Guo, L. Gui, and Y. Tang, "Preparation of CdS single-crystal nanowires by electrochemically induced deposition," *Advanced Materials*, vol. 12, no. 7, pp. 520–522, 2000.

[41] M. S. Gudiksen, L. J. Lauhon, J. Wang, D. C. Smith, and C. M. Lieber, "Growth of nanowire superlattice structures for nanoscale photonics and electronics," *Nature*, vol. 415, no. 6872, pp. 617–620, 2002.

[42] C. R. Martin, "Membrane-based synthesis of nanomaterials," *Chemistry of Materials*, vol. 8, no. 8, pp. 1739–1746, 1996.

[43] B. R. Martin, D. J. Dermody, B. D. Reiss, M. Fang, L. A. Lyon, M. J. Natan, and T. E. Mallouk, "Orthogonal self-assembly on colloidal gold-platinum nanorods," *Advanced Materials*, vol. 11, no. 12, pp. 1021–1025, 1999.

[44] S. R. Nicewarner-Pena, R. G. Freeman, B. D. Reiss, L. He, D. J. Peña, I. D. Walton, R. Cromer, C. D. Keating, and M. J. Natan, "Submicrometer metallic barcodes," *Science*, vol. 294, no. 5540, pp. 137–141, 2001.

[45] C. D. Keating and M. J. Natan, "Striped metal nanowires as building blocks and optical tags," *Advanced Materials*, vol. 15, no. 5, pp. 451–454, 2003.

[46] C. Uran, E. Unal, R. Kizil, and H. V. Demir, "On-chip-integrated nanowire device platform with controllable nanogap for manipulation, capturing, and electrical characterization of nanoparticles," *IEEE Journal of Selected Topics in Quantum Electronics*, vol. 15, no. 5, pp. 1413–1419, 2009.

[47] J. A. Sioss and C. D. Keating, "Batch preparation of linear Au and Ag nanoparticle chains via wet chemistry," *Nano Letters*, vol. 5, no. 9, pp. 1779–1783, 2005.

[48] N. I. Kovtyukhova, T. E. Mallouk, and T. S. Mayer, "Templated Surface Sol–Gel Synthesis of SiO_2 Nanotubes and SiO_2-Insulated Metal Nanowires," *Advanced Materials*, vol. 15, no. 10, pp. 780–785, 2003.

[49] C. Uran and H. V. Demir, "Arrays of suspended plasmonic nanodiscs," in *Photonics Conference (IPC), 2013 IEEE*, pp. 558–559, IEEE, 2013.

[50] R. Oldenbourg, "A new view on polarization microscopy," *Nature*, vol. 381, no. 6585, pp. 811–812, 1996.

[51] C. Weder, C. Sarwa, A. Montali, C. Bastiaansen, and P. Smith, "Incorporation of photoluminescent polarizers into liquid crystal displays," vol. 279, no. 5352, pp. 835–837, 1998.

[52] Z. Yu, P. Deshpande, W. Wu, J. Wang, and S. Y. Chou, "Reflective polarizer based on a stacked double-layer subwavelength metal grating structure fabricated using nanoimprint lithography," *Applied Physics Letters*, vol. 77, no. 7, 2000.

[53] S. Saraf, R. L. Byer, and P. J. King, "High-extinction-ratio resonant cavity polarizer for quantum-optics measurements," *Applied Optics*, vol. 46, no. 18, pp. 3850–3855, 2007.

[54] J. Feng, Y. Zhao, X.-W. Lin, W. Hu, F. Xu, and Y.-Q. Lu, "A transflective nano-wire grid polarizer based fiber-optic sensor," *Sensors*, vol. 11, no. 3, pp. 2488–2495, 2011.

[55] B. Schnabel, E.-B. Kley, and F. Wyrowski, "Study on polarizing visible light by subwavelength-period metal-stripe gratings," *Optical Engineering*, vol. 38, no. 2, pp. 220–226, 1999.

[56] J. J. Wang, L. Chen, X. Liu, P. Sciortino, F. Liu, F. Walters, and X. Deng, "30-nm-wide aluminum nanowire grid for ultrahigh contrast and transmittance polarizers made by UV-nanoimprint lithography," *Applied Physics Letters*, vol. 89, no. 14, 2006.

[57] J. Wang, J. Deng, X. Deng, F. Liu, P. Sciortino, L. Chen, A. Nikolov, and A. Graham, "Innovative high-performance nanowire-grid polarizers and integrated isolators," *IEEE Journal of Selected Topics in Quantum Electronics*, vol. 11, no. 1, pp. 241–253, 2005.

[58] C. Uran, T. Erdem, B. Guzelturk, N. K. Perkgz, S. Jun, E. Jang, and H. V. Demir, "Highly polarized light emission by isotropic quantum dots integrated with magnetically aligned segmented nanowires," *Applied Physics Letters*, vol. 105, no. 14, 2014.

[59] D. Whang, S. Jin, Y. Wu, and C. M. Lieber, "Large-scale hierarchical organization of nanowire arrays for integrated nanosystems," *Nano Letters*, vol. 3, no. 9, pp. 1255–1259, 2003.

[60] J. J. Boote and S. D. Evans, "Dielectrophoretic manipulation and electrical characterization of gold nanowires," *Nanotechnology*, vol. 16, no. 9, p. 1500, 2005.

[61] C. M. Hangarter, Y. Rheem, B. Yoo, E.-H. Yang, and N. V. Myung, "Hierarchical magnetic assembly of nanowires," *Nanotechnology*, vol. 18, no. 20, p. 205305, 2007.

[62] M. G. Bellino, E. J. Calvo, and G. J. Gordillo, "Nanowire manipulation on surfaces through electrostatic self-assembly and magnetic interactions," *Physica Status Solidi - Rapid Research Letters*, vol. 3, no. 1, pp. 1–3, 2009.

[63] S. Liu, J. B. H. Tok, and Z. Bao, "Nanowire Lithography: Fabricating Controllable Electrode Gaps Using Au-Ag-Au Nanowires," *Nano Letters*, vol. 5, no. 6, pp. 1071–1076, 2005.

[64] M. Grabolle, M. Spieles, V. Lesnyak, N. Gaponik, A. Eychmller, and U. Resch-Genger, "Determination of the fluorescence quantum yield of quantum dots: Suitable procedures and achievable uncertainties," *Analytical Chemistry*, vol. 81, no. 15, pp. 6285–6294, 2009.

[65] C. Uran, E. Unal, R. Kizil, and H. V. Demir, "On-chip integrated nanowire devices with controllable nanogap for manipulation, capturing, and electrical characterization of nanoparticles," in *LEOS Annual Meeting Conference Proceedings, 2009. LEOS'09. IEEE*, pp. 217–218, IEEE, 2009.

[66] I. Zoric, M. Zach, B. Kasemo, and C. Langhammer, "Gold, platinum, and aluminum nanodisk plasmons: material independence, subradiance, and damping mechanisms," *ACS Nano*, vol. 5, no. 4, pp. 2535–2546, 2011.

[67] J. N. Anker, W. P. Hall, O. Lyandres, N. C. Shah, J. Zhao, and R. P. Van Duyne, "Biosensing with plasmonic nanosensors," *Nature Materials*, vol. 7, no. 6, pp. 442–453, 2008.

[68] T. Erdem and H. V. Demir, "Semiconductor nanocrystals as rare-earth alternatives," *Nature Photonics*, vol. 5, no. 3, pp. 126–126, 2011.

[69] P. Reiss, M. Protiere, and L. Li, "Core/shell semiconductor nanocrystals," *Small*, vol. 5, no. 2, pp. 154–168, 2009.

[70] S. Akhavan, B. Guzelturk, V. K. Sharma, and H. V. Demir, "Large-area semi-transparent light-sensitive nanocrystal skins," *Optics Express*, vol. 20, no. 23, pp. 25255–25266, 2012.

[71] S. Akhavan, K. Gungor, E. Mutlugun, and H. V. Demir, "Plasmonic light-sensitive skins of nanocrystal monolayers," *Nanotechnology*, vol. 24, no. 15, p. 155201, 2013.

[72] H. A. Atwater and A. Polman, "Plasmonics for improved photovoltaic devices," *Nature Materials*, vol. 9, no. 3, pp. 205–213, 2010.

[73] S. P. Sundararajan, N. K. Grady, N. Mirin, and N. J. Halas, "Nanoparticle-induced enhancement and suppression of photocurrent in a silicon photodiode," *Nano Letters*, vol. 8, no. 2, pp. 624–630, 2008.

[74] S. V. Gaponenko, *Introduction to nanophotonics*. Cambridge University Press, 2010.

[75] G. Konstantatos and E. H. Sargent, "Nanostructured materials for photon detection," *Nature Nanotechnology*, vol. 5, no. 6, pp. 391–400, 2010.

[76] G. Konstantatos and E. H. Sargent, "PbS colloidal quantum dot photoconductive photodetectors: Transport, traps, and gain," *Applied Physics Letters*, vol. 91, no. 17, p. 173505, 2007.

[77] J. M. Luther, M. Law, M. C. Beard, Q. Song, M. O. Reese, R. J. Ellingson, and A. J. Nozik, "Schottky solar cells based on colloidal nanocrystal films," *Nano Letters*, vol. 8, no. 10, pp. 3488–3492, 2008.

[78] A. G. Pattantyus-Abraham, I. J. Kramer, A. R. Barkhouse, X. Wang, G. Konstantatos, R. Debnath, L. Levina, I. Raabe, M. K. Nazeeruddin, M. Gratzel, and E. H. Sargent, "Depleted-heterojunction colloidal quantum dot solar cells," *ACS Nano*, vol. 4, no. 6, pp. 3374–3380, 2010.

[79] S. Akhavan, A. F. Cihan, B. Bozok, and H. V. Demir, "Nanocrystal skins with exciton funneling for photosensing," *Small*, 2014.

[80] N. Gaponik, "Assemblies of thiol-capped nanocrystals as building blocks for use in nanotechnology," *Journal of Materials Chemistry*, vol. 20, no. 25, pp. 5174–5181, 2010.

[81] Y. W. Lin, W. L. Tseng, and H. T. Chang, "Using a Layer-by-Layer Assembly Technique to Fabricate Multicolored-Light-Emitting Films of CdSe@ CdS and CdTe Quantum Dots," *Advanced Materials*, vol. 18, no. 11, pp. 1381–1386, 2006.

[82] J. W. Ostrander, A. A. Mamedov, and N. A. Kotov, "Two modes of linear layer-by-layer growth of nanoparticle-polylectrolyte multilayers and different interactions in the layer-by-layer deposition," *Journal of the American Chemical Society*, vol. 123, no. 6, pp. 1101–1110, 2001.

[83] C. Murray, D. J. Norris, and M. G. Bawendi, "Synthesis and characterization of nearly monodisperse CdE (E= sulfur, selenium, tellurium) semiconductor nanocrystallites," *Journal of the American Chemical Society*, vol. 115, no. 19, pp. 8706–8715, 1993.

[84] D. K. Kim, Y. Lai, B. T. Diroll, C. B. Murray, and C. R. Kagan, "Flexible and low-voltage integrated circuits constructed from high-performance nanocrystal transistors," *Nature Communications*, vol. 3, p. 1216, 2012.

[85] J. Jasieniak, M. Califano, and S. E. Watkins, "Size-dependent valence and conduction band-edge energies of semiconductor nanocrystals," *ACS Nano*, vol. 5, no. 7, pp. 5888–5902, 2011.

[86] A. L. Rogach, N. Gaponik, J. M. Lupton, C. Bertoni, D. E. Gallardo, S. Dunn, N. Li Pira, M. Paderi, P. Repetto, S. G. Romanov, *et al.*, "Light-emitting diodes with semiconductor nanocrystals," *Angewandte Chemie International Edition*, vol. 47, no. 35, pp. 6538–6549, 2008.

[87] E. M. Likovich, R. Jaramillo, K. J. Russell, S. Ramanathan, and V. Narayanamurti, "High-Current-Density Monolayer CdSe/ZnS Quantum Dot Light-Emitting Devices with Oxide Electrodes," *Advanced Materials*, vol. 23, no. 39, pp. 4521–4525, 2011.

[88] A. Shavel, N. Gaponik, and A. Eychmüller, "The assembling of semiconductor nanocrystals," *European Journal of Inorganic Chemistry*, vol. 2005, no. 18, pp. 3613–3623, 2005.

[89] G. Decher, "Fuzzy nanoassemblies: toward layered polymeric multicomposites," *Science*, vol. 277, no. 5330, pp. 1232–1237, 1997.

[90] P. O. Anikeeva, C. F. Madigan, J. E. Halpert, M. G. Bawendi, and V. Bulović, "Electronic and excitonic processes in light-emitting devices

based on organic materials and colloidal quantum dots," *Physical Review B*, vol. 78, p. 085434, 2008.

[91] D. C. Oertel, M. G. Bawendi, A. C. Arango, and V. Bulović, "Photodetectors based on treated CdSe quantum-dot films," *Applied Physics Letters*, vol. 87, no. 21, p. 213505, 2005.

[92] Y. Jin, J. Wang, B. Sun, J. C. Blakesley, and N. C. Greenham, "Solution-processed ultraviolet photodetectors based on colloidal ZnO nanoparticles," *Nano Letters*, vol. 8, no. 6, pp. 1649–1653, 2008.